

STUDY OF HYDROGEN PERMEATION AND DIFFUSION IN
STEELS: PREDICTIVE MODEL FOR DETERMINATION OF
DESORBED HYDROGEN CONCENTRATION

by

Samuel Charca Mamani

A thesis submitted in partial fulfillment of the requirements for the degree of

MASTER OF SCIENCE

in

MECHANICAL ENGINEERING

UNIVERSITY OF PUERTO RICO

MAYAGÜEZ CAMPUS

2005

Approved by:

Frederick Just, Ph. D.
Member: Graduate Examination

Date

Nestor Perez, Ph. D.
Member: Graduate Examination

Date

Oswald Uwakweh, Ph. D.
Chairman: Graduate Examination

Date

A. Basir Shafiq, Ph. D.
Member: Graduate Examination (Co-Advisor)

Date

Paul Sundaran, Ph. D.
Director Mechanical Engineering Department

Date

Oscar Marcelo Suarez, Ph. D.
Representative of Graduate Studies

Date

ABSTRACT

The high mobility of hydrogen is due to the relative small size compared to the atomic size of transition metals. However the presence of defect (dislocations, voids, grain boundaries), can hinder hydrogen transport as they are potential trapping sites. The main objective is to study the hydrogen diffusivity and permeability in steels; it is possible to perform an electrochemical hydrogen permeation process in a thin film (foil or sheet) as a function of certain variables such as prior cold work, thickness, polarization charging current, grain size, electrolyte medium, type of promoter, and concentration. Devanathan and Stachurski (DS) cell is adapted to the study of hydrogen cathodic charging and permeation behavior.

Cold work in Armco-Fe sample (cold rolled condition) increases the dislocation density with these sites acting as irreversible trapping sites as reflected in the reduction of diffusivity and permeability parameters. Same behavior was observed for grain boundary. In both cases the trap binding energy obtained was 20.81KJ/mol and 15.29KJ/mol for Armco-Fe respectively.

Promoters added into the acid solution (charging electrolyte medium) accelerate hydrogen entry in to the material. The promoter that is best in acid solution (pH=1.2) is compose of arsenic, in a concentration range of 0.25 to 1.00 g/l g/l $\text{Na}_2\text{HAsO}_4 \cdot 7\text{H}_2\text{O}$. Furthermore the charging surface roughnesses have a significant effect in hydrogen permeation due to the reduction of rate of hydrogen ingress into the material.

Based on desorption test conducted on prior hydrogen charged materials at room temperature, it appears that the solubility of hydrogen in AF1410 steel is about three times approximately higher than in Armco-Fe.

As is well known hydrogen leads to a reduction in plasticity due to its embrittling properties, and consequently the effect in the reduction of fatigue life. The fatigue test performed was based on load decrement, showed a fatigue life reduction of approximately 45% than in specimen tested in air. Additionally SEM image showed a

brittle fracture surface (intergranular combined with transgranular), in the areas with presence of high hydrogen concentration.

RESUMEN

Este trabajo presenta un estudio del impacto del hidrogeno en el Hierro y los aceros súper resistentes como el AF1410. El diámetro atómico del hidrógeno es muy pequeña comparado con los diámetros atómicos de los metales, esta propiedad le da al hidrogeno a que en los metales se mueva con cierta facilidad. Para desarrollar este estudio utilizamos una replica de la celda desarrollada por Devanathan y Stachurski, con ciertas modificaciones por la disponibilidad de equipos.

Para que el proceso de ingreso del hidrógeno sea acelerado (que es lo que se requiere), utilizamos unos promotores que un compuesto a base de Arsénico, este elemento tiene la propiedad de debilitar el enlace del protón de hidrógeno y en anion del metal que se origina en la superficie del electrodo de trabajo (Hierro o acero AF1410), esto hace que el ingreso del hidrógeno sea mas acelerado. Pero a concentraciones altas de arsénico en la solución este puede ocasionar una reducción en la cantidad de hidrógeno que ingresa.

El hidrógeno tiene la propiedad de juntarse, para formar moléculas consecuentemente gas. Los lugares donde estos se pueden juntar dentro del material son las imperfecciones (dislocaciones, bordes granulares, impurezas, o cualquier otro defecto del material). El tiempo que toma estos hidrógenos para salir de estos lugares es mayor comparado con lo que toman de los lugares de cristalografía normal, en muchos casos estos tiempos tienden a ser infinitos. A estos casos se les llama atrapamientos reversibles y atrapamiento irreversibles, los cuales están caracterizados por la energía de atrapamiento (E_t) muy elevados, según los experimentos los valores obtenidos son 20.81KJ/mol y 15.29KJ/mol para las dislocaciones y los bordes granulare respectivamente.

Además del Arsénico que actúan como un promotor para el ingreso del hidrógeno, existen otros parámetros uno de ellos son la rugosidad de la superficie (acabado superficial) que disminuye la cantidad de hidrógeno que ingresa dentro del material.

El coeficiente de difusión, es función del espesor decreciendo cuando estos aumentan, esto se debe al incremento de la cantidad imperfecciones, y en consecuencia el aumento del numero de atrapamientos.

Cuando el hidrógeno se junta en las imperfecciones y el material esta sometido a cargas externas (cíclicas), estos tienden a fallar prematuramente debido al efecto del hidrógeno, que reduce la plasticidad (ductilidad), con la consecuente reducción de la vida útil del material.

DEDICATION

To my parents Melquíades Charca, and Cecilia Mamani; my brothers and sister: Daniel, Marcial, Albino, Jaime and Lucrecia; my nieces and nephews: Nelly, Evelin, Rubí (Ceci), Alexander, and Marcel; for their immensurable support and love

ACKNOWLEDGEMENTS

During the development of my graduate studies in the University of Puerto Rico several persons and institutions collaborated directly and indirectly with my research. Without their support it would be impossible for me to finish my work. That is why I wish to dedicate this section to recognize their support.

First of all, thanks to my advisor, Dr. Oswald Uwakweh for your encouragement, support and guidance in the development of this thesis. I consider myself fortunate to be his student. I would like to also thank to my co-advisor and PI project (ONR-grant # N000140310540), Dr. Basir shafiq, that in same way help me a development an excellent investigation. Thank to General Engineering Department, University of Puerto Rico, Mayagüez Campus, for offering me an assistantship during a two year.

My special thank to Dr. Oscar Marcelo Suarez and Ms. Amilcar Quispitupa Yupa for support me and guidance in any moment for 24 hour of day; my friend Maryann Batista for their suggestion in experiment and thesis development.

Finally I must thank to technician of Mechanical Engineer Jessamine Hernandez and Pedro Velasquez for provide me the experiment materials.

ABSTRACT	<i>ii</i>
RESUMEN	<i>iv</i>
ACKNOWLEDGEMENTS	<i>vii</i>
Table List	<i>xi</i>
Figure List	<i>xii</i>
1. INTRODUCTION	2
1.1. Objective	4
1.1.1. General Objective	4
1.1.2. Specific Objective	4
1.2. Literature Review	5
1.2.1. Hydrogen Evolution and Entry	5
1.2.2. Electrochemical Method for Hydrogen Charging	8
1.2.3. Hydrogen Permeation	10
1.2.4. Trapping of Hydrogen in Steels	11
1.2.5. Hydrogen Source and Embrittlement.....	13
1.2.6. Theories for Hydrogen Degradation	13
1.2.6.1. Pressure Theory	13
1.2.6.2. Surface Energy	14
1.2.6.3. Transport Model.....	14
1.2.6.4. Hydride Formation.....	15
1.2.6.5. Localized Slip Model.....	16
1.3. The Diffusion Process	17
1.3.1. Basic Hypothesis of Mathematical Theory	17
1.3.2. Mathematical Theory to Hydrogen Permeation	18
1.4. Fatigue Crack Propagation	20
1.4.1. Load Decrementing Testing (LDT)	20
1.4.2. Crack Growth Measurement.....	21
2. EXPERIMENTAL	22
2.1. Materials	22
2.2. Material Preparation	23
2.3. Permeation	24
2.4. Desorption	26
2.5. Microstructure	26
2.6. Roughness	26
2.7. Mechanical Testing	26
3. RESULT	28

3.1.	<i>Hydrogen Permeation Armco-Fe</i>	28
3.1.1.	Effect of Solution and Poison Concentration in Hydrogen Permeation (HP)	28
3.1.2.	Effect of Type of Promoter on Hydrogen Permeation	30
3.1.3.	Determination Optimal Cathodic Charging Current to Hydrogen Permeation	31
3.1.4.	Effect of Sample Thickness on Hydrogen Permeation	32
3.1.5.	Effect of Cold Work on Hydrogen Permeation	32
3.1.6.	Grain Dimension on Hydrogen Permeation	35
3.1.7.	Roughness Effect on Hydrogen Permeation	36
3.2.	<i>Hydrogen Permeation in AF1410 Steel</i>	37
3.2.1.	Determination of Optimal Charging Current for Hydrogen Permeation	37
3.2.2.	Effect of Thickness on Hydrogen Permeation	38
3.2.3.	Surface Roughness Effect on Hydrogen Permeation	39
3.3.	<i>Hydrogen Charging of AF1410 Steel Compact Tension Specimen</i>	40
3.4.	<i>Fatigue Crack Propagation in AF1410 Steel</i>	40
4.	<i>DISCUSSION</i>	43
4.1.	<i>Hydrogen Permeation (HP) on Armco-Fe</i>	43
4.1.1.	Effect of Solution and Poison Concentration on HP	43
4.1.2.	Effect of Kind of Promoter on HP (Armco-Fe)	44
4.1.3.	Effect of Thickness on HP (Armco-Fe)	45
4.1.4.	Effect of Cold Work on HP (Armco-Fe)	47
4.1.5.	Grain Dimension in Hydrogen Permeation (Armco-Fe)	49
4.1.6.	Roughness Effect on HP (Armco-Fe)	50
4.2.	<i>Hydrogen Permeation on AF1410 Steel</i>	52
4.2.1.	Optimal Charging Current (AF1410 Steel)	52
4.2.2.	Effect of Thickness (AF1410 Steel)	53
4.2.3.	Roughness Effect on Hydrogen Permeation	54
4.3.	<i>Models to Verify the Hydrogen Permeation and Diffusion Coefficient (from Experiment)</i>	55
4.3.1.	Armco Fe	55
4.3.2.	AF1410 Steel	58
4.3.3.	Hydrogen Concentration on Charging Surface	60
4.3.3.1.	Armco-Fe	60
4.3.3.2.	AF1410 Steel	63
4.3.4.	Hydrogen Desorption	64
4.3.4.1.	Armco-Fe	64
4.3.4.2.	AF1410 Steel	67
4.4.	<i>Optical Microscopy Analyses of Charging Surface</i>	68
4.4.1.	Armco-Fe	68
4.4.1.1.	Charging Condition	68
4.4.1.2.	Promoter Effect	70
4.4.2.	AF1410 Steel	71
4.5.	<i>Fatigue Crack Propagation Analysis (AF1410 Steel)</i>	72
4.5.1.	Fracture Surface Analysis	74

5.	<i>CONCLUSIONS AND RECOMMENDATIONS</i>	78
5.1.	<i>Conclusions</i>	78
5.2.	<i>Future Work</i>	80
	5.2.1. Hydrogen Thermal Desorption	80
6.	<i>REFERENCES</i>	81
	<i>APPENDIX A</i>	84
A.1.	<i>Mathematical Consideration of Diffusion Phenomenon</i>	84
	A.1.1. Deduction of Mathematical Approximation to Determine the Diffusion Coefficient Parameter 85	
	<i>APPENDIX B</i>	86
B.1.	<i>Slope Method to Determine the Diffusion Coefficient</i>	86

Table List

Tables	Page
Table 1 Thermodynamic properties of some metal-hydrogen system [11]	15
Table 2; Composition of Armco-Fe	22
Table 3: (a) Composition of AF1410 steel in Wt. % and (b) Mechanical properties of AF1410 steel	23
Table 4: Summary of amount hydrogen transport with different concentration of promoter.	30
Table 5: Summary of breakthrough time and permeation steady state current for cold worked sample and the heat treated condition.	33
Table 6: Surface roughness for different degree of grid paper number (Armco-Fe).	36
Table 7: Surface roughness for different degree of grid paper number (AF1410 steel) ...	39
Table 8: Summary of diffusion coefficient with breakthrough time and slope method (Armco-Fe).	46
Table 9: Hydrogen trap binding energy for Armco-Fe.	46
Table 10: Comparison of hydrogen diffusion coefficient in cold work and heat treatment samples in different thickness (Armco-Fe).	48
Table 11: Diffusion coefficient (breakthrough method) as a function of grain size (after heat treatment).	48
Table 12: Trap binding energy as a function of material thickness and thermodynamic state (Armco-Fe).	49
Table 13: Hydrogen diffusion coefficient as a function of grain size, with same thickness ($L = 0.20 \pm 0.015 \text{ mm}$) for Armco-Fe.	49
Table 14: Trap binding energy as a function of grain size, with same thickness ($L =$ $0.20 \pm 0.015 \text{ mm}$) (Armco-Fe).	50
Table 15: Roughness effect on hydrogen permeation (Armco-Fe).	51
Table 16: Hydrogen diffusion coefficient based on the slope method (AF1410 steel). ...	53
Table 17: Relation of diffusible and trapped ($d_g = 16.0 \mu\text{m}$) hydrogen (Armco-Fe).	66
Table 18 Relation of diffusible and trapped hydrogen (Armco-Fe).	67
Table 19: Total hydrogen desorbed of AF1410 steel.	67

Figure List

Figures	Page
Figure 1: Process of hydrogen evolution and adsorption (McCright model) [5].....	6
Figure 2: Models for hydrogen entry to the metal [5]	7
Figure 3: Schematic showing hydrogen discharge recombination permeation and selfedged reaction [16]	8
Figure 4: Electrochemical hydrogen charging condition. (a) Potentiostatic, (b) galvanostatic (c) Potentiometric, (d) steady-state a.c. [6]; (E = potential, I = current, R* real part, X* imaginary part of impedance) [6].....	9
Figure 5: Devanathan and Stachurski cell [5].....	10
Figure 6: Trapping site model showing, energy level in the trap vicinity [10]	12
Figure 7: Summary of hydrogen process (hydrogen source and transport) and micro structural locations [8].	13
Figure 8: schematic illustration of the surface energy model, the model requires that a specific ion from the environment B, interacts and reduces the cohesive strength of straining bond A-A ₀ at the tip of a brittle crack [5].	14
Figure 9: Schematic depiction of microstructure fracture modes (a) high K, microvoid coalescence (b) intermediate K, quasicleavage (c) low K, intergranular cracking (d) intergranular cracking with an assist from hydrogen pressure [8].....	17
Figure 10: DS cell for hydrogen permeation	24
Figure 11: Experiment set up.....	25
Figure 12: Compact Tension Specimen of AF1410 steel	27
Figure 13: Complete hydrogen permeation experiment profile (As-receive cold worked Armco-Fe).....	28
Figure 14: Profile of HP with two kinds of solution (Armco-Fe with previous heat treated)	28
Figure 15: Hydrogen permeation profile with different concentration of promoter (Armco-Fe with prior heat treated).....	29
Figure 16: Hydrogen permeation profile for two different promoters (Armco-Fe with previous heat treated).....	30
Figure 17: Hydrogen permeation profile for varying cathodic current (Armco-Fe, with previous heat treated).....	31
Figure 18: (a) Breakthrough time (t _b) variation with cathodic charging current (Armco- Fe), (b) maximum permeation reached to with different cathodic charging current.31	31
Figure 19: (a) HP profile with thickness variation (Armco-Fe, with previous heat treated), (b) maximum permeation reached to different thickness.	32
Figure 20, HP profile for (a) cold work (As-receive) and (b) with heat treatment two hours to 600 °C, for L = 0.20 mm (Armco-Fe).....	33
Figure 21: HP profile for (a) cold work (As-receive) and (b) with heat treatment (two hours to 600 °C), for L=0.30 mm (Armco-Fe).	34

Figure 22: HP profile for (a) cold work (As-receive) and (b) with heat treatment (two hours to 600 °C), L=0.40mm (Armco-Fe).....	34
Figure 23: HP profile for (a) hot rolled condition and (b) additionally heat treatment (two hours to 600 °C), L = 0.80 mm (Armco-Fe).....	35
Figure 24: Hydrogen permeation profile (same thickness) with variable grain size (Armco-Fe).....	35
Figure 25: Profile of HP with different surface roughness.....	36
Figure 26: Atomic Force Microscope (AFM) generated surface topography ($R_q = 198.00$ nm).....	37
Figure 27: hydrogen permeation profile, with different charging condition (AF1410 steel).....	37
Figure 28: Hydrogen charging current vs. time (AF1410 steel).....	38
Figure 29, Hydrogen Permeation, for different thickness under same charging current (AF1410 steel).....	39
Figure 30: Hydrogen Permeation profiles, same thickness and variable surface roughness (AF1410 steel).....	40
Figure 31: crack growth rate (da/dN) as function of crack length (R=0.4).....	41
Figure 32: Crack Growth rate (da/dN) as a function of $K_{I_{max}}$ (R=0.4).....	42
Figure 33: Effect of promoter in hydrogen charging; (a) without promoter, (b) with promoter.....	44
Figure 34: Diffusion coefficient with respect to sample thickness (with previous heat treated two hours to 600°C, with air cooling) (Armco-Fe).....	46
Figure 35: logarithmic regression of grain size with respect to diffusion coefficient.	50
Figure 36: Effect of surface roughness on hydrogen entry to sample.	51
Figure 37: Microstructure of AF1410 steel.....	52
Figure 38: Hydrogen diffusion coefficient as a function of sample thickness, based on the slope method (AF1410 steel).....	54
Figure 39: Hydrogen concentration profile in permeation based on the Potentiostatic mode (equation 5).....	55
Figure 40: Hydrogen concentration profile in permeation based on the Galvanostatic Mode (equation 8).....	56
Figure 41: HP Comparison of experimental result and the models, for L = 0.20 mm thick material (Armco-Fe).....	56
Figure 42: HP Comparison of experimental results and the models for L = 0.30 mm thick material (Armco-Fe).....	57
Figure 43: HP Comparison of experimental results and the models for L = 0.80 mm thick material (Armco-Fe).....	58
Figure 44: HP comparison of experimental results and model for L = 0.09 mm thick material (AF1410 steel).....	59
Figure 45: HP comparison of experimental results and the model for L = 0.16 mm thick material (AF1410 steel).....	59

Figure 46: HP comparison of experimental results and the models for L = 0.18 mm thick material (AF1410 steel).	60
Figure 47: HP comparison of experimental results and the models L = 0.20 mm thick material (AF1410 steel).	60
Figure 48: Hydrogen permeation current density and potential monitoring in charging side (Armco-Fe).	61
Figure 49: hydrogen concentration in surface (C_s) and subsurface (C_i) evolution in function of time (Armco-Fe).	62
Figure 50: Hydrogen permeation current density and potential monitoring in charging side (AF1410 steel).	63
Figure 51: Hydrogen concentration at the surface (C_s) and subsurface (C_i) evolution as a function of time for AF1410 Steel.	64
Figure 52: Hydrogen desorption (experimental, diffusible and trapping), in exit site (Armco-Fe).	66
Figure 53: Hydrogen desorbed as a function of sample thickness (AF1410 Steel).	68
Figure 54: Optical microscopy (a) without charging, (b) 1.00 mA/cm ² charging condition, (c) 3.00 mA/cm ² charging condition and (d) 10.00 mA/cm ² (Armco-Fe), all samples have a previous heat treatment two hour to 600°C with air cooling (L= 0.80 mm).	69
Figure 55: SEM image of hydrogen induced cracking (HIC) in Armco-Fe (L=0.20mm, with previous heat treated two hour to 600°C with air cooling condition).	70
Figure 56: Optical surface micrograph; (a) 0.00 g/l Na ₂ HAsO ₄ 7H ₂ O, (b) 0.25 g/l Na ₂ HAsO ₄ 7H ₂ O, (c) 1.00 g/l Na ₂ HAsO ₄ 7H ₂ O, (d) 10.00 g/l Na ₂ HAsO ₄ 7H ₂ O (Armco-Fe) (L= 0.78±0.03mm, with previous heat treatment two hour to 600°C with air cooling condition).	71
Figure 57: (a) Extraction and (b) entry surface (AF1410 Steel) (L = 0.35mm).	72
Figure 58: Differentiation of fracture zones and cathodic hydrogen charge.	74
Figure 59: Scanning Electron Microscope (SEM) image of fracture surface, with prior cathodic hydrogen charge (AF1410 steel).	75
Figure 60: Brittle fracture zone with prior cathodic hydrogen charge (AF1410 steel). ...	75
Figure 61: Ductile fracture zone (Without hydrogen), AF1410 steel.	76
Figure 62: Ductile, brittle and quasi cleavage (QC) fracture (intermediate zone), AF1410 steel.	76
Figure 63: Ductile, brittle and quasi cleavage (CQ) fracture zone (close to face to cathodic hydrogen charge), AF1410 steel.	77
Figure 64: Ductile fracture zone combine with brittle, near to charging surface (AF1410 steel).	77
Figure 65: — Hydrogen thermal desorption analysis apparatus. a — reference gas cylinder (argon); b—carrier gas cylinder (argon); c — valve; d — pressure gauge; e — gas flow direction; f — oxygen trap; g — flow gauge; h — moisture trap; i — furnace; j — thermocouple; k — sample; l — fused silica tube; m — furnace	

controller; n — vacuum pump; o — gas chromatograph; p — computerized data acquisition system; q — flow mete [29]	80
Figure 66: Approach to steady-state flow through a plane sheet.....	86
Figure 67: Slope determined form the data of hydrogen permeation transient for Armco-Fe.....	87
Figure 68: Slope determined from the data of hydrogen permeation transient for AF1410 steel	87

1. INTRODUCTION

The reliability of structures or other components of mechanical equipment depends not only on the applied load but also on the conditions at which they operate. This could be corrosive or severe environment at which the material could lose mechanical properties, thereby causing premature failures. There are different forms of degradation, one of which is the weakening of the material due to hydrogen otherwise known as hydrogen embrittlement. This is an important aspect we have to consider for the design of components. To predict the deterioration due to or with hydrogen by any model it is necessary to calculate or evaluate from experiments diffusion, concentration and hydrogen traps (reversible or irreversible) characteristic of the material at room temperature

The impact or degradation due to hydrogen may vary with composition, microstructure, and stress levels of the material in service. The concentration of hydrogen traps in the material determines the level or degree to which the material can suffer. The concentration is a function of the coefficient of diffusion, which can be determined experimentally by different methods such as: electro chemical method, sub-surface micro hardness profiling, nuclear reaction analysis, nanoindentation measurement, Slow strain rate test (SSRT) [9, 13, 17, and 22].

The method that has greater acceptance in determining the diffusion in steel materials is the Hydrogen Permeation technique. The advantage of using this method is its simplicity and the high hydrogen concentrations that can be achieved in the material. This method can help us to recognize with more precision how alloy contents, crystal defects are affecting the diffusion process. The process of corrosion is based on the existence of anodic and cathodic regions which determines the direction of current flow, and hence corrosion rate.

Other case where hydrogen entry into the material can occur are manufacturing, e.g. during melting, electroplating, and in service when subjected to wet environments with simultaneous corrosion. In solid solution hydrogen at low concentration in the material does not affect the mechanical properties except during the application of load. As a consequence of loading dislocations are generated with possibility of becoming hydrogen traps (as these tend to migrate towards areas of high strain field). The

transported hydrogen can eventually cause high local pressure thereby reducing the stress intensity factor culminating in brittle fracture.

1.1. Objective

1.1.1. General Objective

The objective of the proposed study is to study hydrogen transport properties through permeation test based on the DS method for Armco Iron and AF1410 steel materials. With the diffusion coefficient we can develop a model that will help us calculate the hydrogen concentration in the material.

1.1.2. Specific Objective

1. Establish of Hydrogen Permeation properties in Armco Iron and AF1410 steel materials of varying thicknesses.
2. Determine the experimental permeation profiles for different ranges of charging currents and membrane thicknesses.
3. Study the effect of promoters (otherwise known as “poison”) in the permeation characteristic of these steels.
4. Develop a desorption procedure to determine the amount of hydrogen leaving the material with previous charging at room temperature in order to understand its retention rate
5. Study of the effect of surface (roughness) on hydrogen permeation
6. Determine the necessary parameters and conditions needed to introduce hydrogen in a compact fatigue test material.

1.2. Literature Review

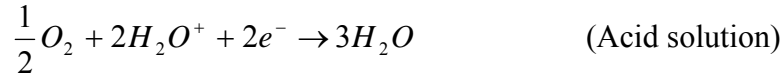
Birnbaum [11] in his reference included John's work published in 1875 where he reported most of the general phenomena of steel degradation known as Hydrogen Embrittlement (HE). Since then, research has been extended to other materials system ferrous and non-ferrous are alike.

Hydrogen has an atomic radius of 0.25-0.54 Å which compared with the diameter of other metallic atoms is much smaller. This characteristic gives hydrogen significant mobility (diffusion) in metals. Dislocations or imperfections in a material retard hydrogen diffusion and can act as hydrogen trapping sites (in most cases hydrogen trap can act as barrier that prevent hydrogen transport). In order for hydrogen embrittlement to occur, it's concentration must attain a critical level, which depends on the type or nature of material under consideration. The effect of hydrogen in materials can be critical, especially in high strength steels such as: AISI 4340, Aermet100, AF1410, and 300M which are used in aircrafts (these materials resist severe environments, but are susceptible to hydrogen embrittlement). Studies by Thomas and Scully in Aermet100 show that hydrogen has a considerable effect in the stress intensity factor [3]. Based on their observations the presence of hydrogen leads to a K_{IC} reduction from $130\text{MPa}\sqrt{m}$ to $12\text{MPa}\sqrt{m}$ [3]. Hydrogen can be introduced in a material through a variety of ways such as by electrochemical means, hydrogen gas atmospheres, plating process, etc.

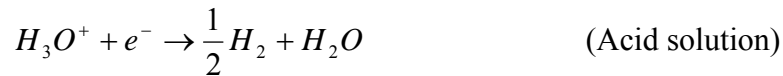
1.2.1. Hydrogen Evolution and Entry

In order for hydrogen to go through a material it must be transported to the surface of the material, followed by adsorption, absorption and eventually transported to the material bulk. Different reactions occur in corrosion; in anodic part there occurs dissolution of material (reduction of oxygen) with hydrogen evolution on the cathodic part. Both reactions can occur in acidic or alkaline solutions. Depending on the pH of the medium, the following reactions (frequently) are likely to occur [5].

- Oxygen reduction



- Hydrogen evolution



To understand hydrogen entry into a metal, it is necessary to know the characteristic of hydrogen evolution reaction. Figure, 1 [5] shows the process of hydrogen evolution reaction (HER) when a metal is in an acid solution. It shows the distinct steps associated with the entire process. First hydrated atoms are transported to the double layer (surface), a separation of hydrogen proton and water by adsorption, electro donation with the charge of electrons of material thereby producing a discharge; the process of hydrogen combination can occur by two ways atom-atom or ion-atom or both; The ultimate stage are eventually the desorption and entry into the material, with accompanying hydrogen evolution reaction culminating in the formation and hydrogen diffusion.

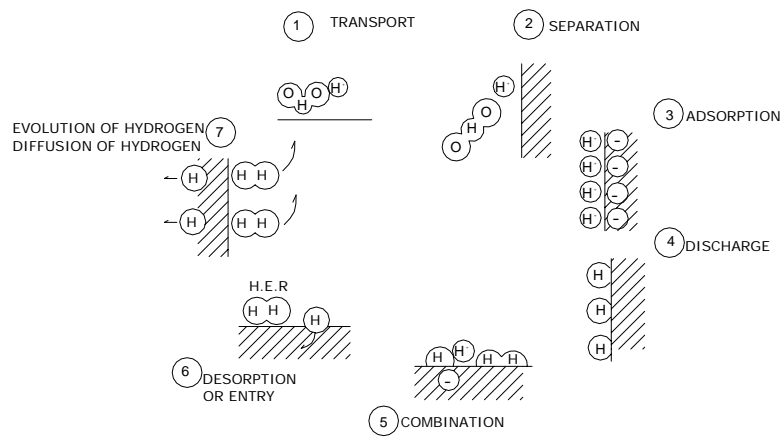


Figure 1: Process of hydrogen evolution and adsorption (McCright model) [5].

Hydrogen entry into the material can occur by two forms as reported in reference [5] detailed in Figure 2. The absorption of hydrogen could occur by way of reduced hydrogen (atomic), or otherwise by proton interaction with the metal materials bulk.

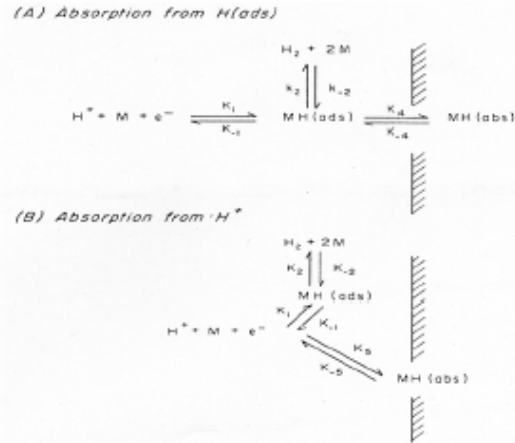
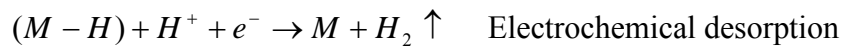


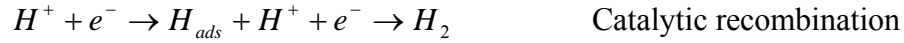
Figure 2: Models for hydrogen entry to the metal [5].

On the other hand DeLuccia [2] proposed a model that consists of three steps hydrogen evolution reaction. After the electrochemical discharge step, the newly formed hydrogen atoms combine to form hydrogen molecules (or hydrogen gas bubbles). His proposal in indicates that a small amount of hydrogen entry to the material can cause embrittlement.



In the first step reaction in acid solutions, hydrogen atoms are reduced to form neutral hydrogen atoms through a two steps reaction path thus.





Rajan, [16], proposed a model of hydrogen permeation that involves a three stage process shown in Figure 3, which consists of: (1) Hydrogen discharge reaction (proton tunneling), (2) hydrogen recombination reaction either by chemical recombination or electrochemical desorption, (3) hydrogen evolution, and (4) hydrogen diffusion and permeation (mainly by bulk diffusion),

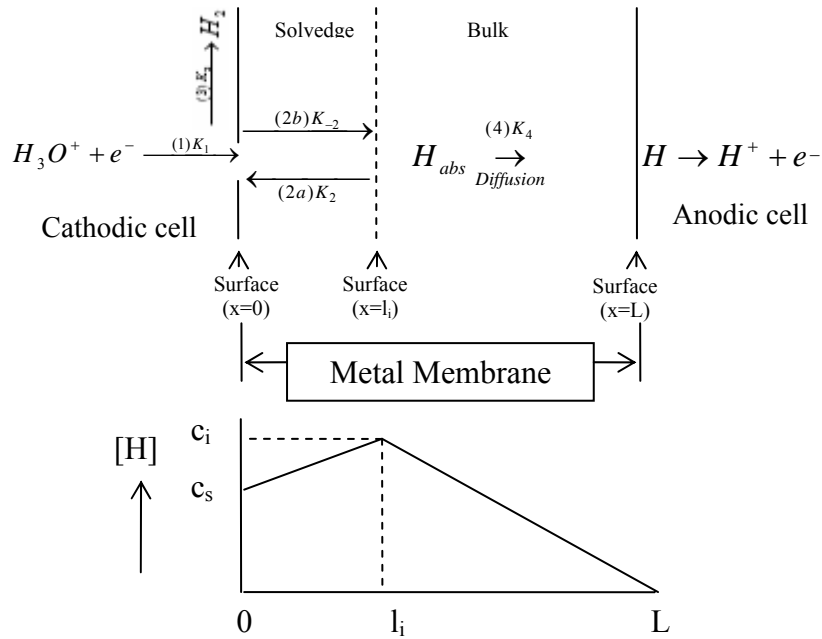


Figure 3: Schematic showing hydrogen discharge recombination permeation and selvedge reaction [16].

In the diagram: K_1 is the discharge rate coefficient, K_2 the recombination rate coefficient, K_3 the evolution rate, and K_4 the diffusion rate coefficient. The evolution and entry to the material are the same as proposed by McCright even though it is not reflected in step 3.

1.2.2. Electrochemical Method for Hydrogen Charging

There are different experimental methods or techniques for hydrogen cathodic charging which can be used to determine diffusion coefficient (D) of hydrogen in a given material as show in Figure 4.

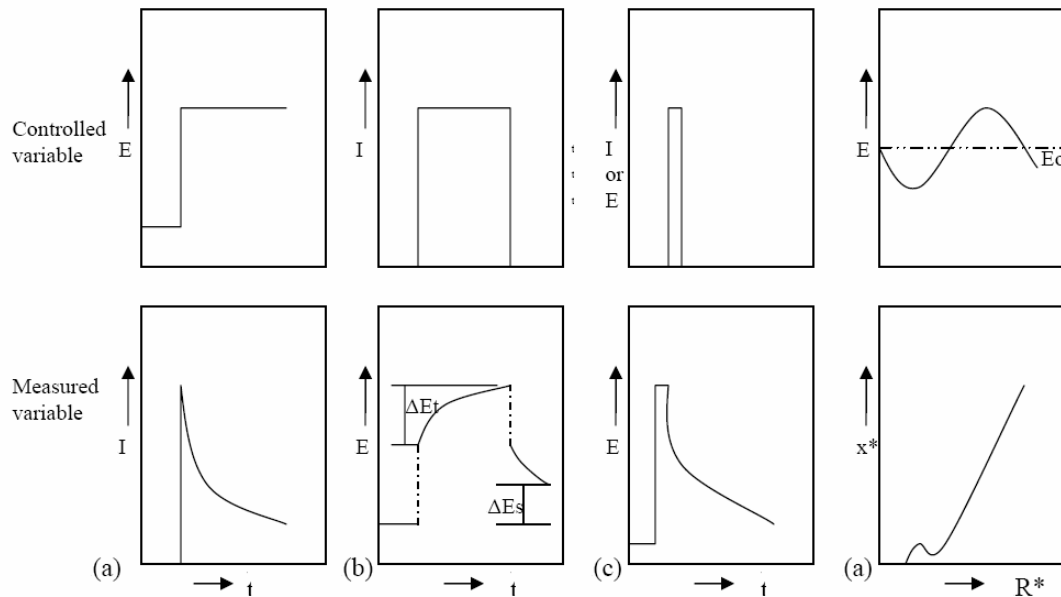


Figure 4: Electrochemical hydrogen charging condition. (a) Potentiostatic, (b) galvanostatic (c) Potentiometric, (d) steady-state a.c. [6]; (E = potential, I = current, R^* real part, X^* imaginary part of impedance) [6].

- a) **Potentiostatic:** in this kind of experiment we assume that the surface has an initial concentration of H with an equilibrium potential (E) as shown in Figure 4 (a). At $t = 0$ we apply a constant potential between the sample and electrode, with consequent change in the concentration. Next at $t > 0$ we measure the evolution of current (I), while the concentration is maintained constant.
- b) **Galvanostatic:** The parameters controlled and measured are shown in Figure 4 (b). We observe that the controlled parameter is current (I) while the measured parameter is the potential (E), on the surface of sample ($x=0$). Since the potential is a variable, the variation of hydrogen concentration is governed by de first Fick's law.
- c) **Potentiometric:** This technique assumes the initial concentration to be a constant which corresponds to an equilibrium potential E_0 (equilibrium potential). A very short high current (impulse) is applied and after interrupting the current, we measure the potential variation as a function of time in $t > 0$.

d) **Steady-State AC Method:** This technique assumes the initial concentration to be constant which corresponds to equilibrium E_0 (not net current passing through the cell). Next a small sinusoidal AC signal $E_{\max}\sin\omega t$ (E_{\max} amplitude to the ac voltage, $\omega = 2\pi f$, $f =$ is a frequency) is superimposed upon the constant dc voltage E_0 , and monitoring the response impedance parameters (R^* and x^*).

1.2.3. Hydrogen Permeation

Hydrogen permeation is the process by which an amount of hydrogen is transported from one location to other. Devanathan and Stachurski (DS) developed an electrochemical sensitive system with instantaneous recorder of hydrogen permeation rate in an electrolytic process through a metallic foil, sheet or membrane. This system consists of two separate cells, the middle of which contains a test sample (metal membrane) as shown in Figure 5

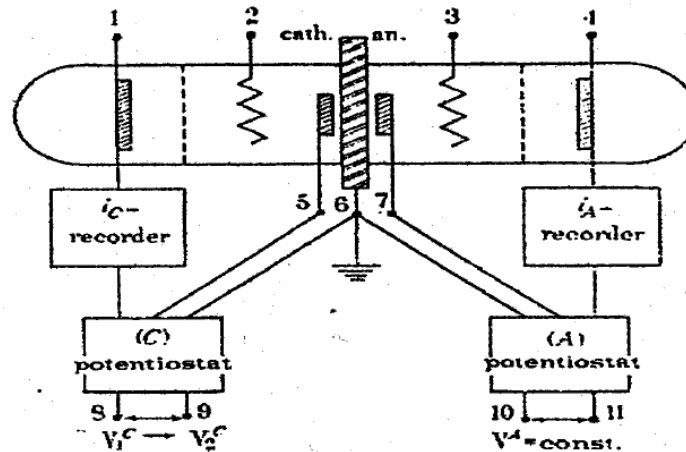


Figure 5: Devanathan and Stachurski cell [5].

In the above diagram:

- 1, 4: Platinum electrode (entry side and recorder side)
- 5, 7: Reference electrode (entry side and recorder side)
- 6: Metal Membrane

One side of the membrane acts as the cathode while the other as the anode. In the diagram the left cell (input side) contains a solution with high concentration of hydrogen ions like H_2SO_4 , NaCl , or NaOH , while in the right hand side cell (exit side) it is necessary to have a basic solution (usually NaOH) in order to avoid corrosion on the surface which will affect hydrogen permeation. Many references [3, 5, 7] indicate that it is necessary to cover the membrane with Palladium to avoid corrosion and for reliable results.

1.2.4. Trapping of Hydrogen in Steels

All solid materials contain structural defects; more so crystalline solids such as the metallic ones have certain imperfections such as vacancies, dislocation, grain boundaries areas, voids, inclusions, etc. These defects can serve as trapping sites for hydrogen and more so certain impurities or alloy elements, also can act as rapping sites, and some cases form hydride, as with C and S. These can interact preferentially with hydrogen to form gases such as CH_4 and H_2S [4], and generally lead to the formation of blister in the material.

The consequence of trapping is the reduction of transport rate of hydrogen through the material membrane. When hydrogen accumulates on these defects, it becomes difficult for subsequent hydrogen diffusion or transport while the hydrogen resident time on these sites increases correspondingly in comparison to the case for normal lattice distribution [30]. Because of these, the analysis of various aspects associated with hydrogen transport in metallic system such as hydrogen distribution, bulk hydrogen concentration, or distribution, hydrogen embrittlement, etc. can become very difficult or complicated.

There are two clearly different kinds of hydrogen trappings, namely reversible and irreversible traps. The reversible trapping is associated with limited resident time of hydrogen in a material at a specific temperature, generally with low interaction energy while irreversible trapping is when residence is permanent at a specific temperature, and site with high activation energy.

Figure 6 shows a model [10] of types of traps in terms of energy level of either interstitial sites, A, or trapping sites, B. The rate of movement of hydrogen in any given site is a function of activation energy associated with such a site. In Figure 6, E_n represents the energy for hydrogen entry from the surface into the bulk, E_s energy level for hydrogen from bulk entry to the trapping sites, E_t is the activation energy of trapping sites, while E_b is the energy which characterizes the kind of trapping (energy for hydrogen to leave the trapping sites). The relative value of E_t is an indication of the nature of dissociated trapping sites vis-à-vis reversible or other wise. For instance, if $E_t \gg E_b$, this corresponds to the irreversible trapping.

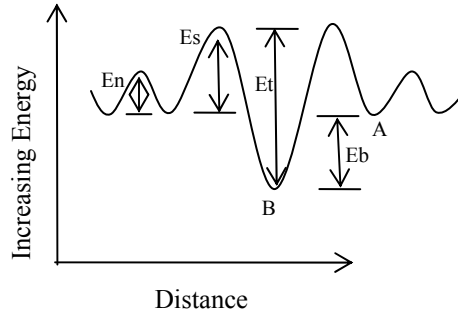


Figure 6: Trapping site model showing, energy level in the trap vicinity [10].

The reversible trap has a very significant effect on the mechanical properties of material in comparison to irreversible traps because when a material is subjected to an applied load, the reversible hydrogen traps acts so as to cause more damage or accelerate failure [5].

A general approach is possible to determine the hydrogen trap binding energy, relating the apparent diffusion coefficient with lattice diffusion coefficient. The equation relating both parameters is the Arrhenius expression [27], as shown below:

$$D_{app} = D_L \exp\left(-\frac{E_t}{RT}\right) \quad (1)$$

Where

D_{app} : apparent diffusivity (obtained experimentally)

D_L : lattice diffusivity

E_t : trap binding energy

R: real gas constants ($R=8.3145\text{J/mol } ^\circ\text{K}$)

T: absolute temperature

1.2.5. Hydrogen Source and Embrittlement

Since the hydrogen source can be different e.g., corrosive environment such as, during electroplating, in melting process, etc., our investigation focuses on electrochemical hydrogen evolution and diffusion. When hydrogen enters the material, it tends to accumulate at a wide range or variety of location within the microstructures such as on grain boundaries, inclusions, voids, dislocation and dislocation arrays, solute atoms, as well as in solid solution. Whichever of this location is the most sensitive to fracture will control the magnitude of hydrogen effects, although in general all of them will accumulate hydrogen albeit to different extents. In summary the generalized process of hydrogen embrittlement is shown in Figure 7 as proposed by Thompson [8]

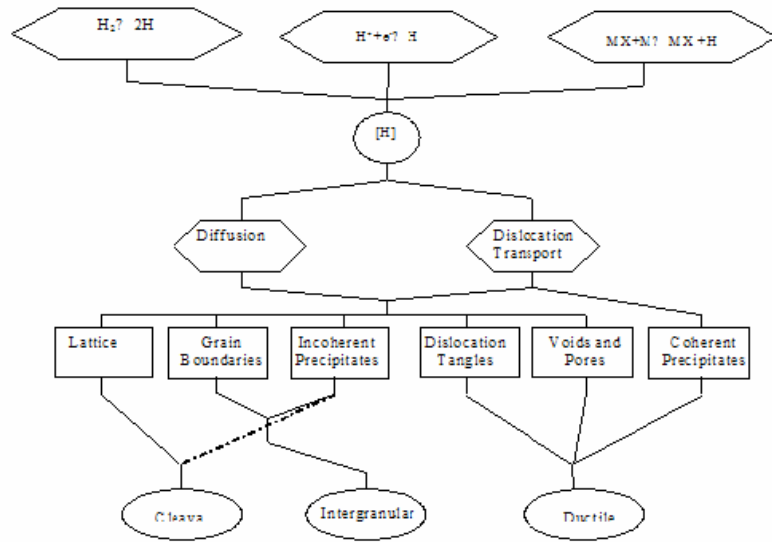


Figure 7: Summary of hydrogen process (hydrogen source and transport) and micro structural locations [8].

1.2.6. Theories for Hydrogen Degradation

1.2.6.1. Pressure Theory

Hydrogen degradation occurs when hydrogen accumulates and increases in concentration within internal voids or fissures, creating a large internal pressure which enhances voids growth and crack propagations, and in some cases finally with the

formation of blisters [1]. While the internal bubble pressure provides initial driving forces, this pressure decreases rapidly without the presence of continued hydrogen source. Birnbaum [11], in his report concluded that the formation of high pressure hydrogen bubbles, which may occur only in systems having endothermic heat of hydrogen solution can provide for crack nucleation.

1.2.6.2. Surface Energy

Birnbaum [11] formulated a relation for crack propagation derived from the energy balance during crack extension in plane strain. The principal effect of hydrogen is to reduce the effective surface energy as a result of absorption on the surface produced as the crack propagated

On the atomic scale, hydrogen absorbs and interacts with strained bonds at the crack tip, causing a reduction in a bond strength as shown in Figure 8,

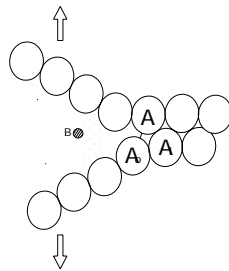


Figure 8: schematic illustration of the surface energy model, the model requires that a specific ion from the environment B, interacts and reduces the cohesive strength of straining bond A-A₀ at the tip of a brittle crack [5].

1.2.6.3. Transport Model

For Hydrogen to cause crack nucleation and crack propagation, it must be transported through a solution phase, adsorbed, absorbed, transported internally by diffusion or dislocation motion, and accelerate from one part as an internal interface where it influences nucleation and growth of a crack [11]. The hydrogen transport can be enhanced by presence of dislocation but be decreased by trapping phenomena, which acts as a wall that reduces the transport of hydrogen. While important in contributing to the degradation process, these phenomena are not by themselves mechanisms but rather contribution to the over all mechanisms.

1.2.6.4. Hydride Formation

A metal hydride might form ahead of a crack tip, in a region of high triaxial stress. Crack propagation could occur because of the cracking of the brittle phase [11].

Metal-hydrogen system exhibits a greatly disparate range of behavior. A large number of metals form stable hydrides, i.e. compounds which are generally centered about stocheometric metal-hydrogen ratio. The bonding of these hydrides ranges from metallic to covalent to ionic with their stabilities differing greatly. All of the metals which form stable hydrides are hydrogen embrittled. Hydrogen solid solubility in these systems can be very large, ranging up to values of $H / Metal \approx 1$ while the heats of solution from the gas phase are negative as shown in Table 1 [11]. In contrast to these systems, non-hydride formers have very limited ranges of solute solubilities and have positive heats of solution from the gas phase. These metals also are subject to hydrogen embrittlement, often at hydrogen concentrations as low as a few parts per million. A number of metals such as nickel exhibit an intermediate behavior, having hydrides which are stable at high hydrogen fugacities but not at the condition under which embrittlement is observed.

Table 1 Thermodynamic properties of some metal-hydrogen system [11].

Element	Hydrides	ΔH Solution (From gas phase) (KJ/mol)	ΔH Formation (of hydrides) (KJ/mol)	H solid solubility at 300 K (H/Metal)	Comments
Li	LiH		-90.7	Very small	Hydride has a ionic bonding
Cu	CuH	+54.8		<8.00E-7*	Hydride has not been reported to form from metal
Ag		+56.9		<5.00E-6*	
Au		+27.6		Extremely small*	
Mg	MgH ₂		-74.5	<0.02	
Zn	ZnH ₂				Hydride has not been reported to form from metal
Cd	CdH ₂				hydride has not been reported to form from metal
Al	AlH ₃	+25.2	-46	2.40E-8*	hydride has not been reported to form from metal
Y	YH ₂ , YH ₃		-235 (YH ₂)	~0.2†	
Ti (α)	TiH ₂ (γ)	-45.20	-123.50	0.0014†	Metastable hydrogen form

Ti (β)	TiH ₂ (γ)	-58.20		~1.00 \dagger	Solubility at T \geq 700K
Zr (α)	ZrH _{1.5} (γ)	-51.10	-94.1	<0.01 \dagger	Metastable hydrides form solubility at Solubility at T \geq 700K
Zr (β)	ZrH _{1.5} (γ)	-64.50		~1.00 \dagger	Metastable hydrides form solubility at Solubility at T \geq 700K
V	VH _{0.5} , VH, VH ₂	-31.1	-17.30 (VH _{0.5})	0.05 \dagger	
Nb	NbH, NbH ₂	-36.00	-29.30 (NbH)	0.05 \dagger	
Ta	TaH	-34.00	-20	0.20 \dagger	
Cr	CrH, CrH ₂	+47.70		<0.10E-4*	
Mo		+51.50		<0.10E-4*	
W				Extremely small*	
Mn (α)		-8.00		1.00E-4*	
Fe (α)		+28.00		3.00E-8*	
Co (hcp)		+20.50		<4.00E-5	
Ni	NiH	+16.70		<7.60E-5	NiH has been formed by electrolytic charging and under hydrostatic pressures of about 5.70E-4 Pa
Pd	PdH	-9.60	20 (Pd ₂ H)	0.03 \dagger	
Pt		+18.80		<1.00E-5	

\dagger ; Solubility in equilibrium with the hydride

*; Solubility in equilibrium with H₂ gas at 5.7 Pa (1 atm.)

1.2.6.5. Localized Slip Model

According to this model, sufficiently concentrated hydrogen can be dissolved in the lattice ahead of the crack tip thereby assisting whichever deformation process the micro structural feature will permit [1]. The microstructure, the crack tip stress intensity and the concentration of hydrogen are the factors, which determine if the intergranular quasicleavage or microvoid coalescence fracture model operates [8].

Figure 9 below shows the different mechanisms of fracture, which depend on high or low value of stress intensity factor.

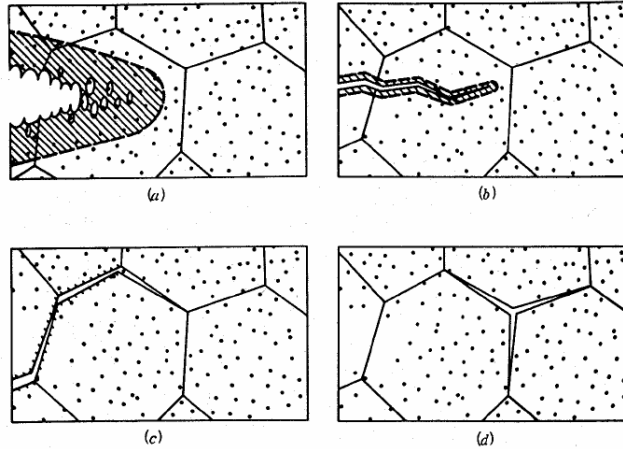


Figure 9: Schematic depiction of microstructure fracture modes (a) high K, microvoid coalescence (b) intermediate K, quasicleavage (c) low K, intergranular cracking (d) intergranular cracking with an assist from hydrogen pressure [8].

1.3. The Diffusion Process

Diffusion is a transport phenomenon that occurs when a flux is established in a given material system, such that a concentration gradient is maintained.

1.3.1. Basic Hypothesis of Mathematical Theory

Mass and heat Transfer by diffusion is also due to random molecular motion, and there is an obvious analogy between the two processes. This was recognized by Fick who first put diffusion on a quantitative basis by adopting the mathematical equation of heat conduction derived by Fourier [25 and 26].

First Fick's law
$$J = -D \left(\frac{\partial C}{\partial x} \right) \quad (2)$$

Second Fick' law
$$D \frac{\partial^2 C}{\partial x^2} = \frac{\partial C}{\partial t} \quad (3)$$

The of obtaining of both equations is shown in the Appendix, based on the deduction of Crank and Carslaw [25 and 26]

To solve these equations it is necessary to define the initial and boundary conditions, since these conditions will depend on experimental conditions of a given process.

1.3.2. Mathematical Theory to Hydrogen Permeation

For hydrogen permeation, there are different possibilities that could be used in the analysis based on the electrochemical charging technique used. Fick's laws have been shown to be applicable in the analysis of hydrogen permeation through membranes under galvanostatic or potentiostatic conditions as described below.

- i. **Potentiostatic Condition:** starting from equations (2) and (3)

$$J = -D \left(\frac{\partial C}{\partial x} \right)$$

$$D \frac{\partial^2 C}{\partial x^2} = \frac{\partial C}{\partial t}$$

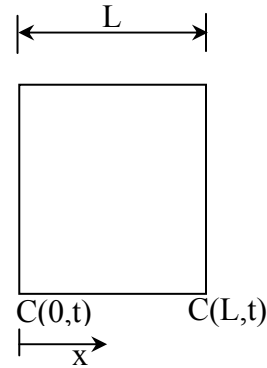
Boundary Condition

$$C(0,t) = C_i \quad t > 0$$

$$C(l,t) = C_l \quad t > 0$$

Initial Condition

$$C(x,0) = C_0$$



There are diverse methods to solve these equations. With the separation of variables method, the solution for the profile of concentration is given by:

$$C(x,t) = C_i + (C_l - C_i) \frac{x}{l} + \frac{2}{\pi} \sum_{n=1}^{\infty} \frac{C_l \cos n\pi - C_i}{n} \sin\left(\frac{n\pi x}{l}\right) \exp\left[-D \left(\frac{n\pi}{l}\right)^2 t\right] + \frac{4C_0}{\pi} \sum_{m=1}^{\infty} \frac{1}{2m+1} \sin\left(\frac{(2m+1)\pi x}{l}\right) \exp\left[-D \left(\frac{(2m+1)\pi}{l}\right)^2 t\right] \quad (4)$$

Under potentiostatic conditions we can assume that \$C_0\$ (hydrogen concentration before charging) and \$C_l\$ (hydrogen concentration in the exit side) are maintained constant to zero, in which case we will therefore obtain:

$$C(x,t) = C_i - C_i \frac{x}{l} - \frac{2}{\pi} \sum_{n=1}^{\infty} \frac{C_i}{n} \sin\left(\frac{n\pi x}{l}\right) \exp\left[-D\left(\frac{n\pi}{l}\right)^2 t\right] \quad (5)$$

For hydrogen permeation carried out under galvanostatic and potentiostatic condition the hydrogen concentration at the exit surface of the membrane is in both condition maintained at zero level, while at the entry surface simple static boundary conditions are realized. Potentiostatic condition means maintaining constant the concentration at the entrance surface while the flux is variable. In galvanostatic condition we assumed constant the flux with variable concentration and consequently the potential.

The profile for hydrogen permeation can be defined by applying the first Fick's law equation (2) which leads to the following solution of equation (6). Other forms of approximation of the diffusion parameter can be obtained by fitting the experimental data to equation (6)

$$J(t) = J_{\infty} \left[1 + 2 \sum_{n=1}^{\infty} (-1)^n \exp\left(-D\left(\frac{n\pi}{l}\right)^2 t\right) \right] \quad (6)$$

ii. **Galvanostatic Condition:** similarly by starting from equation (2) and (3), one obtains:

$$J = -D * \left(\frac{\partial C}{\partial x} \right)$$

$$D * \frac{\partial^2 C}{\partial x^2} = \frac{\partial C}{\partial t}$$

Boundary Conditions

$$\frac{\partial C(0,t)}{\partial x} = -\frac{J}{D} \quad t > 0 \quad \text{if we assign} \quad F_0 = -\frac{J_{\infty}}{D}$$

$$C(l,t) = C_l \quad t > 0$$

Initial Condition

$$C(x,0) = C_0$$

Using the separation of variables to solve the equation, we have the following equation for the concentration profile:

$$C(x,t) = F_0(x-l) + C_l + 2 \sum_{m=0}^{\infty} \left[\frac{2C_l(-1)^m}{2m+1} - \frac{4F_0l}{[(2m+1)\pi]^2} \right] \cos\left(\frac{2m+1}{2l}\pi x\right) \exp\left[-D\left(\frac{2m+1}{l}\pi\right)^2 t\right] + \frac{4C_0}{\pi} \sum_{n=1}^{\infty} \frac{(-1)^n}{2n+1} \cos\left(\frac{(2n+1)\pi x}{2l}\right) \exp\left[-D\left(\frac{(2n+1)\pi}{2l}\right)^2 t\right] \quad (7)$$

In permeation experiments, it is common for C_0 and C_L to be maintaining constant at zero. Therefore equation (7) reduces to:

$$C(x,t) = F_0(x-l) + 8F_0l \sum_{m=0}^{\infty} \left[\frac{1}{[(2m+1)\pi]^2} \right] \cos\left(\frac{2m+1}{2l}\pi x\right) \exp\left[-D\left(\frac{2m+1}{2l}\pi\right)^2 t\right] \quad (8)$$

The profile for hydrogen permeation can be expressed by applying the first Fick's law in equation (8) which gives the following equation:

$$J(t) = J_{\infty} \left[1 - \frac{4}{\pi} \sum_{n=0}^{\infty} \frac{(-1)^n}{2n+1} \exp\left(-D\left(\frac{(2n+1)\pi}{2l}\right)^2 t\right) \right] \quad (9)$$

To determine the approximate value of diffusion parameter, it is possible to adjust the permeation model profile obtained with breakthrough time, lag time and slope method; the deduction of these equations is showed in the Appendix.

1.4. Fatigue Crack Propagation

1.4.1. Load Decrementing Testing (LDT)

The load decrementing testing is a technique that is employed to study fatigue crack propagation that consists, in controlled constant strain, which is reached when kept constant the crack opening displacement (COD), while the load intensity is decreasing at the crack tip when the crack is growing. LDT is an excellent technique in conducting comparative FCG studies and it has several advantages over the load controlled fatigue testing, such as, multiple but complete lifetimes which can be obtained from a single specimen. Testing time is greatly reduced and greater control can be exercised in obtaining stable crack growth

1.4.2. Crack Growth Measurement

To calculate the crack growth one can use a compliance technique based on the equation developed by Saxena and Hudak [20] equation 10

$$a = W[1.0010 - 4.6695U_x + 18.46U_x^2 - 236.82U_x^3 + 1214.90U_x^4 - 2143.60U_x^5] \quad (10)$$

where a is the crack length and w is the depth of the specimen, and

$$U_x = \frac{1}{\left(\frac{eEV_x}{P}\right)^{0.5} + 1}$$

e , E , V and P are the specimen thickness, young's modulus, COD and load, respectively. Based on stress analysis, crack length was obtained from the real and positive root of the following equation,

$$35.6(1 - a/W)^3 + \left[\frac{V_x Et}{P} - 52.91\right](1 - a/W)^2 + 30.13(1 - a/W) - 19.75 = 0 \quad (11)$$

2. EXPERIMENTAL

2.1. Materials

Armco-Fe: The As-received materials measuring 10x10cm were in cold rolled form, with thickness corresponding to 0.25, 0.38, and 0.5 mm while 1.00 mm for the hot rolled sample. The materials composition is shown in Table 2.

Table 2; Composition of Armco-Fe.

Element	%
C	0.012
Mn	0.60
S	0.05
P	0.05
Fe	Balance

AF1410 Steel: the as-receive material measuring 8x8 cm were of varying thicknesses. In the initial normalized state the hardness was about 28 on the HRC scale with, the composition and mechanical properties are given the Table 3. The final heat treatment was carried out by Dyton T. Brown and entailed the following step.

1. Heat treatment atmosphere; air, combustion products, argon helium: use at dew point less than -40 °F, or vacuum.
2. Austenitize at 1575 ± 25 °F, 1-2 hours.
3. Oil quench at 75 to 140 °F
4. Within one hour of quenching, refrigerate at 100 °F for minimum 1 hour
5. Air warm to room temperature.
6. Age harden at 950 ± 10 °F for 5 to 8 hours
7. Air cool to room temperature
8. Secondary harden at 950 ± 25 °F for 4 to 7 hours

Table 3: (a) Composition of AF1410 steel in Wt. % and (b) Mechanical properties of AF1410 steel

	C	Mn	Si	P	S	Cr	Ni	Co	Mo	Ti	Al	O	N	S+P
Min	0.13	----	----	----	----	1.50	9.50	13.50	0.90	----	----	----	----	----
Max	0.17	0.10	0.10	0.008	0.005	2.20	10.50	14.50	1.10	0.015	0.015	0.002	0.0015	0.010

Properties (Minimum)	Longitudinal	Transversal
Ultimate Strength (ksi)	236	235
Yield Strength (.2% ksi)	215	213
Elongation (in 4D, %)	12	12
Reduction in Area (%)	60	55
Impact Strength	45	

2.2. Material Preparation

Armco-Fe: The samples (as received) were cut to 2.5 x 2.5 cm sizes followed by heat treatment at 600.00 °C for 2 hours with air cooling. The samples were successively polished starting with 240 grids to 320, 400, 600, and 800 respectively. The last step in the polishing of the material involves the use of 0.05 μ alumina suspension with CHEMOMET cloth as prescribed by BUEHLER.

AF 1410 steel: The samples were cut to 2cm x 2cm sizes. Polishing was carried out in successive steps with the following grid papers; 60, followed by 120, 240, 320, 400, 600, 800 and 1200 respectively. The final polishing stage was as in the case of Armco-Fe made with Buehler method with 0.05 μ alumina suspensions with CHEMOMET cloths.

After successive polishing, the samples were rinsed in alcohol (methanol or ethanol) followed by blow air drying. Samples were stored in desiccators afterwards in order to avoid or prevent oxidation of the polished surfaces. Before the hydrogen permeation the materials were cleaned ultrasonically (Cole Palmer 8890) in order to remove the possible presence of contaminants that can affect the process of hydrogen permeation.

2.3. Permeation

The hydrogen permeation experiments were carried out in a two cell system based on the DS technique with some modifications of the original setup, as shown below in Figure 10. In the following illustration, “C” refers to the counter electrode, “R” the reference electrode, while “W” is the working electrode, or sample under study. We used inert platinum, (Pt) electrode as the counter electrode, and Ag/Ag Cl reference electrode.

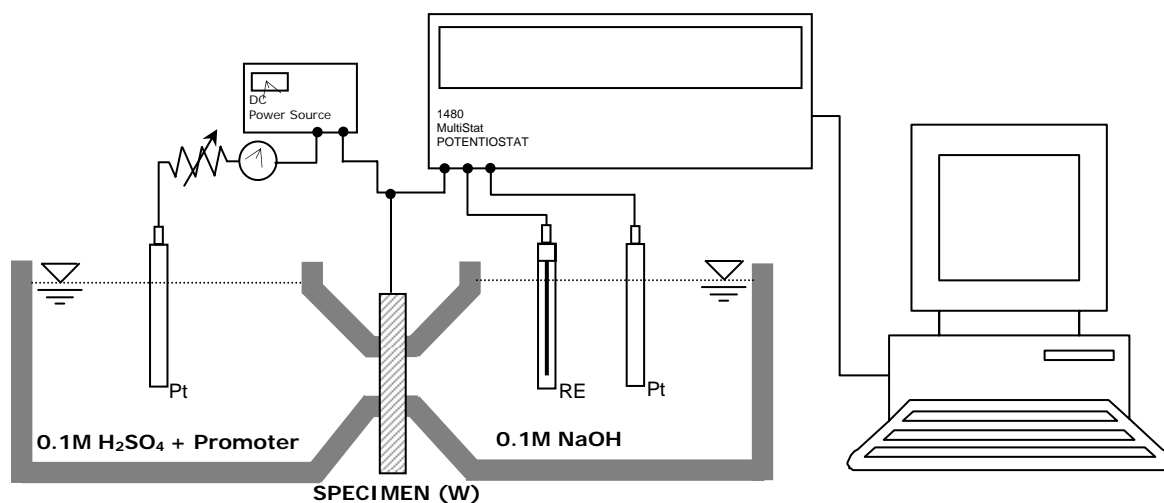


Figure 10: DS cell for hydrogen permeation.

The hydrogen charging of the sample on the left side of the set up was controlled by a DC power source (Hewlett Packard 6216C) while the variable resistance (Resistance Substitutor RS200 IET) controlled the current necessary to induce hydrogen permeation. Electrolyte consisting of 0.1M H_2SO_4 was used in the entry side. In this condition the entry side was impregnated with $\text{Na}_2\text{HAsO}_4 \cdot 7\text{H}_2\text{O}$, as poison necessary to increase the hydrogen entry rate and subsequent permeation.

The equipment that was used to control the extraction side (anodic cell) is a potentiostat Solartron 1280 that was controlled by software CorrWare. This software can control different modes such as potentiostatic, galvanostatic, potentiodynamic, galvanodynamic, etc. For this study the setup was in potentiostatic condition. The reason for this selection is the necessity to record hydrogen permeability (current density). To avoid corrosion on the extraction side we used a solution of 0.1M NaOH.

The DC power source is for applying the current in the entry cell, to induce hydrogen. There are two possibilities to applying the charge namely galvanostatic (constant current) and potentiostatic (constant potential) conditions. In potentiostatic method the variation of current in the entry side must be small if at all. During the early trials we observed a significant variation of current, and as a consequence galvanostatic condition was used in the development of the hydrogen charging procedure.

Procedure for Hydrogen Permeation is a follow:

First step: setup the device as a show in the Figure 10 and 11.

Second step: setup the software that control the potentiostat in potentiostatic mode with 300.00 mV with respect to open circuit potential (OCP), for Armco-Fe and AF1410 Steel, Next, select type of reference electrode as Ag/Ag Cl, and the permeation area 1.89 cm²

Third step: add the solution in the exit side (anodic cell) and start the polarization (run the potentiostat).

Fourth step: Set up the power source to obtain 1.00mA/cm² for Armco Fe or 2.00mA/cm² for AF1410 steel based on earlier trials. When the recorded current (anodic cell) reaches the minimum steady state of approximately 0.1 μA, add the solution in the entry side (cathodic current) to start the charging current (DC power source).

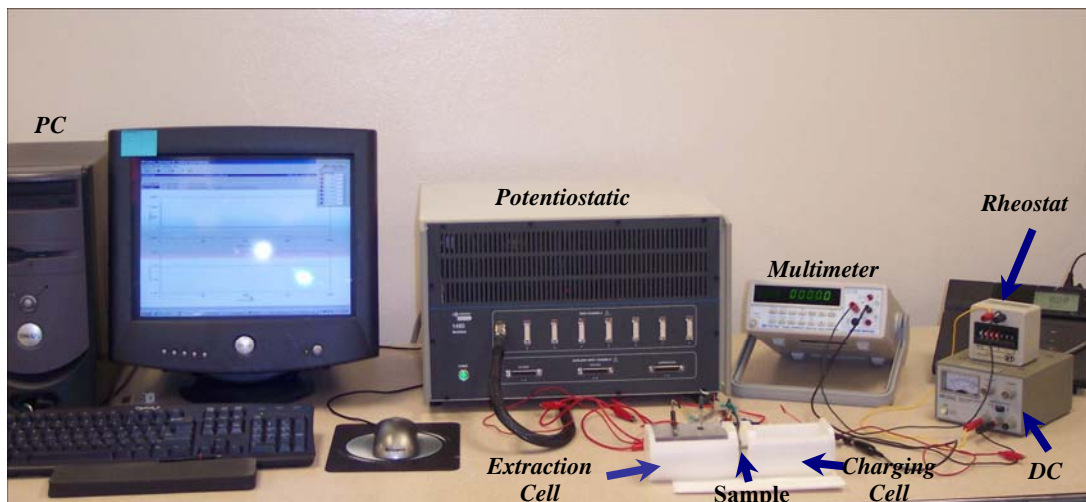


Figure 11: Experiment set up.

2.4. Desorption

This procedure is to determine the amount of hydrogen that can leave the sample at room temperature with prior cathodic charging. The procedure is the following: At the attainment of the steady state permeation current (J_{∞}), stop the charging current (power source), remove the solution of the cathodic cell and clean the charged surface with alcohol, to avoid increasing the rate of corrosion with the rest of acid solution. Let the potentiostat (anodic cell) continue to record the hydrogen leaving the sample.

2.5. Microstructure

The microstructure is a feature that affects the hydrogen diffusion and consequently its permeability and solubility. In order to show the microstructure; the samples were attacked with a solution of nitric acid in methanol 1/15 (Nital). It was immersed in the solution for 7 to 10 seconds, after which it was cleaned with distilled water and methanol, followed by blow air drying. Photos were taken using a Nikon EPIPHOT 200 with digitalized a camera (Digital Camera DN100) to obtain micrographs, with 5X, 10X, 20X, 50X and 100X, magnification.

2.6. Roughness

The surface roughness has an effect on cathodic hydrogen charging, diffusion, solubility and especially permeability. To study the effect of surface roughness, the samples were polished to obtain mirror surface finish with same procedure applied on both sides. Finally, the 600 grid paper was used to obtain a uniform roughness (only one side). These procedures were similarly adopted for the 400 and 320 grid papers respectively. NanoSurf Easy Scan DFM was used to obtain the roughness measurement and topography.

2.7. Mechanical Testing

Hydrogen has a detrimental effect in mechanical properties of the metals, especially in ultra high strength steels (AF1410), which is reflected in the fatigue lifetime. There are

diverse methods to predict lifetime, one of them is the load decrementing testing (LDT) or crack opening displacement (COD) control mode. For these experiments compact tension (CT) specimens were used, with dimension shown in Figure 12. The surface preparation of specimens is same as in samples for hydrogen permeation (sheets of AF1410 steels)

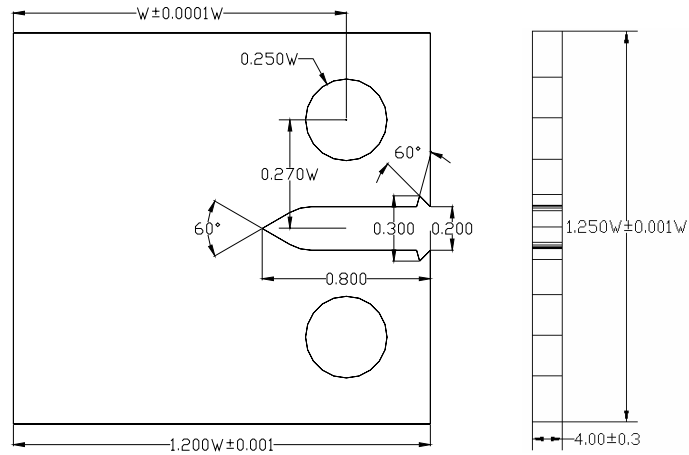


Figure 12: Compact Tension Specimen of AF1410 steel.

Where $w = 40.00mm$

To develop the LDT we used a servo hydraulic MTS 810 mechanical testing machine automated by Instron. The visual monitoring of crack propagation was carried out with a traveling calibrated telescopic microscope.

For Comparative purposes, a test was carried out in air condition (free hydrogen) and in a previously electrochemical cathodic hydrogen charged sample. Prior to fatigue test each samples was subjected to a pre-cracked condition.

3. RESULT

Figure 13 shows the complete transient of hydrogen permeation experiment. The process begins when the extraction current density is stabilized for approximately $0.1 \mu\text{A}/\text{cm}^2$ (refer to chapter 3). With cathodic charging current applied, seconds later (depending on the material kind) hydrogen transport through the sample is detected in the exit side (anodic cell) by Potentiostat.

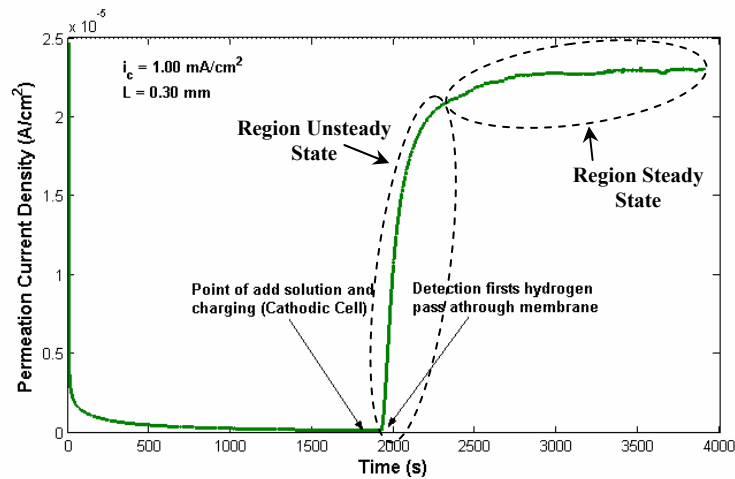


Figure 13: Complete hydrogen permeation experiment profile (As-receive cold worked Armco-Fe).

3.1. Hydrogen Permeation Armco-Fe

3.1.1. Effect of Solution and Poison Concentration in Hydrogen Permeation (HP)

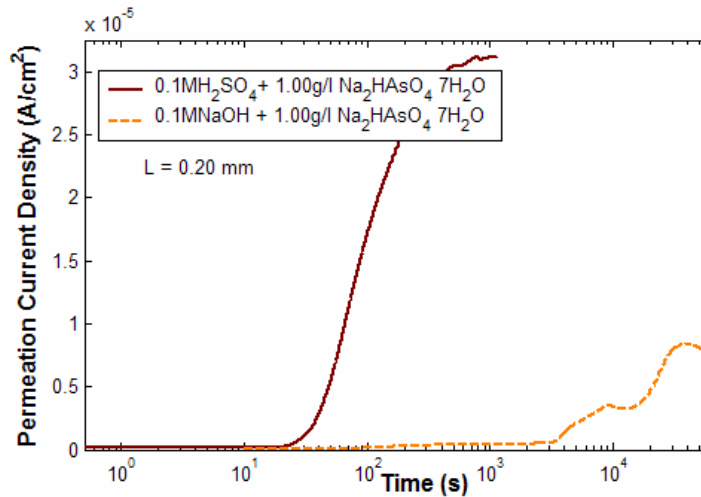


Figure 14: Profile of HP with two kinds of solution (Armco-Fe with previous heat treated).

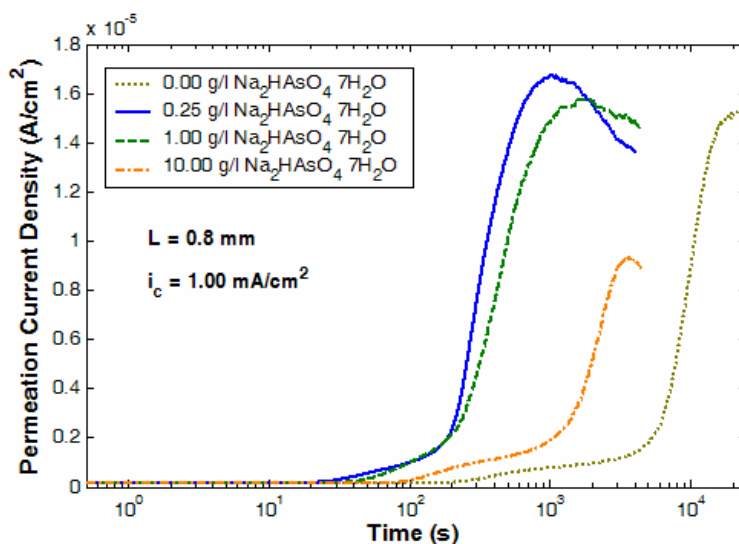


Figure 15: Hydrogen permeation profile with different concentration of promoter (Armco-Fe with prior heat treated).

Figure 14 shows the hydrogen permeation profile in two different kinds of solution, made of 0.1MNaOH and 0.1MH₂SO₄, each with a 1.00 g/l of promoter (poison). In the basic solution the charging current applied was 10.00mA/cm² [17-19] and for the acid solution, it was 1.00mA/cm².

The amount of concentration of promoters (poison) used to accelerate the process of entry of hydrogen to the bulk and consequently to permeate hydrogen is shown in Figure15. The first variation which can be appreciated is the breakthrough time (t_b). It increases with the concentration of poison, i.e., when the concentration of promoters is 1 and 0.25 g/l for Na₂HAsO₄ · 7H₂O the t_b approximately is 30 seconds, but if the concentration is increased to 10 g/l the t_b increases to 80 seconds. Furthermore a simple inspection of the permeation profile shows that the amount of hydrogen passing through the samples decreased when the concentration of poison is increased. As shown in Table 4, if the concentration of poison is between 0.25 to 1.00 g/l the total amount of hydrogen passed is relatively similar at same time, while in the absence of the promoter the charging time becomes very long and subsequently is reflected in the total amount of hydrogen detected in the exit side.

Table 4: Summary of amount hydrogen transport with different concentration of promoter.

Concentration (g/l, $\text{Na}_2\text{HAsO}_4 \cdot 7\text{H}_2\text{O}$)	Total Hydrogen (mol-H/cm ²)
0.00†	2.01×10^{-6}
0.25‡	5.64×10^{-7}
1.00‡	5.78×10^{-7}
10.00‡	2.14×10^{-7}

†Charging Time $t = 22000.00$ seconds

‡Charging Time $t = 4000.00$ seconds

3.1.2. Effect of Type of Promoter on Hydrogen Permeation

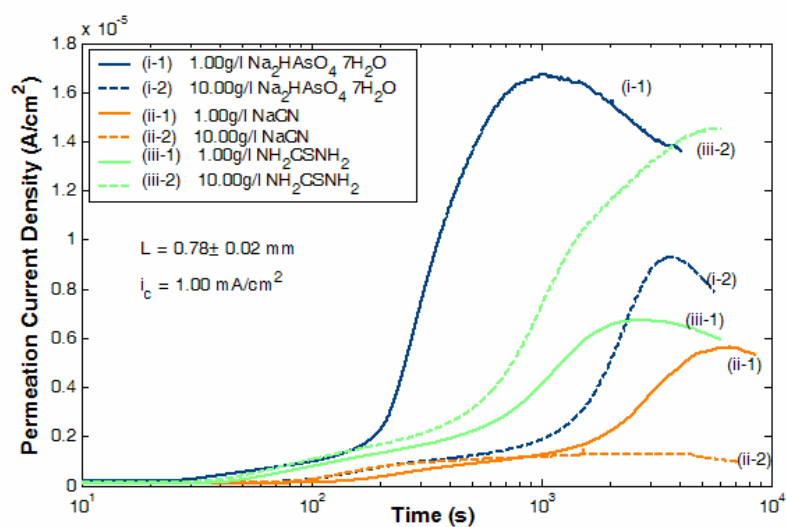


Figure 16: Hydrogen permeation profile for two different promoters (Armco-Fe with previous heat treated).

Each kind of promoter and concentration has different effect in permeation; this is shown in the Figure 16. In this case, there is no significant variation in the permeation breakthrough time, but only in the profile. For comparison purpose, two different concentrations of promoters were employed for the different promoters.

3.1.3. Determination Optimal Cathodic Charging Current to Hydrogen Permeation

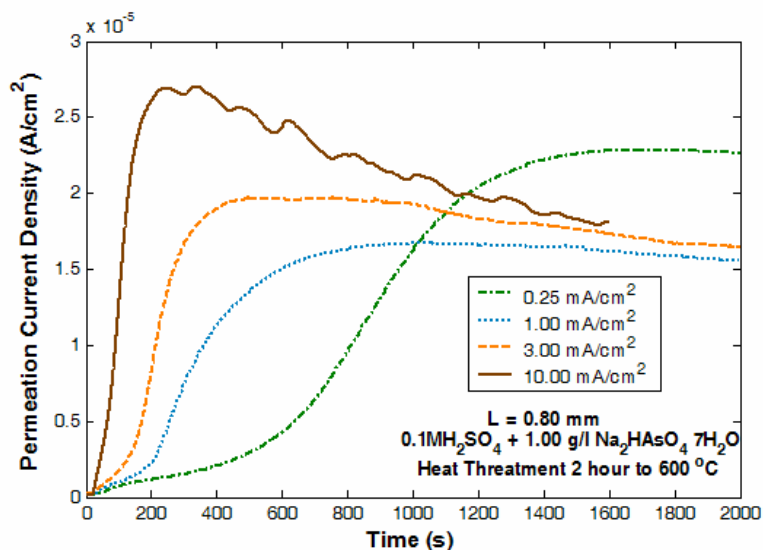


Figure 17: Hydrogen permeation profile for varying cathodic current (Armco-Fe, with previous heat treated).

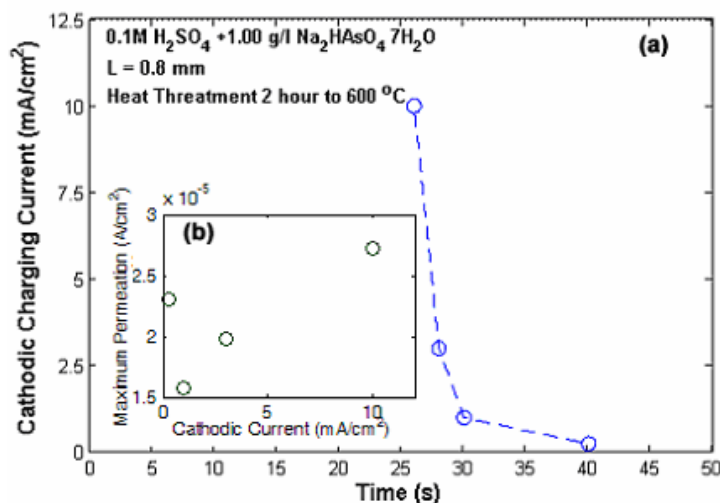


Figure 18: (a) Breakthrough time (t_b) variation with cathodic charging current (Armco-Fe), (b) maximum permeation reached to with different cathodic charging current.

The charging current is a parameter, which could be regarded as a very important one, because this it helps us to have a good approximation in determining the diffusion coefficient, and permeability. Figure 17 shows the effect of charging current in hydrogen permeation; while, Figure 18 shows the relation of charging current density with

breakthrough time (t_b) which tends to be constant at 1.00mA/cm^2 (charging current density). The higher the charging current density the more severe is the surface damage. In the profiles shown when the permeation current reaches maximum level, it tends to decrease.

3.1.4. Effect of Sample Thickness on Hydrogen Permeation

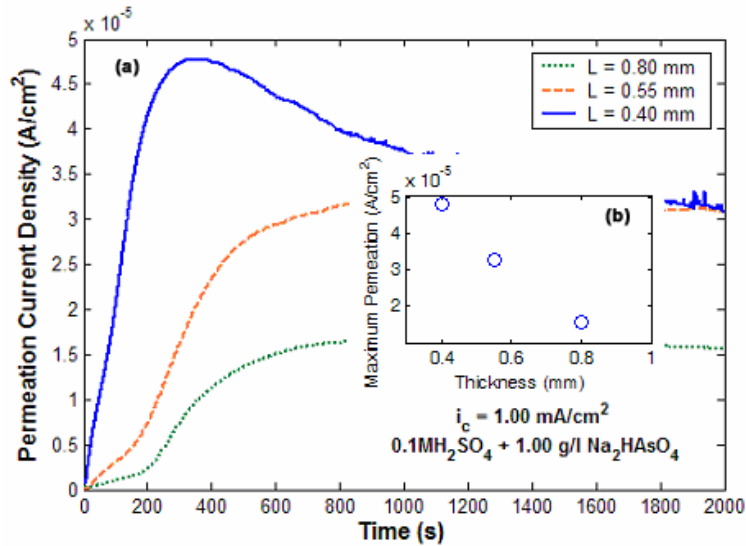


Figure 19: (a) HP profile with thickness variation (Armco-Fe, with previous heat treated), (b) maximum permeation reached to different thickness.

The permeation and diffusion parameters are a function of sample thickness, as shown in the Figure 19. If thickness is increased, the permeation and diffusion values decrease i.e., for 0.80 mm the maximum hydrogen permeation current reached is $1.67 \times 10^{-5} \text{ A/cm}^2$, while for samples of 0.55 mm the maximum permeation current reached is $3.23 \times 10^{-5} \text{ A/cm}^2$. Finally if the thickness of the sample is 0.40 mm, the maximum permeation current is $4.78 \times 10^{-5} \text{ A/cm}^2$. With these values it can be shown approximately that a reduction of hydrogen transport through the specimen occurs.

3.1.5. Effect of Cold Work on Hydrogen Permeation

Microstructure is a parameter that is of very important consideration in the development of hydrogen charging and permeation process. Figure 20 shows the profile of HP in Armco-Fe with cold work and annealing heat treatment (2 hour to 600°C ,

following with air cooling), with the corresponding micrographs shown on the right hand side for both. Micrograph (a) shows the effect of cold work and consequently the resulting grain orientation elongated along the rolling direction texture. (b) This micrograph shows the sample with heat treatment where, the difference is very clear with respect to grain shape and dimension.

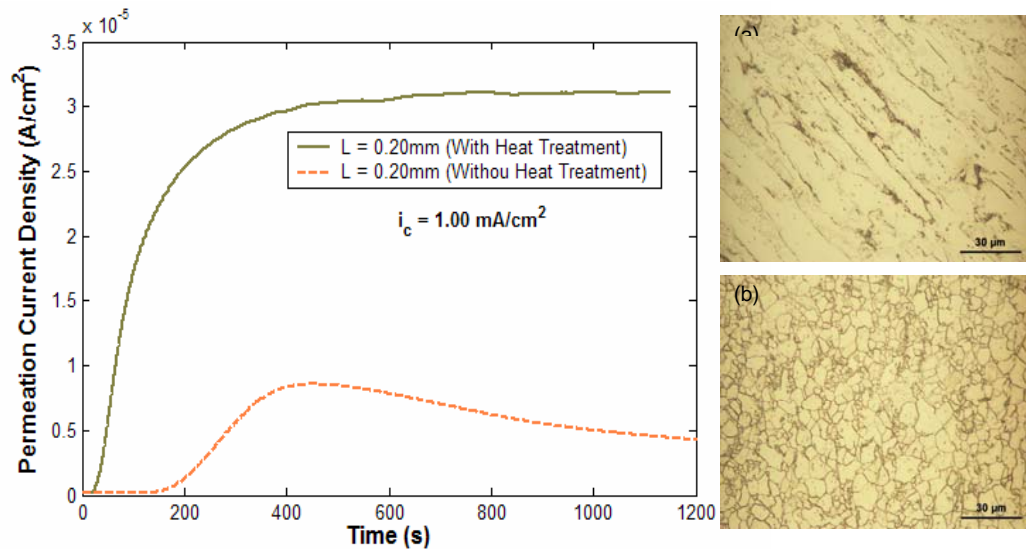


Figure 20, HP profile for (a) cold work (As-recv) and (b) with heat treatment two hours to 600 °C, for L = 0.20 mm (Armco-Fe).

Table 5 shows the summarized values of breakthrough time and maximum permeation current reached.

Table 5: Summary of breakthrough time and permeation steady state current for cold worked sample and the heat treated condition.

Thickness (mm)	t_b (s)		J_{max} (A/cm ²)	
	Cold Work (As receive)	Heat treated 2 hours to 600°C	Cold Work (As receive)	Heat treated 2 hours to 600°C
0.20	170.00	18.00	8.55×10^{-6}	3.11×10^{-5}
0.30	300.00	20.00	1.22×10^{-5}	2.25×10^{-5}
0.40	400.00	120.00	2.50×10^{-6}	2.24×10^{-5}

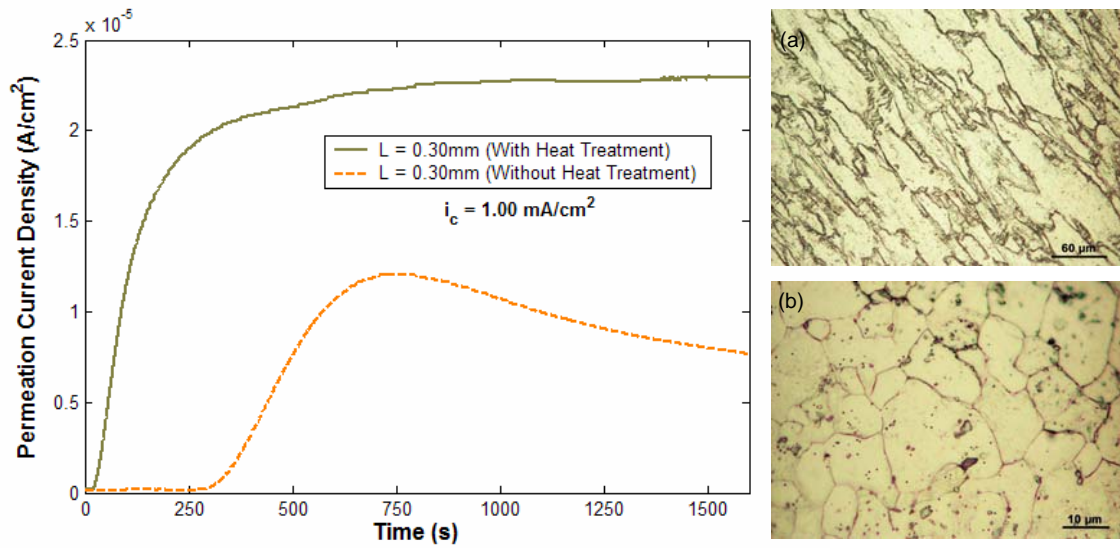


Figure 21: HP profile for (a) cold work (As-receive) and (b) with heat treatment (two hours to 600 °C), for $L=0.30$ mm (Armco-Fe).

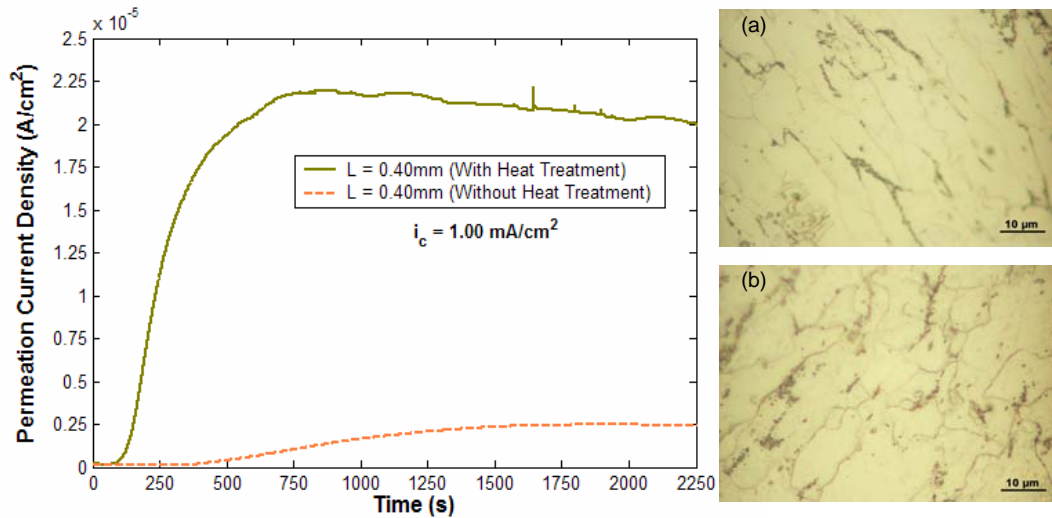


Figure 22: HP profile for (a) cold work (As-receive) and (b) with heat treatment (two hours to 600 °C), $L=0.40$ mm (Armco-Fe).

In samples without heat treatment shown in Figures 20 to 22, after reaching steady state, the permeation current tends to decrease, while for samples that have been heat treated this behavior is not observed.

The result for the samples with $L = 1.00$ mm (As-received thickness with hot rolling condition) subjected to a heat treatment (two hour to 600°C with air cooling),

followed by cathodic polarization in order to effectuate hydrogen permeation, similarly as with the other samples are shown in Figure 23 with corresponding micrographs.

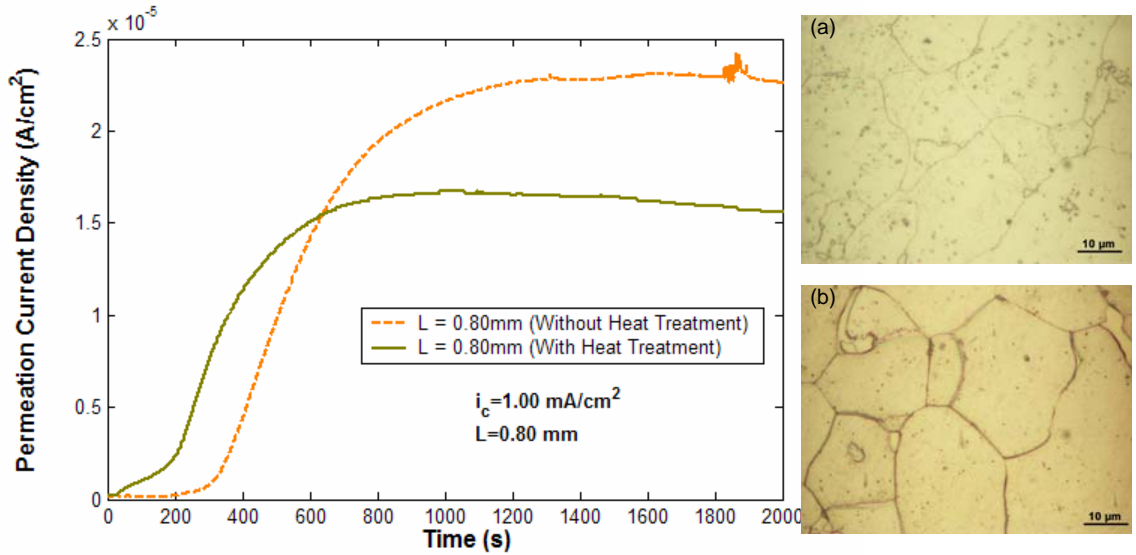


Figure 23: HP profile for (a) hot rolled condition and (b) additionally heat treatment (two hours to 600 °C), $L = 0.80$ mm (Armco-Fe).

3.1.6. Grain Dimension on Hydrogen Permeation

Figure 24 shows hydrogen permeation profiles, with same thickness but with variable grain size, samples have a prior heat treatment of, two hours at 600°C with air cooling condition.

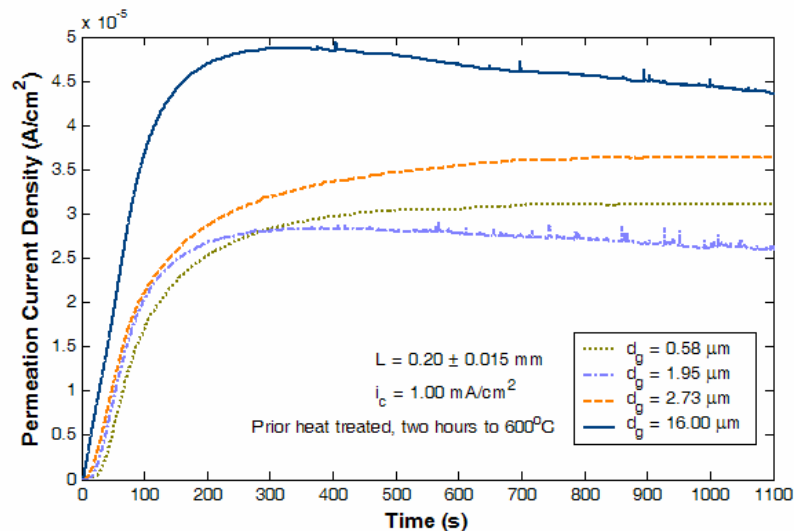


Figure 24: Hydrogen permeation profile (same thickness) with variable grain size (Armco-Fe).

3.1.7. Roughness Effect on Hydrogen Permeation

The surface roughness of a material has significant effect on hydrogen entry to the bulk, and therefore in permeation and diffusion processes as shown in Figure 25. There are significant variations with respect to breakthrough time which doubles approximately in value in each case. The maximum permeation current density decreases for samples with better surface finishing, while remaining invariable practically for roughness corresponding to 600, 400 and 320 grid respectively.

Figure 26 shows the topography of the area obtained for the given roughness values indicating the material removal. The values for the roughness corresponding to each grid, is shown in Table 6. In this experiment for comparison purposes, orientation of polished surface has been set in horizontal direction, and the quoted roughness based on ISO 4287/1 standard. Sample corresponding to the As-receive with hot rolled condition ($L = 1.00$ mm) and additionally heat treated (600°C for two hours with air cooled) was used. Note that the thickness changed after the process of polishing.

Table 6: Surface roughness for different degree of grid paper number (Armco-Fe).

Thickness (mm)	Final Step (Grid)	Roughness (R_q , nm)
0.80	0.05 μ (final polishing)	7.10
0.65	600	44.10
0.75	400	70.00
0.78	320	198.00

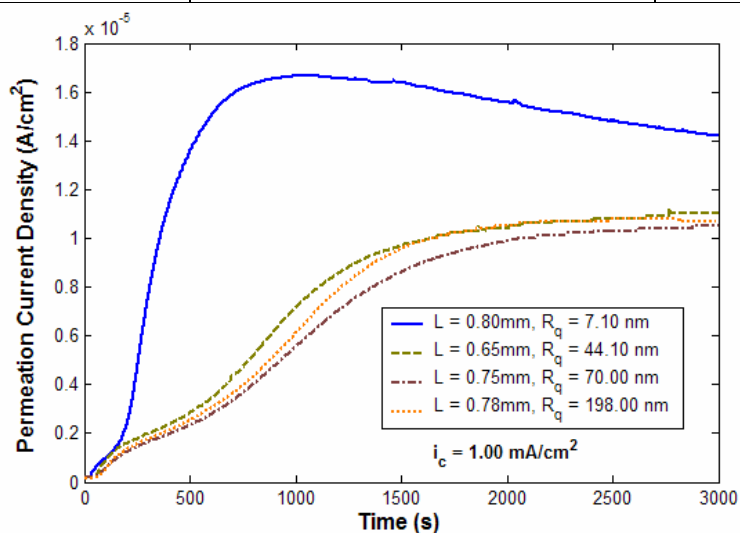


Figure 25: Profile of HP with different surface roughness.

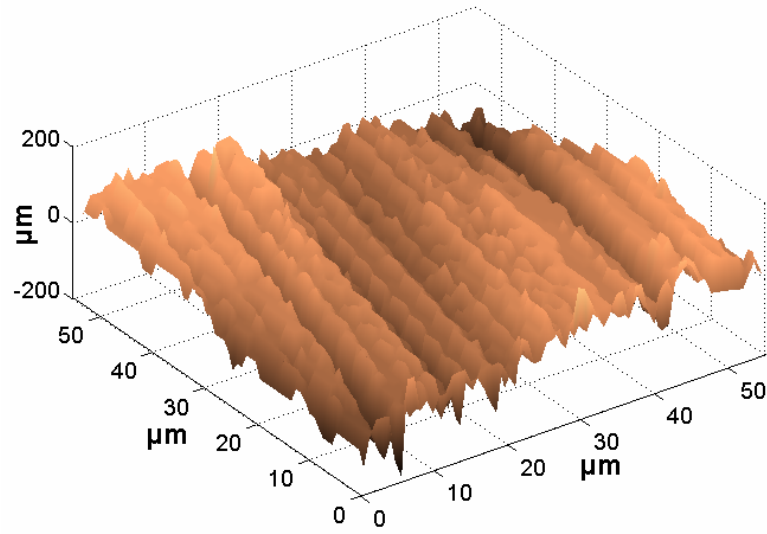


Figure 26: Atomic Force Microscope (AFM) generated surface topography ($R_q = 198.00 \text{ nm}$).

3.2. Hydrogen Permeation in AF1410 Steel

3.2.1. Determination of Optimal Charging Current for Hydrogen Permeation

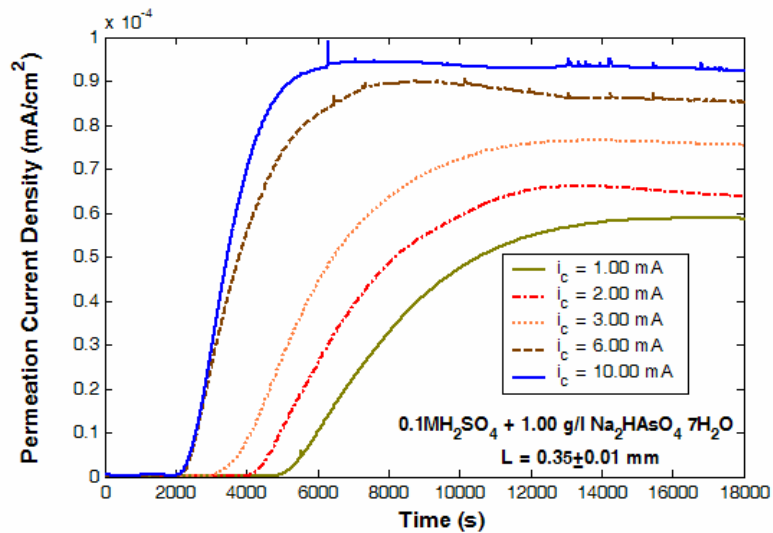


Figure 27: hydrogen permeation profile, with different charging condition (AF1410 steel).

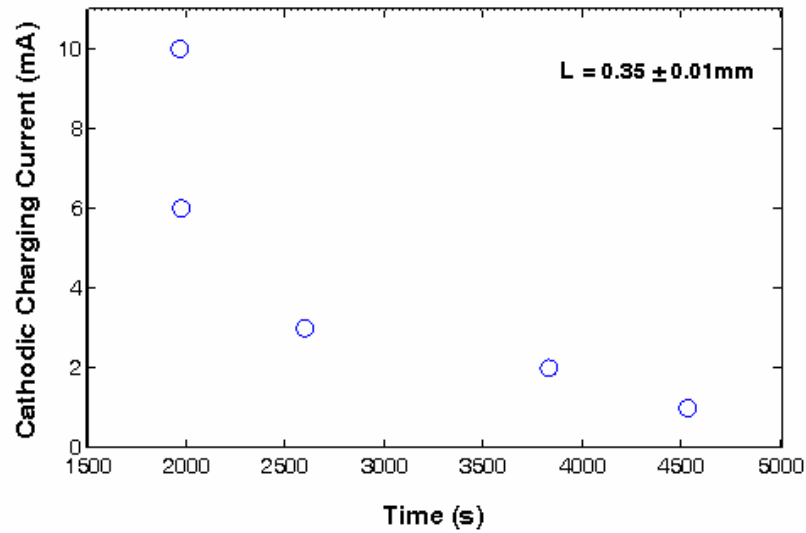


Figure 28: Hydrogen charging current vs. time (AF1410 steel).

In order to have a reliable charging process, there is need to have reproducible results following cathodic polarizations. Figure 27 shows the permeation profiles in AF1410 steel for different charging conditions similar to the case of Armco-Fe. In low charging conditions the breakthrough is high and the permeation profile is low, but when the charging load is increased, the breakthrough time tend to be maintained constant. When the charging current is high, the formation of blister in the material is more frequently. Figure 28 shows the diagram of charging current as a function of breakthrough time

3.2.2. Effect of Thickness on Hydrogen Permeation

Figure 29 shows the hydrogen permeations, with same charging condition ($i_c=2.00\text{mA/cm}^2$) for different material thicknesses. The principal observation here is the reduction in time to reach the steady state condition and with corresponding increase the section time to attain steady state condition.

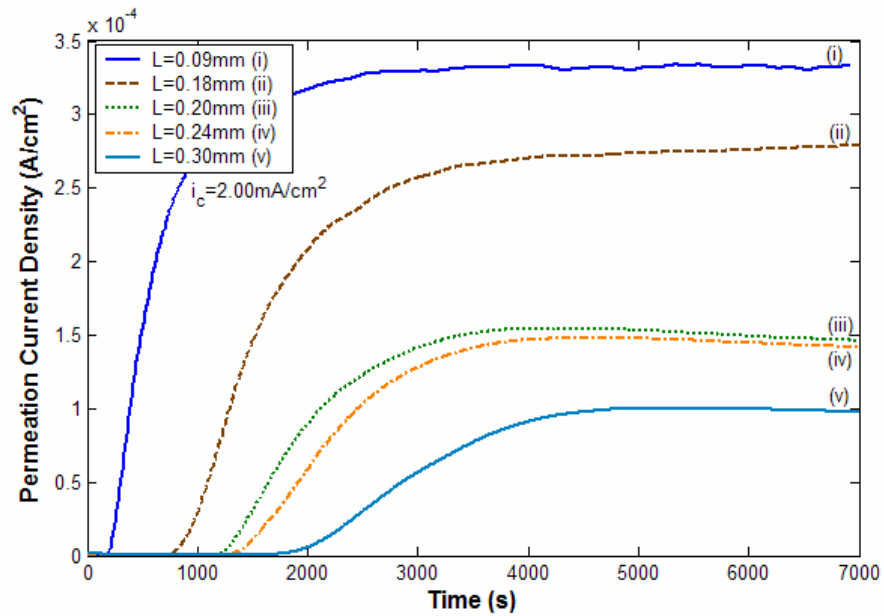


Figure 29, Hydrogen Permeation, for different thickness under same charging current (AF1410 steel).

3.2.3. Surface Roughness Effect on Hydrogen Permeation

Similar to Armco-Fe the effect of hydrogen rate ingress into the sample is affected by the surface finish of the sample. Table 7 shows the summary of the final paper grid used with corresponding value of roughness value based on ISO 4287/1 standard. The sample thickness is equal to 0.24 ± 0.01 mm. Figure 30 shows hydrogen permeation profile for different grades of surface roughness.

Table 7: Surface roughness for different degree of grid paper number (AF1410 steel).

Final Step (Grid)	Roughness (R_q , nm)
0.05 μ (final polishing)	10.00
600	39.20
320	127.00

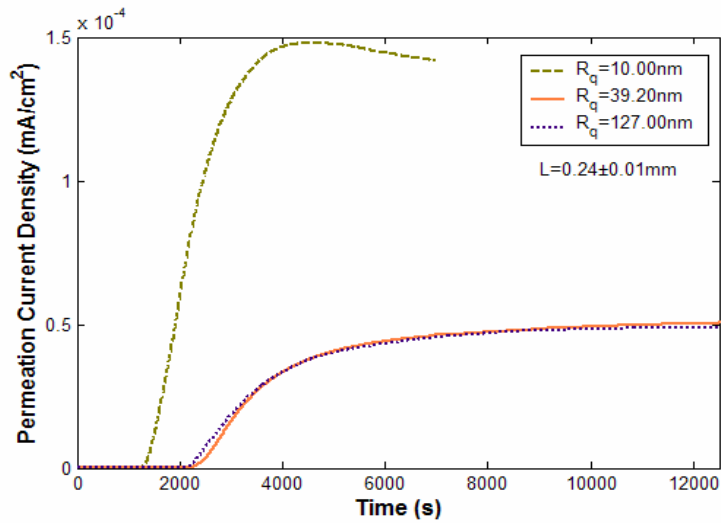


Figure 30: Hydrogen Permeation profiles, same thickness and variable surface roughness (AF1410 steel).

3.3. Hydrogen Charging of AF1410 Steel Compact Tension Specimen

Compact tension samples of AF1410 steel, measuring in thick approximately equal to 4.00 ± 0.3 mm, poses a great challenge to permeate because of the low diffusivity of hydrogen in this material. Furthermore in high current cathodic charging condition, the charged surface suffers severe damage such as, pitting formation (for long charging time). To perform the hydrogen charging process the following parameters were used: current density of 0.3 mA/cm^2 for 234 hours in a solution of $0.1 \text{ M H}_2\text{SO}_4 + 1 \text{ g/l}$ sodium arsenate. The charging time was determined based on visual observation to avoid the charging surface damage.

3.4. Fatigue Crack Propagation in AF1410 Steel

Figure 31 shows the crack growth rate (da/dN) as function of crack length for both conditions (in **air** and with prior electrochemical **cathodic hydrogen charging**). This was performed under COD controlled test condition in order to obtain a comparative behavior of the AF1410 steel under fatigue test subjected to those conditions mentioned above.

Figure 32 shows the crack growth rate (da/dN) as a function of $K_{I\max}$, obtained for both testing conditions (air and with prior hydrogen). To develop these tests materials previously subjected to pre-crack is used in order to obtain a good result. These test were conducted in collaboration with one of my colleagues (**Ms. Amilcar Quispitupa Yupa**) who also a Ph. D candidate.

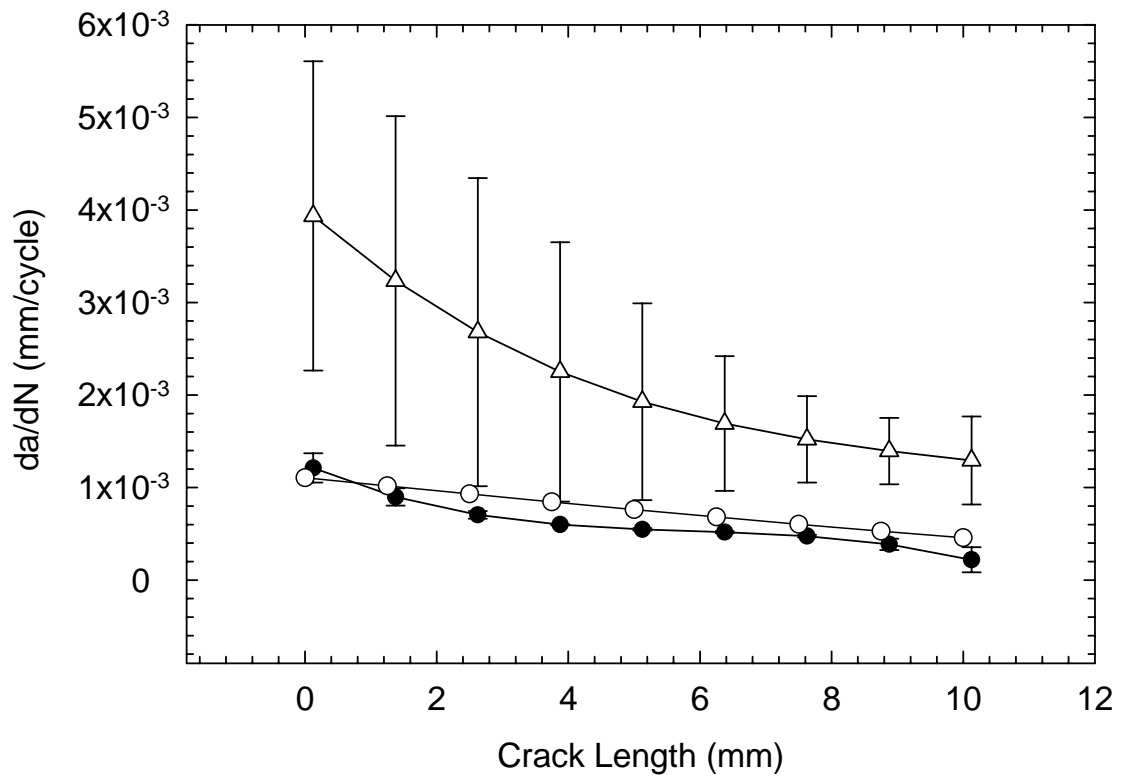


Figure 31: crack growth rate (da/dN) as function of crack length ($R=0.4$).

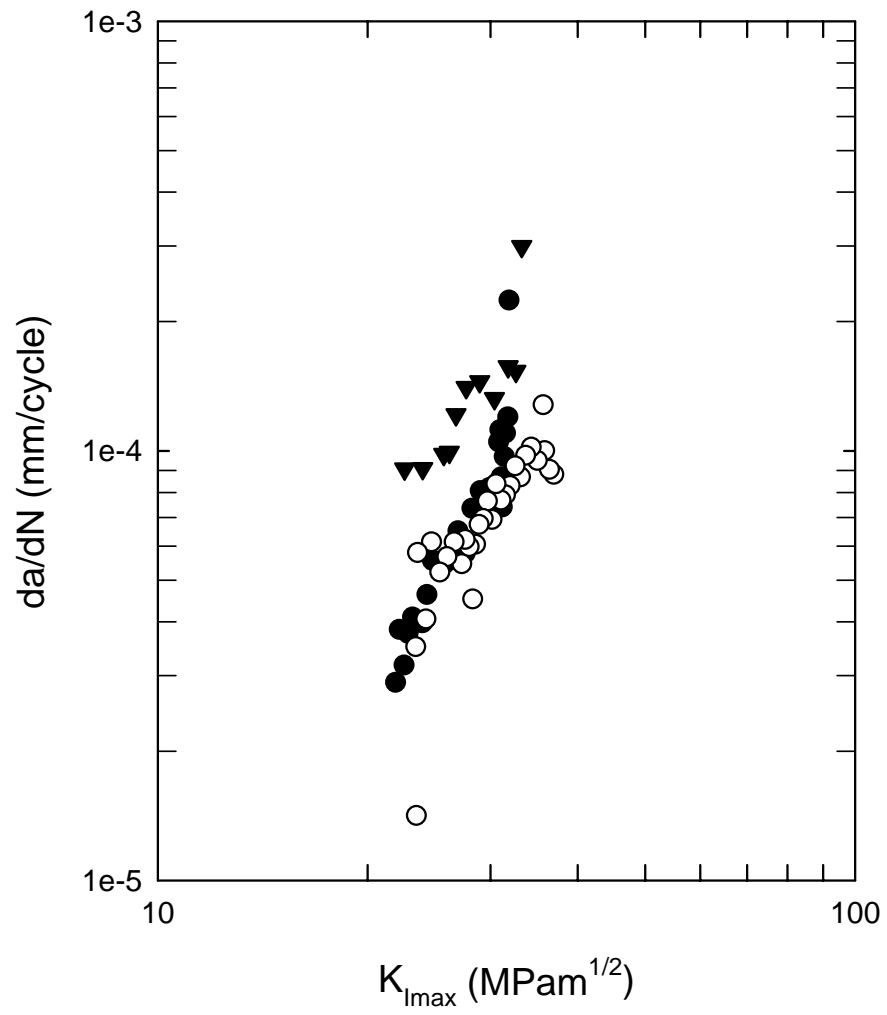


Figure 32: Crack Growth rate (da/dN) as a function of $K_{I_{max}}$ ($R=0.4$).

4. DISCUSSION

4.1. Hydrogen Permeation (HP) on Armco-Fe

4.1.1. Effect of Solution and Poison Concentration on HP

As indicated earlier, the poison is a promoter that has effect of accelerating hydrogen ingress or entry to the bulk as shown in Figure 15. There are different theories used to describe this phenomenon, i.e. how the promoters act. One of these was proposed by Bockris and Conway and described by Newman [18]. They postulate that an increase in hydrogen permeation can be explained by a decreasing in the strength of the M-H bond, caused by the electrostatic attraction between a negatively charged anion and a positively charged hydrogen atom. This reduction in strength is caused by Arsenic (As) on the surface and further AsH_3 that can evacuate in gas form. If the concentration of promoter is relatively low (0.25 g/l and 1.00 g/l as shown in Figure 15), the amount of hydrogen permeation will be high, but if the concentration of promoters in the solution increased (10.00g/l), the amount of hydrogen permeated reduces. Figure 33 shows how the promoters aid in the acceleration of the entry of hydrogen to the material. When the concentration of As in the solution is low the surface coverage of the promoter is relatively low, while if the concentration increases the element covers the surface, and thereby act as a wall. As shown in the profile in Figure 15, the process of acceleration decreases. The effect of poison is only to accelerate the process, as can be deduced with charging with 0.10M H_2SO_4 without poison. In this case steady state is reached closely to same level as with concentration (0.25g/l and 1.00 g/l) while the time to accelerate it is long (approximately 20000.00 seconds); which verifies the initial postulation.

Each profile shows the following peculiarity: when the potentiostat begins to record hydrogen in the exit side, this tends to increase to some level and after a brief stabilization period there is rapid increase until the maximum permeation level state, explained by the presence of high concentration of reversible trap due to the presence of unstable grains that act as potentially reversible trapping sites as shown in the micrograph of Figure 23 b. This phenomenon is shown in the mathematical model develop by Iino [4], where the delay for the capture rate per trap is greater than the

release rate per trap in the first 200 seconds for low concentration poison, while for high concentration this time is increased to 1000 seconds. In the absence of promoters, this time is very long, as shown experimentally reaching 5000.00 seconds approximately.

The type of solution (on the entry side), have a different effect in permeation by the pH condition. Figure 14 shows the comparison between the permeation profiles with two kinds of solution, the permeation profile for alkaline solution have an unsteady behavior with the resultant apparent solubility low, probably the small amount of hydrogen generated on the surface and consequently ingress into the material. This condition does not give a good approximation to determine the hydrogen diffusivity (diffusion coefficient) and permeability of a given material

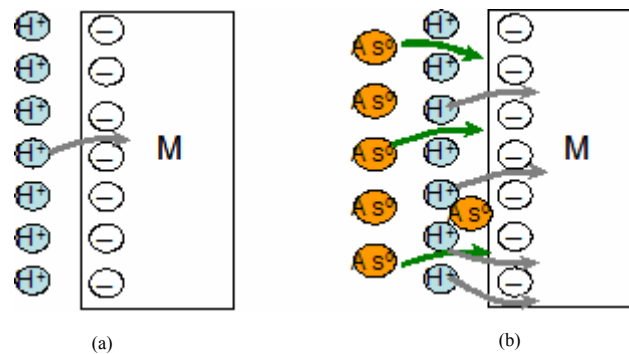


Figure 33: Effect of promoter in hydrogen charging; (a) without promoter, (b) with promoter.

4.1.2. Effect of Kind of Promoter on HP (Armco-Fe)

Amount of hydrogen permeating through a sample (same characteristic), depends on hydrogen ingress in the input side. This parameter is studied using different kinds of promoters, for varying concentrations. Figure 16 shows the hydrogen permeation profiles for different types of promoter with two concentrations for each one. Thiourea (NH_2CSNH_2) in high concentration (10.00 g/l) has a significant effect in rate of hydrogen ingress in the material decreasing when the concentration is low. With respect to sodium cyanide (NaCN), it does not have a significant effect in the hydrogen permeation as it is possible to observe a little increase in the rate for low concentration (1.00g/l NaCN)

The effective kind of promoter with 0.1M H_2SO_4 (pH = 1.2) for best hydrogen ingress rate in the material is sodium arsenate ($Na_2HAsO_4 \cdot 7H_2O$) with concentration range of (0.25-1.00g/l) as show in Figure 16. In each profile shown, one observes that after a short time after the detection of the first hydrogen in the exit side, a stabilization (the stabilization time depends of the kind and concentration of promoter), period followed by a rapid increase. This is due to the high concentration of reversible trapping sites as explain earlier.

4.1.3. Effect of Thickness on HP (Armco-Fe)

Hydrogen, have easy mobility when the material is a thin film, than in materials that have a considerable thickness where its mobility is reduced, and the time from release of trapping is increased, as shown in the permeation profiles in Figure 19. The significant reduction in time to reach the steady state and considerable increase of breakthrough time, affect the diffusion parameter. With increasing thickness the diffusion parameter decreases in an exponential form. To obtain the diffusion coefficient it is possible with different methods such as, the slope and breakthrough time methods as summarized in Table 8. To determine the breakthrough time the explanation is given in the appendix. For the slope method the ASTM G-148-97 standard [13] was adopted which yields the apparent diffusivity which can be calculated from the plot of $\log(J_\infty - J(t))$ in the y axis and in the x axis the $1/t$ (as shown in Appendix 7.2). From this plot, one obtains a linear slope which corresponds to $L^2 \log(e)/4D$, which is but an approximation. Figure 34 details the apparent hydrogen diffusion coefficient variation based on the methods utilizing the different criteria. To check the values obtained (D), it is necessary to compare the experimentally recorded profile with the mathematically derived curves based on theory.

Table 8: Summary of diffusion coefficient with breakthrough time and slope method (Armco-Fe).

Cathodic Current (i_c , mA/cm ²)	Thickness (L, mm)	Breakthrough Time Method		Slope Method	
		(t_b , s)	Diffusion (D_{app} , cm ² /s) x10 ⁻⁵	Slope	Diffusion (D_{app} , cm ² /s) x10 ⁻⁵
1.00	0.40	5	2.09	7.335	2.37
1.00	0.55	11	1.79	17.847	1.84
1.00	0.65	16	1.72	28.256	1.62
1.00	0.80	30	1.39	46.810	1.48

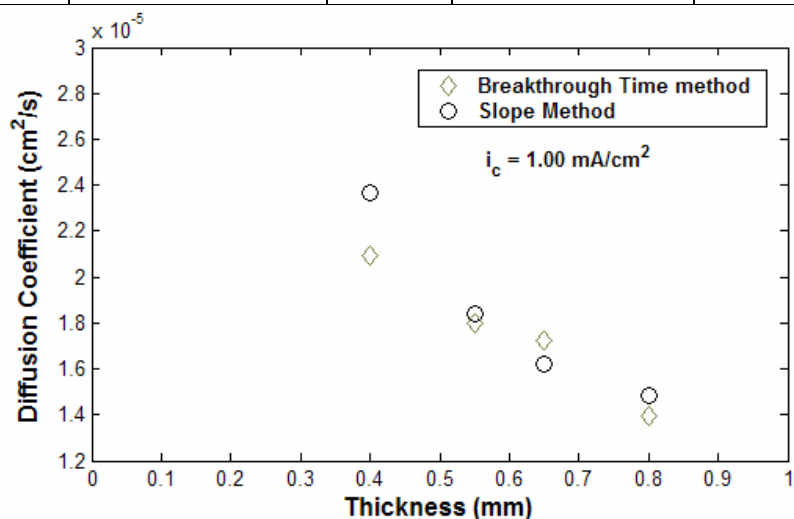


Figure 34: Diffusion coefficient with respect to sample thickness (with previous heat treated two hours to 600°C, with air cooling) (Armco-Fe).

Trap binding energy is possible to be determined, by taking equation (1) where the D_{app} is the diffusion calculated by breakthrough method or slope, with R and T known. Kiuchi and Mclellan [27] made statistical analyses of literature available different previous values obtained by other investigators and concluded that the best value of D_L for Armco Fe is 7.23×10^{-4} cm²/s. The values obtained for E_t are shown in Table 9. In our case we used the D_{app} obtained by the breakthrough time, because of the good fitting with the mathematical model as will be explained much later.

Table 9: Hydrogen trap binding energy for Armco-Fe.

Thickness (L, mm)	Trap Binding Energy (E_t , KJ/mol)
0.40	8.72
0.55	9.10
0.65	9.20
0.80	9.72

The values obtained show that the trapping energy increased with increasing material thickness. This is because, there are possibly more than one path way for the hydrogen transport. Thus, for hydrogen at the surface or at the center of the material to diffuse, increased material thickness will result to increased trapping sites, and therefore more work needed for hydrogen transport. This implies higher trap binding energy with increasing material thickness

4.1.4. Effect of Cold Work on HP (Armco-Fe)

The permeation profiles for material thicknesses 0.20, 0.30, 0.40 mm are displayed in Figures 20, 21 and 22 respectively, showing the significant effect of cold work (as receive material). As is seen when the sample is in cold rolled condition, the amount of hydrogen permeating through it is low, with the maximum permeation rate of hydrogen for 0.20 mm, equal to $J_{\max} = 8.55 \times 10^{-6} \text{ A/cm}^2$. As indicated earlier after attaining the maximum hydrogen permeation rate, it's value tends to decrease. This tendency is similar for all the material thicknesses. One of the effects or consequences of cold rolling process is the increase in the dislocation density, which acts as irreversible traps sites. Shortly after the beginning of the hydrogen charging, the dislocation sites are filled with hydrogen in greater part in molecular form which mixes in some cases with other impurities in stable configuration. These act like a wall such that they do not permit hydrogen permeation and so, the hydrogen that arrive in atomic or ionic forms continue to be accumulated especially near the charging surface, until forming a blister. Experimental observations show that blisters begin to form after attaining the maximum value of permeation current, which is followed by decrease in the permeation current, thereby allowing us to relate the two effects.

To obtain the apparent diffusivity, we used the two methods based on the breakthrough time and slope, which are shown in Table 10 in summarized form.

Table 10: Comparison of hydrogen diffusion coefficient in cold work and heat treatment samples in different thickness (Armco-Fe).

L, (mm)	Breakthrough Time				Slope Method			
	Cold Rolled		Heat Treatment (600°C/2hr/Air cold)		Cold Rolled		Heat Treatment (600°C/2hr/Air cold)	
	t _b , s	D _{app} , cm ² /s	t _b , s	D _{app} , cm ² /s	Slope	D _{app} , cm ² /s	Slope	D _{app} , cm ² /s
0.20	170	1.54 x10 ⁻⁷	18	1.45 x10 ⁻⁶	19.104	2.27 x10 ⁻⁶	27.423	1.58 x10 ⁻⁶
0.30	300	1.96 x10 ⁻⁷	20	2.94 x10 ⁻⁶	303.06	3.22 x10 ⁻⁷	31.759	1.58 x10 ⁻⁶
0.40	400	2.61 x10 ⁻⁷	120	8.71 x10 ⁻⁷	408.77	4.25 x10 ⁻⁷	46.81	1.02 x10 ⁻⁶
0.80	320	1.31 x10 ⁻⁶	30	1.39 x10 ⁻⁶	567.24	1.23 x10 ⁻⁶	46.81	1.48 x10 ⁻⁵

The diffusion coefficient is a measure of ease of hydrogen movement or transport in a material. If the material has high density of dislocations as a consequence of cold work, these sites will reduce the diffusivity of hydrogen by the effect of irreversible trapping as mentioned earlier.

Another parameter that impact hydrogen transport is the effect of grain size. The samples obtained were of different thickness with each having a particular microstructure. The following Table 11 shows the list of samples with corresponding grain sizes (corresponding to materials that have been heat treated).

Table 11: Diffusion coefficient (breakthrough method) as a function of grain size (after heat treatment).

Thickness (mm)	d _g (μm)	Diffusion (D, cm ² /s)
0.20	0.58	1.45 x10 ⁻⁶
0.30	1.95	2.94 x10 ⁻⁶
0.40	2.37	8.71 x10 ⁻⁷
0.80	16.00	1.39 x10 ⁻⁵

Hydrogen diffuses within the unit cell and after reaching the grain boundaries; they are retained thereby spending more time than in the initial case, and subsequently suffer low diffusivity and permeation. Since grain boundaries act as irreversible trapping sites, then hydrogen tend to recombine and form molecules within the grain boundaries. Therefore if the specimen has a small grain size, the grain boundary length (the grain boundary area) increases, then the trap density sites increase and hence a decrease in the diffusion coefficient. As a consequence of increasing trapping sites (dislocation and grain boundary), the trap binding energy is increased. The trap binding energy as a function of material thickness for different thermodynamic condition is summarized on Table 12.

Table 12: Trap binding energy as a function of material thickness and thermodynamic state (Armco-Fe).

Thickness (L, mm)	Trap Binding Energy (E_t , KJ/mol)	
	Cold Work	Heat Treatment
0.20	20.81	15.29
0.30	20.22	13.55
0.40	19.518	16.55
0.80	15.54†	9.72

†: Hot rolled condition

The binding energy for as received samples (cold worked) is higher in comparison to same samples following heat treatment. This behavior is for the samples that have a small grain size where the binding energy is higher than materials with large grain size. It is important to know that with increasing thickness of materials, there is also increase of trapping sites, and consequently, increase in the trap binding energy.

4.1.5. Grain Dimension in Hydrogen Permeation (Armco-Fe)

Table 13 shows the hydrogen diffusivity obtained with breakthrough time method, as a function of grain size (same thickness with $L = 0.20 \pm 0.015$ mm). It is evident that the diffusivity suffers a reduction when the grain size is smaller. The grain boundaries act as irreversible trapping sites consequently if the grain size is small the grain boundary increases, which then affect the hydrogen diffusion and permeability. The maximum permeability reached in sample with $d_g = 16.0 \mu\text{m}$ is two times higher than in samples with $d_g = 0.58 \mu\text{m}$, as shows in Figure [24].

Table 13: Hydrogen diffusion coefficient as a function of grain size, with same thickness ($L = 0.20 \pm 0.015$ mm) for Armco-Fe.

d_g (μm)	t_b (s)	D_{app} (cm^2/s)
0.58	18	1.45243E-06
1.57	13	2.01106E-06
2.37	10	2.61438E-06
16.00	1	2.61438E-05

To determine a relation between the grain size and diffusivity, it is possible to make a logarithmic regression as shown in Figure 35 with the intersection as

$\ln(C) = -13.301$, then $n = 0.9144$ is the regression line slope, corresponding to the equation of the form $D_{app} = Cd_g^n$. Substituting the relevant values, one obtains:

$$D_{app} = 1.67 \times 10^{-5} d_g^{0.9144}.$$

This is similar to the previous case where equation 1 was used to determine the trap binding energy, as shown in Table 14

Table 14: Trap binding energy as a function of grain size, with same thickness ($L = 0.20 \pm 0.015 \text{ mm}$) (Armco-Fe).

d_g (μm)	D_{app} ($\text{cm}^2/\text{s}) \times 10^{-6}$	Trap Binding Energy (E_t , KJ/mol)
0.58	1.45	15.38
1.57	2.01	14.58
2.37	2.61	13.93
16.00	26.14	8.22

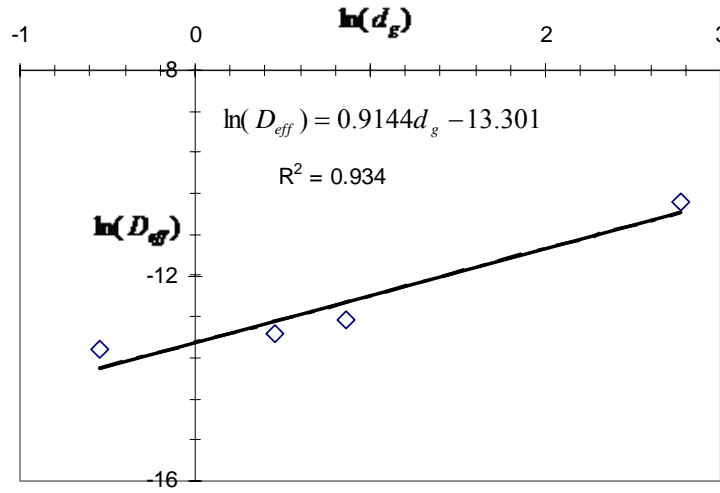


Figure 35: Logarithmic regression of grain size with respect to diffusion coefficient.

4.1.6. Roughness Effect on HP (Armco-Fe)

Figure 25 shows the hydrogen permeation profile with different surface characteristics (roughness). The breakthrough time in all of them is affected being increased. When the profile is increased with the curve shifting to the right, it then reaches a maximum level, and remains constant there after. Though the thicknesses obtained by the polishing process are not the same, the permeation profiles are seen to be

similar with little difference in the breakthrough time of 10s. Thus the breakthrough times must be related to the materials thicknesses as shown in Table 15 indicating these variations with respect to roughness.

Surface roughness is an imperfection associated with material processing and is characterized by different degrees of crest and valleys (maximum and minimum). When hydrogen is generated at the surface of a material, it tends to form pockets or bubbles of molecular hydrogen (H_2), there in as shown in Figure 36; because the gas is not evacuated quickly as in the case of highly polished surfaces with small roughness. Then the bubbles of H_2 will act like a wall preventing hydrogen atoms further entry into the material bulk.

Table 15: Roughness effect on hydrogen permeation (Armco-Fe).

Thickness (L, mm)	Roughness (R_q , nm)	Breakthrough Time (t_b , s)	J_{max} (A/cm^2) $\times 10^{-5}$
0.8	7.10	30	1.66
0.65	44.10	50	1.10
0.75	70.00	60	1.08
0.78	198.00	60	1.06

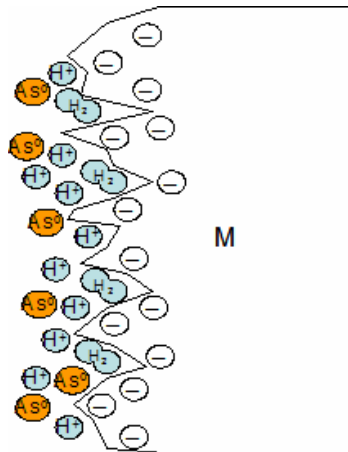


Figure 36: Effect of surface roughness on hydrogen entry to sample.

4.2. Hydrogen Permeation on AF1410 Steel

As in the case of Armco-Fe the microstructure is a critical parameter that affects the hydrogen diffusion and permeation properties. AF1410 steel is a multiphase material with diverse alloying elements. Figure 37 shows the etched surface of the AF1410 steel of this study. Previously Antolovich's [21] study showed the detailed microstructure of AF1410 steel. After age hardening at $950\pm 10^\circ\text{C}$, the material consisted of a highly dislocated lath martensite, with a small amount of stringer like retained austenite at the interlath boundaries. Furthermore the precipitates are shown being very fine, and are located in the interior of the lath and between the lath. These particles were small sized, and so they concluded that the precipitation agent at the indicated temperature of treatment produced a fine $(\text{MoCr})_2\text{C}$. These (small size) finely dispersed particles seem to nucleate at dislocation.

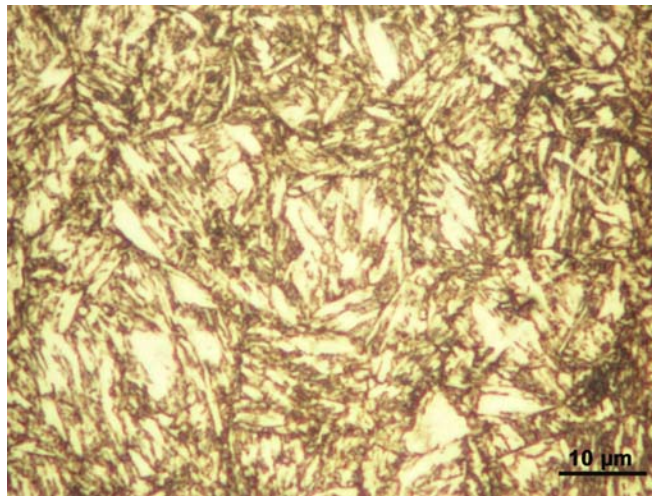


Figure 37: Microstructure of AF1410 steel.

4.2.1. Optimal Charging Current (AF1410 Steel)

Similar to the case of Armco-Fe, it is first necessary to determine the optimal cathodic charging condition. For the AF1410 steel the solution used is the same as in the case Armco-Fe. Figures 27 and 28 show the hydrogen permeation profiles for different charging conditions for the same material thickness. In experiments with low charging

current, the breakthrough time was observed to be long while the steady state value is low. The breakthrough time increases with the charging current and tends to stabilize approximately at 4.00 mA (see the Figure 28). According to these the optimal charging currents was determined to be approximately equal to 4.00 mA, for a charging surface area of $A_c = 1.89 \text{ cm}^2$ which for convenience is taken to be 2.00 mA/cm^2 . Other parameters that help in determining the optimal charging condition is the formation of blister at the surface. As in the case of Armco-Fe, with high charging current it is observed that relative small amount of these forms. Furthermore with high charging current condition and at prolonged times, one observes the formation of pitting on the surface of the samples.

4.2.2. Effect of Thickness (AF1410 Steel)

Similarly as in the case of Armco-Fe the thickness of the material has an effect on the permeation profiles as shown in Figure 29. Based on the profile and the influencing parameter the diffusion coefficient based on slope method is shown summarized in Table 16.

Table 16: Hydrogen diffusion coefficient based on the slope method (AF1410 steel).

Thickness (L, mm)	Slope	D (cm^2/s) $\times 10^{-8}$
0.09	174.17	5.05
0.16	823.92	3.37
0.18	1206.8	2.91
0.20	1709.2	2.54
0.24	3217.80	1.94
0.30	6400.00	1.53

Diffusion coefficients obtained by breakthrough time and time lag do not follow a defined correlated pattern. Since the transient build up for Armco-Fe is steeper than for AF1410 steel, and also, the transient portion for AF1410 steel is more “sigmoid” shaped, therefore, one can project two tangents depending on choice, for instance, if one chooses the first rise in transient, or the later rise in transient. One way of obtain an approximate breakthrough time is by drawing a line in the linear part of permeation transient and projecting until it intersects the time axis. We take this value as t_b , (approximately but it

is not guaranteed as the best value). For the time lag method, once steady state (J_{∞}) is reached there is a little variation (if not stabilized completely), this small variation leads to a large range of possible selection of the values of time lag (the time variation in both cases can be 50 to 200 seconds).

The diffusion coefficient obtained with the slope method is the most reasonable because in this case most of the data points are used (all linear transient part) in the estimation. Figure 38 shows the diffusion parameter obtained as a function of sample thickness. Similar to the case of Armco-Fe, the diffusion coefficient decreases when the material thickness increases. This is due to increase of trapping sites, or mostly due to the normal lattice sites behaving as trapping sites being predominantly near or in the middle of sample or membrane.

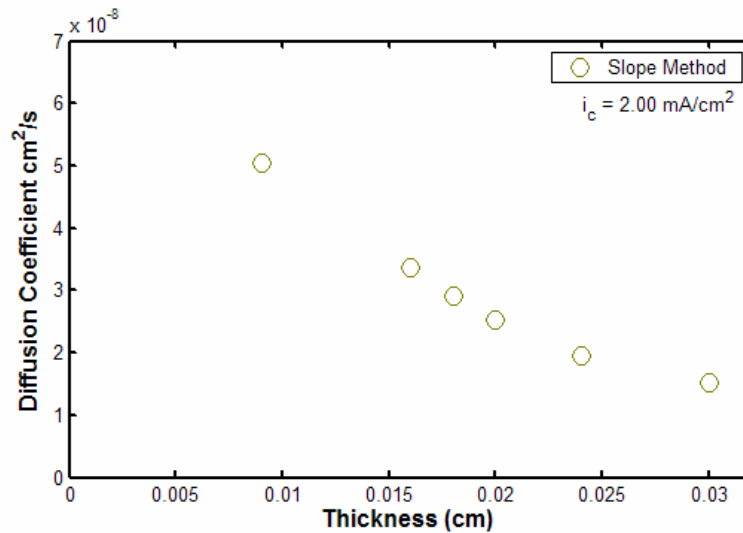


Figure 38: Hydrogen diffusion coefficient as a function of sample thickness, based on the slope method (AF1410 steel).

4.2.3. Roughness Effect on Hydrogen Permeation

Similar to Armco-Fe, it is clear see to the effect in increasing the breakthrough time and reduction of maximum attainable rate of hydrogen permeated. Of Figure 30 shows hydrogen permeation profile for two grades of surface roughnesses, i.e., samples with $R_q=39.20$ and 127.00 nm (600 and 320 final grid path). The profile are similar, however there is a small difference in breakthrough time (40.00seconds) only. Compared to the HP profile for the sample with $R_q=10.00$ nm (final polish process with $0.05\mu\text{m}$ of

alumina suspension), the breakthrough time increases approximately to 60%. The reason of this behavior is the rate of hydrogen ingress into the material which is reduced by the formation of molecular hydrogen as explained earlier in the section for Armco-Fe.

4.3. Models to Verify the Hydrogen Permeation and Diffusion Coefficient (from Experiment)

4.3.1. Armco Fe

To solve the Fick's equation we considered two charging conditions, the potentiostatic and galvanostatic method. In the potentiostatic condition we assume that the concentration is maintained constant at $x = 0$; while for galvanostatic condition, the concentration is known to change. Applying equations 5 and 8 [25, 26] one can show how the concentration profile varies as a function of the dimensional term ($\tau = Dt / L^2$) as seen in the Figures 39 and 40. For potentiostatic condition the steady state is reached when the value of $\tau \geq 1.00$, while in the galvanostatic mode steady state is reached with $\tau \geq 3.00$. According to the last deduction, time taken to reach solubility limit in the potentiostatic mode is three times less than in galvanostatic mode.

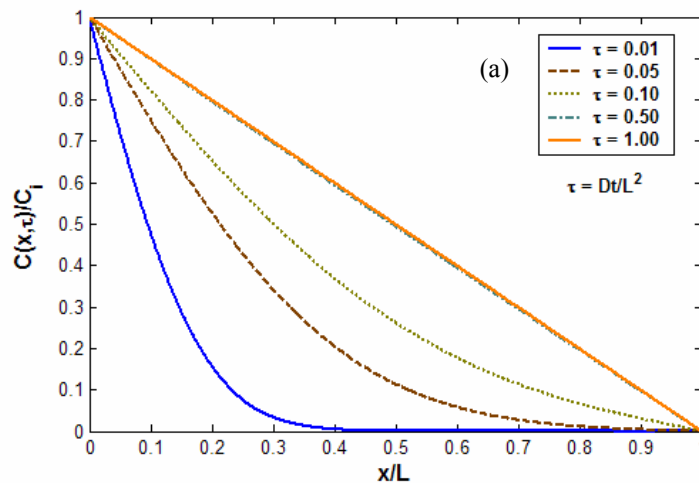


Figure 39: Hydrogen concentration profile in permeation based on the Potentiostatic mode (equation 5).

(b)

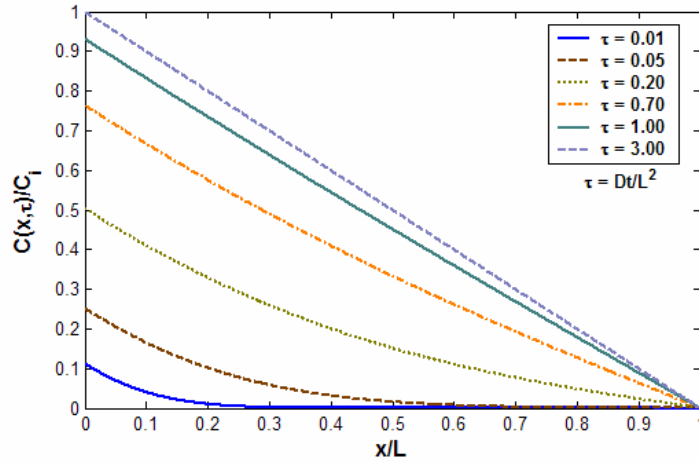


Figure 40: Hydrogen concentration profile in permeation based on the Galvanostatic Mode (equation 8).

To obtain the permeation profile we can apply the first Fick's law equations as show in chapter 1. Figure 41 shows the permeation profile for experimental data and compared to the model equations obtained for both conditions (potentiostatic equation (6) and galvanostatic equation (9)). The diagram shows that the galvanostatic condition compared to the model have a best fit, from which we could verify the initial supposition about the variation of concentration of hydrogen at $x=0$.

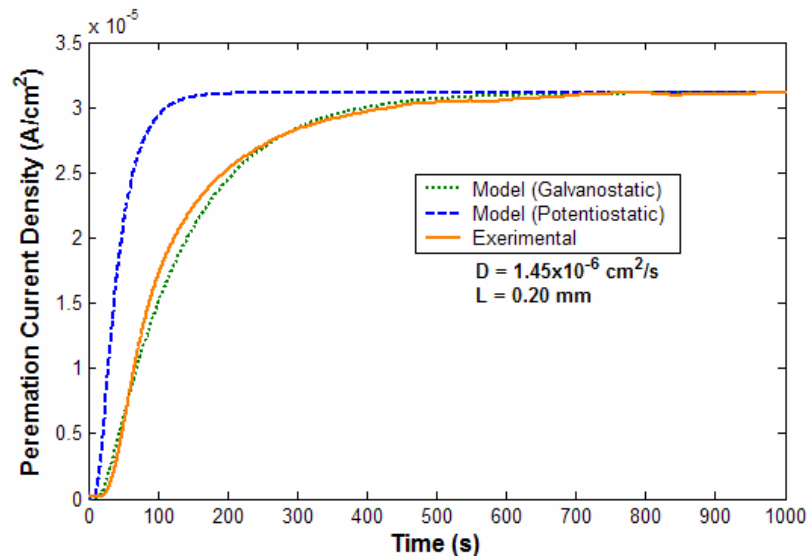


Figure 41: HP Comparison of experimental result and the models, for $L = 0.20$ mm thick material (Armco-Fe).

Table 10 shows the diffusion coefficient obtained with the two methods of breakthrough time and slope technique. In samples which have high diffusion coefficient and small thickness, the D obtained by breakthrough time have a best fit to galvanostatic charging condition as shown in Figures 41 and 42.

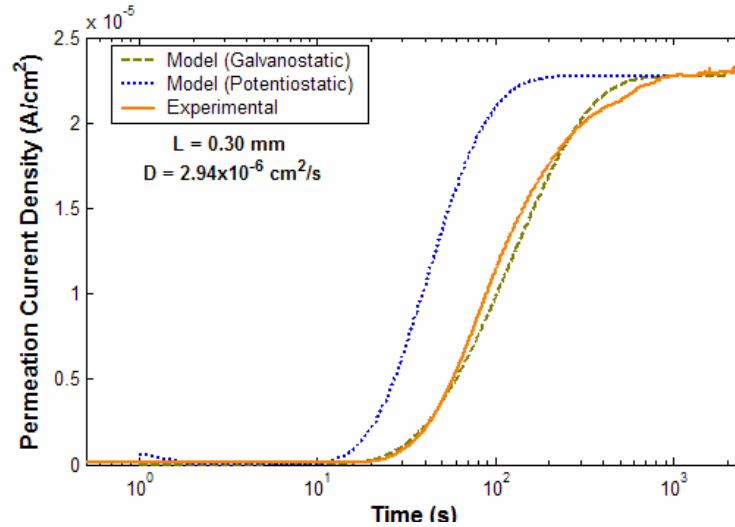


Figure 42: HP Comparison of experimental results and the models for $L = 0.30$ mm thick material (Armco-Fe).

The samples with initial thickness $L = 1.00$ mm (as-received hot rolled condition), were heat treated to ensure a fully annealed state. Micrographs show that the grain dimension is rather big ($d_g = 16.0 \mu\text{m}$) and also, that most of the grains are still under evolution, and consequently unstable (see Figure 23 b). These provide sites which act as potentially reversible trapping sites as explained earlier. In hydrogen permeation profiles the effect of these reversible trap sites can be seen as shown in Figure 43.

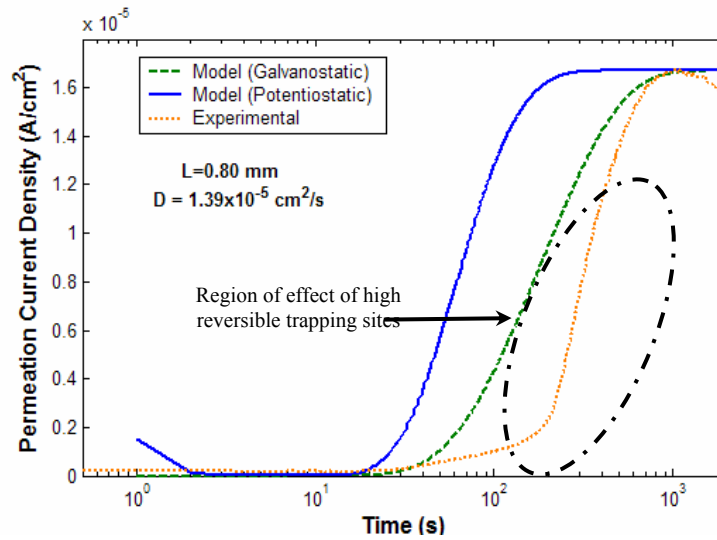


Figure 43: HP Comparison of experimental results and the models for $L = 0.80$ mm thick material (Armco-Fe).

4.3.2. AF1410 Steel

Table 16 shows the value obtained for diffusion coefficient, where the best fit is obtained by slope methods, as shown in the Figures 44-47. In permeation, the time taken to reach a steady state is long (depends on sample thickness and diffusivity). However the experimental observation indicated that the time taken for hydrogen concentration to be stabilized in the charging surface is approximately 1000 seconds for each sample. The last observation showed that after 1000 seconds the concentration in the charging surface behaves as in the potentiostatic form. Figure 44 shows comparison of the experimental data and models of hydrogen permeation for $L = 0.09$ mm in the galvanostatic mode clearly. Figure 45 for samples with $L = 0.16$ mm shows the fitting is closely to the potentiostatic mode, and similarly for $L = 0.18$ mm and $L = 0.20$ mm respectively. The model does not have a good approximation (fitting) for samples with $L \geq 0.24$ mm .

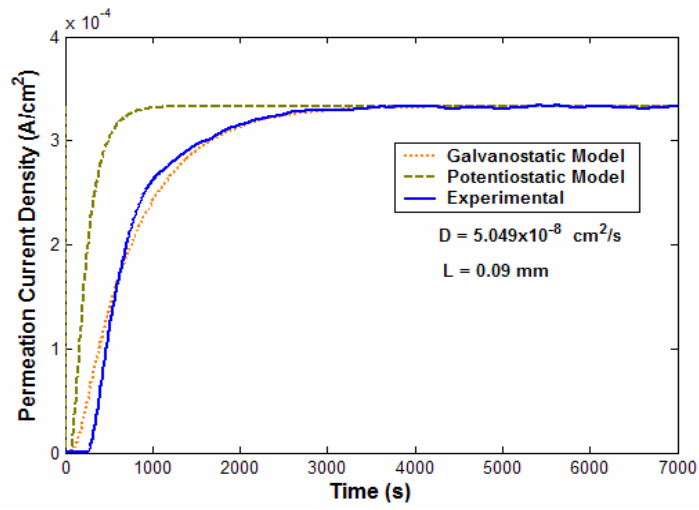


Figure 44: HP comparison of experimental results and model for $L = 0.09$ mm thick material (AF1410 steel).

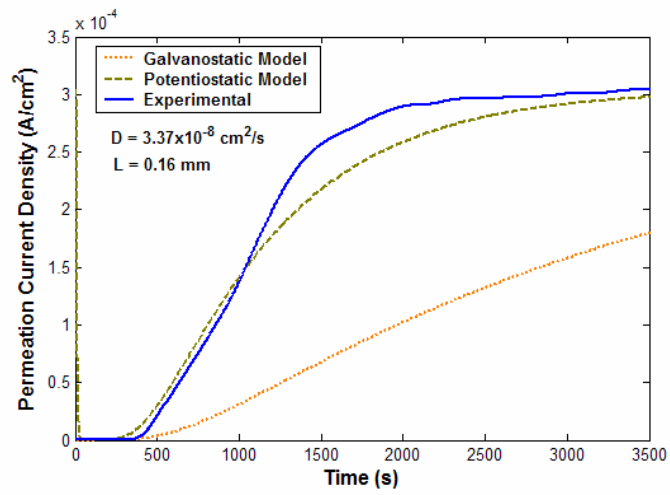


Figure 45: HP comparison of experimental results and the model for $L = 0.16$ mm thick material (AF1410 steel).

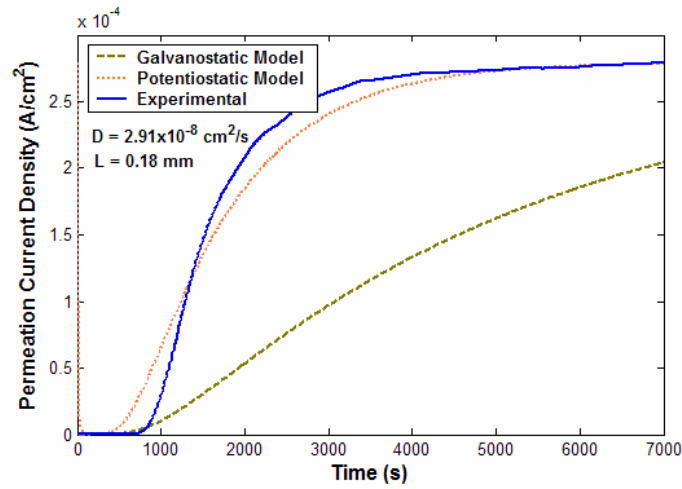


Figure 46: HP comparison of experimental results and the models for $L = 0.18$ mm thick material (AF1410 steel).

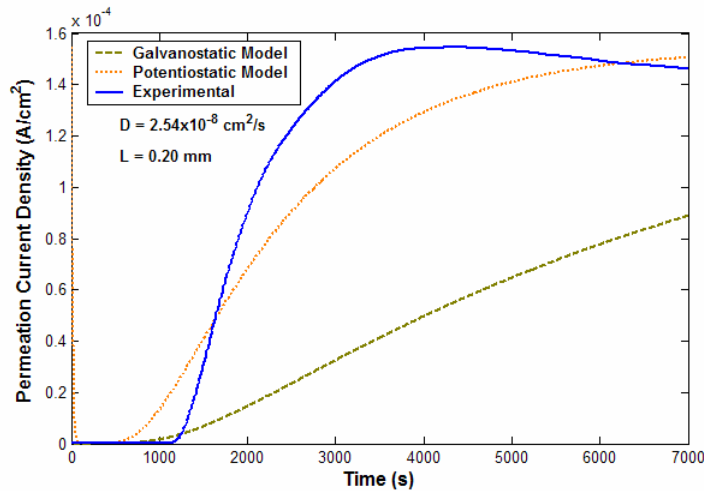


Figure 47: HP comparison of experimental results and the models $L = 0.20$ mm thick material (AF1410 steel).

4.3.3. Hydrogen Concentration on Charging Surface

4.3.3.1. Armco-Fe

It is important in monitoring the potential changes during the charging of surface to estimate approximately the hydrogen concentration. As indicated initially the charging behavior is in better agreement with the galvanostatic form, and after a certain time when, hydrogen reaches saturation at the charging surface. This condition helps to stabilize the

hydrogen surface concentration and subsequently its behavior becomes as in the potentiostatic mode (the last criterion is clearly explained in the permeation of materials that have considerable thickness and low diffusivity).

Figure 48 shows the hydrogen permeation profile superimposed on the cathodic polarization potential ($E(t)$) monitoring for sample $L = 0.40$ mm. It shows that the permeation profile (anodic cell) and potential variation profile (cathodic cell) reach stabilization at same time ($t_{\text{solubility}} = 750$ seconds). The last analysis shown for the permeation in Armco-Fe fulfills the galvanostatic condition. Furthermore the potential fluctuated randomly after reaching stabilization due to the fact that the material reaches a solubility limit, and consequently leads to in the amount of hydrogen fraction to evolve at the surface (the rate of hydrogen ingress being reduced)

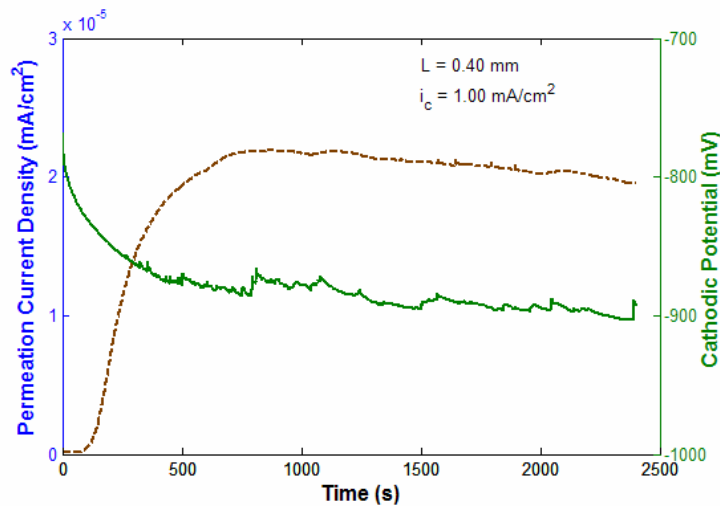


Figure 48: Hydrogen permeation current density and potential monitoring in charging side (Armco-Fe).

With the data obtained by monitoring the polarization potential in the cathodic cell it is possible to determine the concentration of hydrogen at the surface and subsurface as explained in the chapter 1, based on the Rajan [16] model.

Figure 49 shows the evolution of hydrogen concentration on the surface and in the subsurface. Concentration on the surface is obtained by Nernst equation by considering a basic hydrogen reduction at the surface (H_2). The Nernst equation (12) states:

$$E(t) = E_o + \frac{RT}{zF} \ln(C(H^+)) \quad (12)$$

where:

E_o : Open Circuit potential (V)

E : Polarization potential (V)

R : Real gas constant ($R=8.31451$ J/(mol K))

F : Faraday constant ($F=96485$ A.s/mol)

$$C(H^+) = \exp\left(\frac{zF(E(t) - E_o)}{RT}\right) \quad (13)$$

The hydrogen concentration in the subsurface is obtained for the galvanostatic charging condition with equation 7 or 8 at $x = 0$.

With this result one can observe that the hydrogen concentration on the surface ($C(H^+)$) though decreases, it can reach a steady state approximate value equal to 1.75×10^{-6} mol-H/cm³, while in the subsurface, the contrary of increasing concentration attaining a stable value approximately equal to 9.75×10^{-6} mol-H/cm³, is achieved

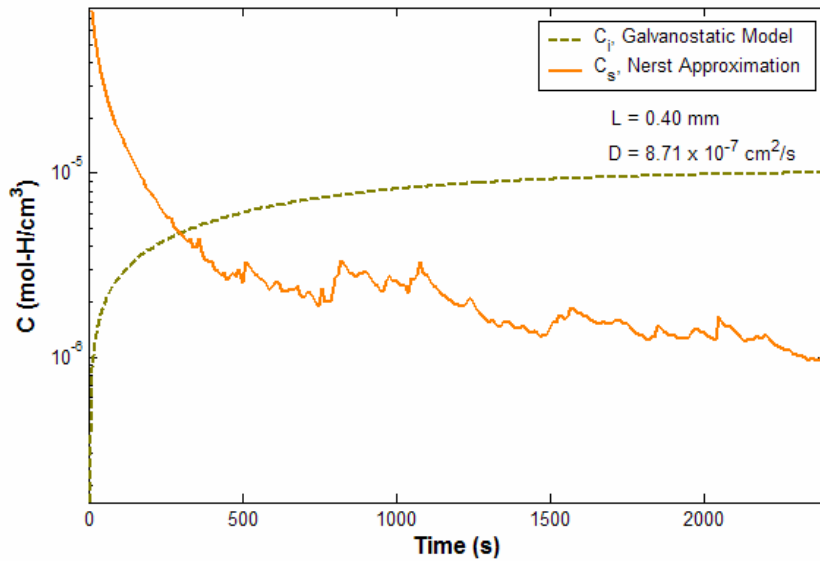


Figure 49: Hydrogen concentration in surface (C_s) and subsurface (C_i) evolution in function of time (Armco-Fe).

4.3.3.2. AF1410 Steel

Similar to the case of Armco Fe, Figure 50 shows the superimposed profiles of permeation and cathodic polarization potential, for AF1410 steel. It indicates that the time to achieve stabilization is 1000-1500 seconds (cathodic potential) which is faster than the time to reach a steady state in permeation ($t = 4000$ seconds). This difference shows us that the behavior is in a potentiostatic mode and it is not valid in the initial supposition as galvanostatic mode. The comparison made with both models and experimental results have good fitting to the galvanostatic model for samples with small thickness ($L = 0.09$ mm), in contrast to samples with $L \geq 0.16$ mm experiment data fitting the potentiostatic mode is better.

The variation of hydrogen concentration at the surface and in the subsurface is shown in Figure 51. The concentration of hydrogen at the surface is approximately 1.22×10^{-10} mol-H/cm³ while in the subsurface is 1.20×10^{-3} mol-H/cm³.

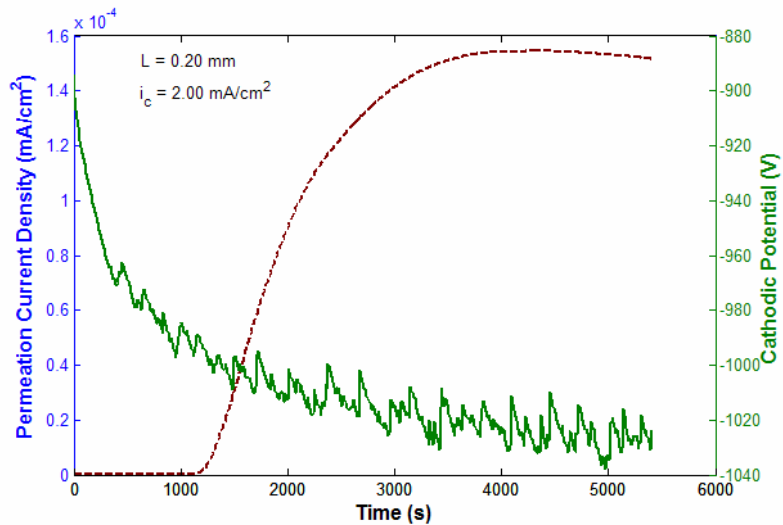


Figure 50: Hydrogen permeation current density and potential monitoring in charging side (AF1410 steel).

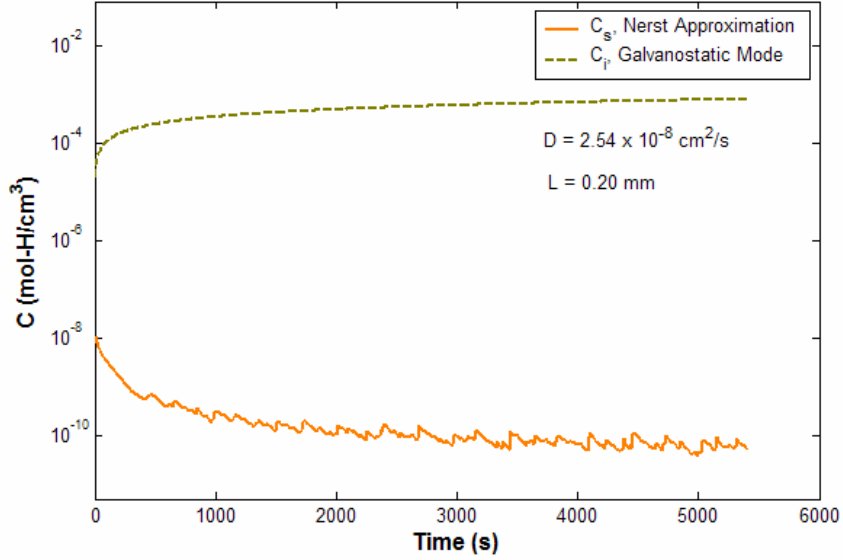


Figure 51: Hydrogen concentration at the surface (C_s) and subsurface (C_i) evolution as a function of time for AF1410 Steel.

4.3.4. Hydrogen Desorption

4.3.4.1. Armco-Fe

To determine the mathematical description for desorption we use the deduced equation found in chapter 1 for the concentration profile in a plate (sample). These equations show that near to the input surface the hydrogen concentration is high.

Analysis and study made by Zakroczymski [17], demonstrated that it is possible to use the concentration equation described by the potentiostatic mode, using the first Fick's law at $x = 0$ and $x = L$ to calculate the amount of hydrogen that leaves the material based on the following deduction:

Entry side $x = 0$:

$$\frac{J(t)}{J_\infty} = 2 \sum_{n=1}^{\infty} \exp\left(-\left(\frac{n\pi}{L}\right)^2 Dt\right) \quad (14)$$

Exit side $x = L$

$$\frac{J(t)}{J_{\infty}} = -2 \sum_{n=1}^{\infty} (-1)^n \exp\left(-\left(\frac{n\pi}{L}\right)^2 Dt\right) \quad (15)$$

To obtain the total diffusible hydrogen leaving the material, we integrate with respect to time ($\int_0^{\infty} J(t)dt$), both equations and obtain the following:

$$q_{x=0} = \frac{J_{\infty} L^2}{3D}$$

$$q_{x=L} = \frac{J_{\infty} L^2}{6D}$$

Mathematical demonstrations show that the amount of the hydrogen desorbed in the extraction surface is 1/3 of the total amount while in the charging surface is 2/3. Zakroczymski [17], experimentally demonstrates this result. Furthermore we obtained in Armco-Fe that the 97.7% of hydrogen is in the trapped while the rest is diffusible.

Experimental desorption process was made as explained earlier. Figure 52 shows the experimental profile and the model while the difference of both is known as or attributed to the reversible trapping at $x = L$. Table 17, shows the summary of amount of hydrogen leaving the sample.

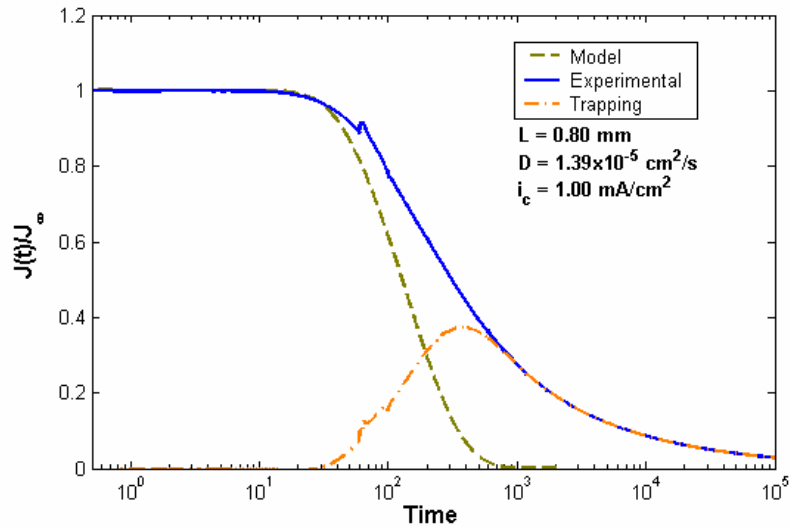


Figure 52: Hydrogen desorption (experimental, diffusible and trapping), in exit site (Armco-Fe).

Table 17: Relation of diffusible and trapped ($d_g = 16.0 \mu\text{m}$) hydrogen (Armco-Fe).

Thickness (L, mm)	H Diffusible		H trapped		Total H	
	%	(mol-H/cm ²)	%	(mol-H/cm ²)	%	(mol-H/cm ²)
0.40	2.27	1.39×10^{-8}	97.73	5.97×10^{-7}	100	6.11×10^{-7}
0.55	1.37	2.91×10^{-8}	98.63	2.09×10^{-6}	100	2.12×10^{-6}
0.80	1.38	3.19×10^{-8}	98.62	2.27×10^{-6}	100	2.30×10^{-6}

The desorption time for the samples with thickness 0.40 mm is 12600 seconds, while for the samples with 0.80 mm and 0.55 mm it is 100000 seconds. Desorption time is taken when the current density reaches same value or approximately the minimum current reached before recording the first hydrogen permeation.

In samples that have small thicknesses, hydrogen tends to evacuate the bulk very fast and consequently the time for desorption process is short, contrary to the case of samples that have relatively large thickness, where most of the hydrogen tends to stay in the material with long retention times. In most cases these behave like irreversibly trap. Shown especially in the sample with thickness 0.80 mm the percentage of hydrogen leaving the sample is close to the case for 0.55 mm (refer to Table 17). Experimentally, the obtained values show that less than 2.27 % of hydrogen is diffusible while the rest is in trapped form.

The grain size (d_g) is inversely proportional to grain boundary length. As the grain boundary is a potential trapping sites, samples with $L = 0.20$, $L = 0.30$ mm and $L = 0.40$

mm in Table 18, shows the total diffusible hydrogen in the three thicknesses is between 11.00-15.50 %, which is high, if we compare with other samples ($d_g = 16.0 \mu\text{m}$). The total hydrogen desorbed in 0.20mm is a little higher if we compare to the sample with $L=0.30$ mm, due to increase in the trapping sites as explained earlier. For sample with $L=0.40$ mm the total hydrogen leaving the material (desorbed) is more than two times compared to the first two samples. This is due to the thickness differences. Desorbed time for $L=0.40\text{mm}$ was 20000 seconds and 10000 seconds for samples with $L=0.20$ and 0.30 mm.

Table 18 Relation of diffusible and trapped hydrogen (Armco-Fe).

Thickness (L, mm)	d_g (μm)	H Diffusible		H trapped		Total H	
		%	(mol-H/cm ²)	%	(mol-H/cm ²)	%	(mol-H/cm ²)
0.20	0.58	13.38	4.44×10^{-8}	86.62	2.87×10^{-7}	100	3.31×10^{-7}
0.30	1.95	11.22	3.67×10^{-8}	88.78	2.90×10^{-7}	100	3.27×10^{-7}
0.40	2.35	15.04	1.08×10^{-7}	84.96	6.12×10^{-7}	100	7.21×10^{-7}

4.3.4.2. AF1410 Steel

Figure 53 and Table 19 show the relationship between the total hydrogen desorbed with thickness. Hydrogen desorption tends to become stabilized when the thickness increases. The time for hydrogen to leave the material is short, when they (hydrogen) are near or close to the sample surface. If hydrogen is close to the center of the sample, this time tend to be infinity, and as a consequence the hydrogen can be called irreversible (irreversible trapped). The irreversible sites increase when the thickness increases.

Table 19: Total hydrogen desorbed of AF1410 steel.

Thickness (mm)	Desorption Time (s)	Total Amount of Hydrogen Desorbs, (mol-H/cm ²)
0.09	10000	7.616×10^{-6}
0.20	30000	9.678×10^{-6}
0.24	60000	1.070×10^{-5}
0.30	60000	1.077×10^{-5}

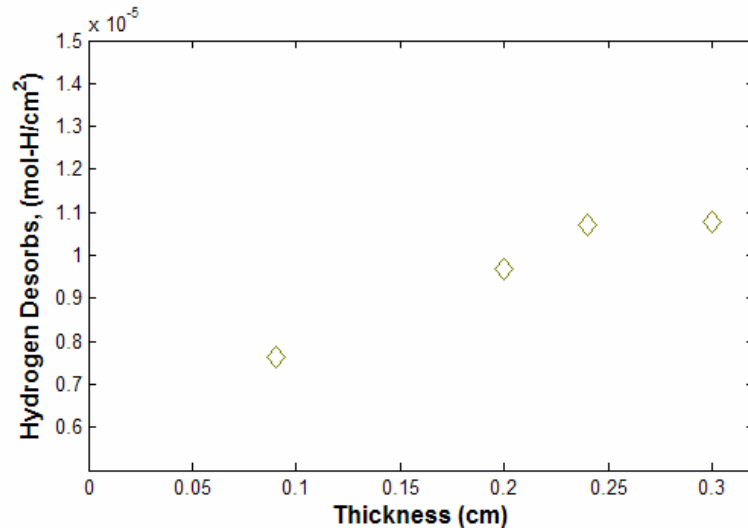


Figure 53: Hydrogen desorbed as a function of sample thickness (AF1410 Steel).

4.4. Optical Microscopy Analyses of Charging Surface

4.4.1. Armco-Fe

4.4.1.1. Charging Condition

Figure 54 shows the optical micrograph obtained with samples before charging and after charging conditions (time taken for charging time of 1500 seconds). Figure 54 (a) shows a sample without hydrogen charging, examined with AFM (Atomic Force Microscope) showing that this surface have a roughness value of $R_q = 7.10$ nm (surface as a mirror, with final polishing). In samples with a 0.25 mA/cm² charging no blister formation was observed, while for higher charging condition up to 1.00 mA/cm² blister formation was observed, as shown in Figures 54 (b), (c) and (d). In agreement with charging current increases, blister formation and surface damage are more severe. In most cases the blister formed linearly along certain direction (cold rolling direction). SEM image (see Figure 55) shows the effects of hydrogen induces cracking, (HIC), due to the high pressure caused by the accumulation of molecular hydrogen.

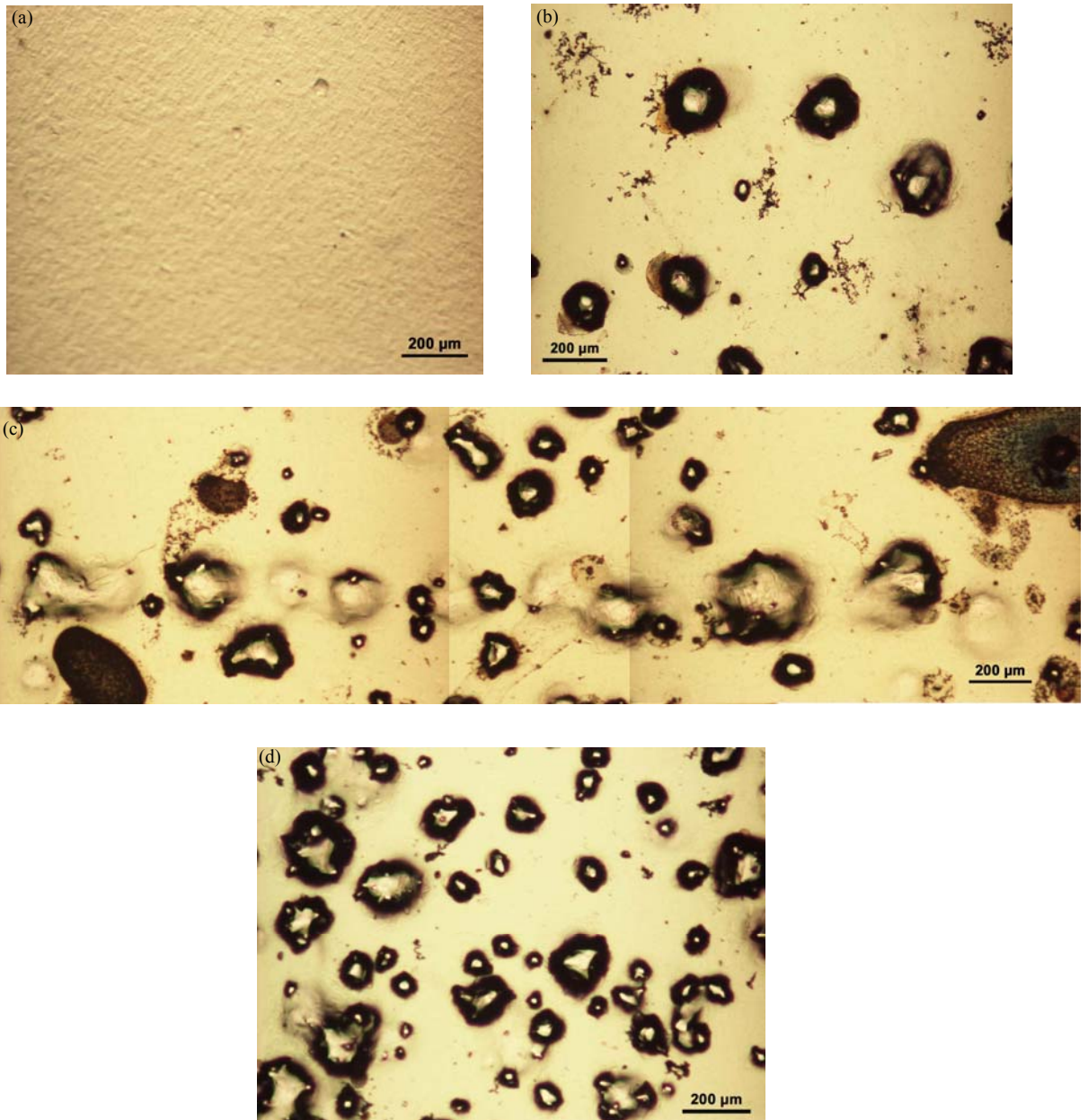


Figure 54: Optical microscopy (a) without charging, (b) 1.00 mA/cm² charging condition, (c) 3.00 mA/cm² charging condition and (d) 10.00 mA/cm² (Armco-Fe), all samples have a previous heat treatment two hour to 600°C with air cooling (L= 0.80 mm).

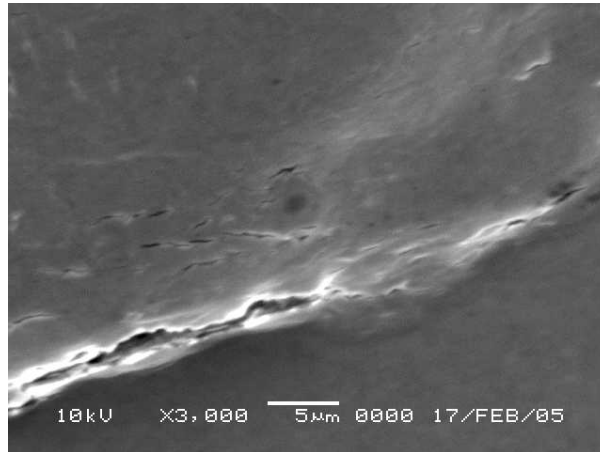


Figure 55: SEM image of hydrogen induced cracking (HIC) in Armco-Fe (L=0.20mm, with previous heat treated two hour to 600°C with air cooling condition).

4.4.1.2. Promoter Effect

Formation and blister growth depend on hydrogen entry into the material. In samples charged with a solution without poison, the blister is present in small quantity as shown in Figure 56 (a), whereas if we increase the poison concentration, the blister appears in considerable amounts as shown in the Figures 56 (b) and (c). For higher promoter concentration the blisters are not present as shown in Figure 56(d). Important parameter that is necessary to be considered is the charging time since for samples charged with poison containing electrolyte the necessary charging time is 3000 second while without poison, the charging time is 11000 seconds.

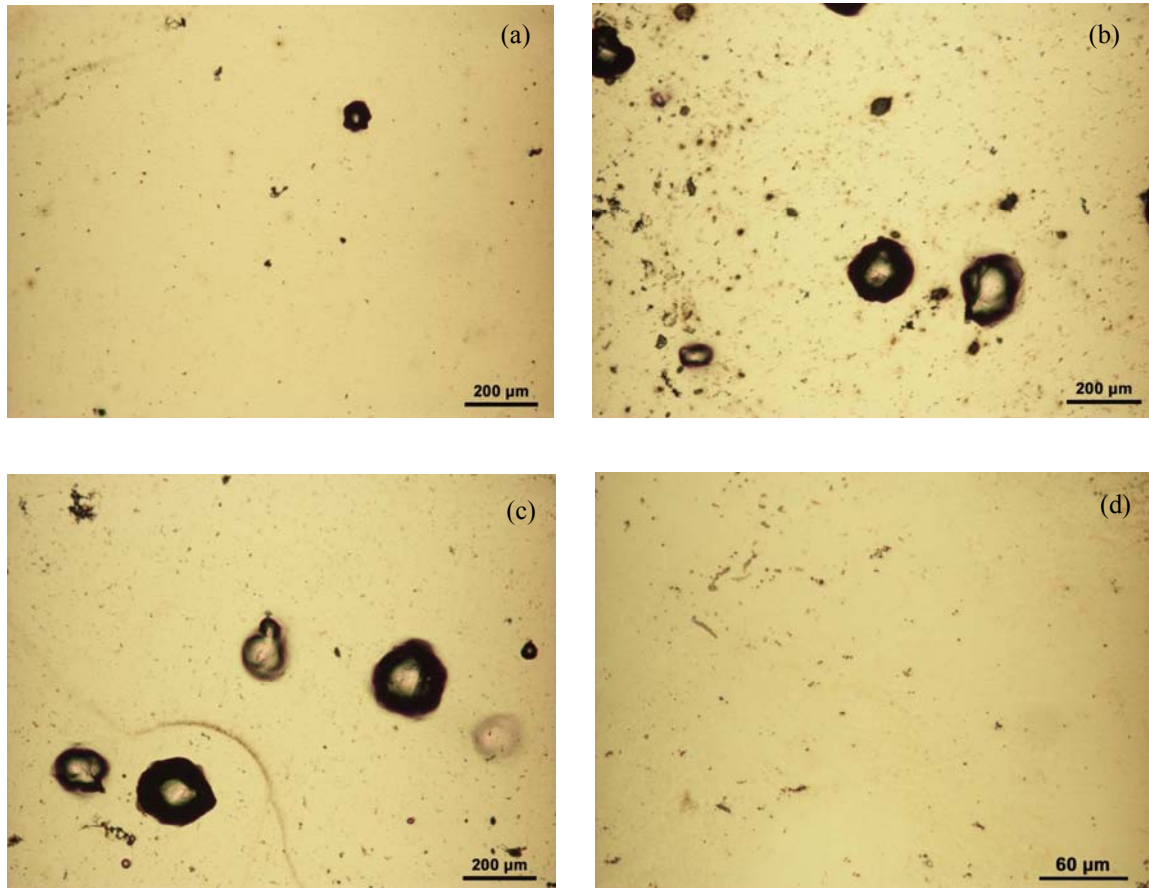


Figure 56: Optical surface micrograph; (a) 0.00 g/l $\text{Na}_2\text{HAsO}_4 \cdot 7\text{H}_2\text{O}$, (b) 0.25 g/l $\text{Na}_2\text{HAsO}_4 \cdot 7\text{H}_2\text{O}$, (c) 1.00 g/l $\text{Na}_2\text{HAsO}_4 \cdot 7\text{H}_2\text{O}$, (d) 10.00 g/l $\text{Na}_2\text{HAsO}_4 \cdot 7\text{H}_2\text{O}$ (Armco-Fe) ($L=0.78\pm 0.03\text{mm}$, with previous heat treatment two hour to 600°C with air cooling condition).

4.4.2. AF1410 Steel

Formation of blister is not as severe in AF1410 UHSS in comparison to Armco-Fe. In high charging conditions, i.e., for more than $3\text{mA}/\text{cm}^2$, we observe a small amount of formation of blister on both sides (entry and extraction), as shown in Figure 57 (a, b).

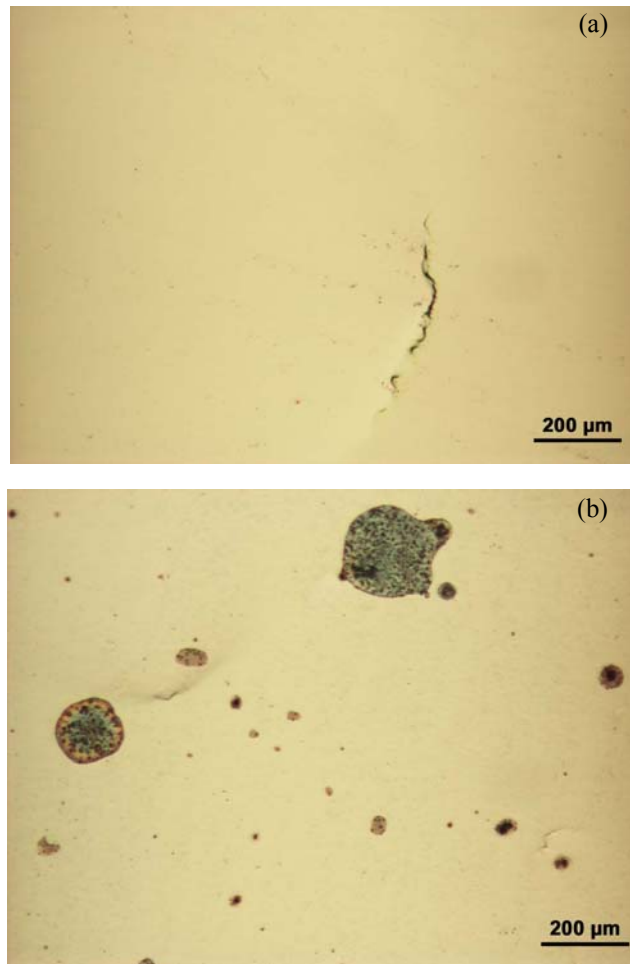


Figure 57: (a) Extraction and (b) entry surface (AF1410 Steel) (L = 0.35mm).

4.5. Fatigue Crack Propagation Analysis (AF1410 Steel)

From Figure 31 the crack growth rate da/dN with prior cathodic hydrogen charging was almost 4 times greater than in air. It indicated that the presence of hydrogen in the steel decreased the fatigue life of this steel as reported in the literature [21]. The effects of hydrogen into the material, is to decrease the strength in the atomic bonding and the weakening of the grain boundaries (depends on hydrogen concentration in the bulk) which represent a deleterious effect in the plastic deformation of the material during crack growth.

The testing frequency for specimen in air and with prior hydrogen was at 3Hz and 1Hz respectively. The effect of the frequency on the specimen when this was tested in air conditions does not have significant variation in the lifetime (as show in Figure 31), only if the frequency remains in the range of 0-10Hz. On the other hand, the specimen with prior hydrogen charging was evaluated at 1Hz frequency which represents acceleration in the crack growth rate compared with air conditions. At low testing frequencies, the hydrogen probably will have more time to move into the material at places where there are higher stress concentrations, especially at the crack tip (high tri-axial stresses).

The specimens charged with hydrogen and its behavior in fatigue is hard to predict since random behavior could be present. To get a reliable understanding of the hydrogen effects into the material, the fatigue crack growth rates were represented using error bars.

The presence of hydrogen into the material increase the fatigue crack growth as show in Figure 32, consequently reduce fatigue life. Moreover, behavior of samples at 1Hz and 3Hz in air condition non show significant difference. Prior hydrogen charged samples can be reduces approximately to a half of life of this ultra high strength steels compared to the life under air testing condition (@1 o 3 Hz). Fatigue test performed in all cases are in stable crack growth zone (zone II).

It is possible approximate the total amount of hydrogen content in compact tension sample, making a simple analysis of fracture surface and hydrogen desorbed of sample with previous electrochemical charged. Compact tension sample is charged electrochemically with hydrogen followed by a desorption process. The total amount of hydrogen leaved the sample is equal to 4.887×10^{-6} mol-H/cm². Furthermore in fracture surface (Figure 64 and 65) is clear see the part of hydrogen leaved the sample the depth approximately is equal to $50 \pm 5 \mu\text{m}$ with respect to charging surface. The total hydrogen desorbed in the sheet (L = 0.09 mm) of AF1410 steel is equal to 7.616×10^{-6} mol-H/cm², also the quantity of hydrogen desorbed in the input side is equal to 5.077×10^{-6} mol-H/cm² (2/3 part of total demonstrated earlier). Since both values obtained are similar, one then can conclude that the total amount of hydrogen content in $50 \pm 5 \mu\text{m}$ is approximately equal to 4.887×10^{-6} mol-H/cm². Moreover the fracture surface of fatigue specimens

showed that the hydrogen ingress depth is equal to 1.5 ± 0.2 mm, thereby indicating that the total content of hydrogen in the specimen is approximately to 1.466×10^{-4} mol-H/cm²

4.5.1. Fracture Surface Analysis

In the fractured surface, it is easy to see the part affected by the presence of hydrogen. There are clearly differences in the zones thus: brittle fracture zone (BFZ), ductile fracture zone (DFZ), pre-cracked zone (PCZ) and the area where hydrogen was charged (HCS) as shown in Figures 58 and 59.

As shown in the SEM fractured surface image (Figure 59) hydrogen charging for 234 hours (cathodic hydrogen charge time) can ingress approximately to a depth of 1.5 ± 0.2 mm. Areas that have a high concentration of hydrogen are characterized by intergranular and transgranular fracture as shown in Figure 60; whereas in areas without hydrogen, ductile fracture is observed (Figure 61). It is easy to see the area where the hydrogen tend to leave the material ($55 \mu\text{m}$ approximately). In this area the ductile combined with quasi cleavage fracture mode are present (Figure 62). Same fracture modes are present in the transition part (limit of depth where the hydrogen can ingress, Figure 63 and 64). This area is characterized by the low concentration of hydrogen.

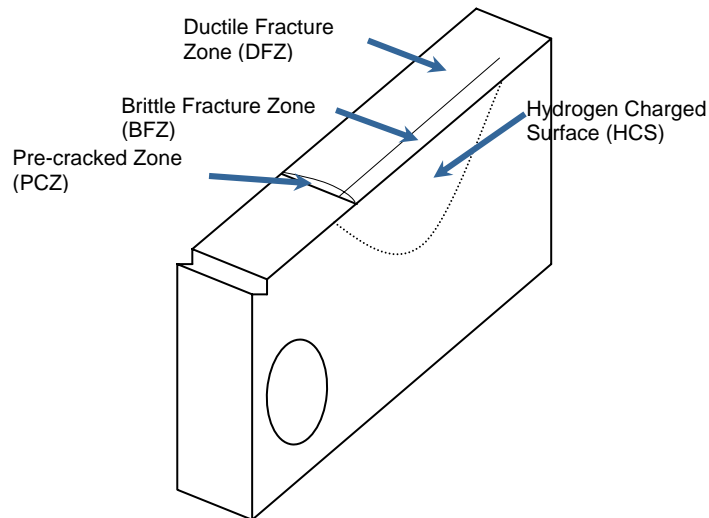


Figure 58: Differentiation of fracture zones and cathodic hydrogen charge.

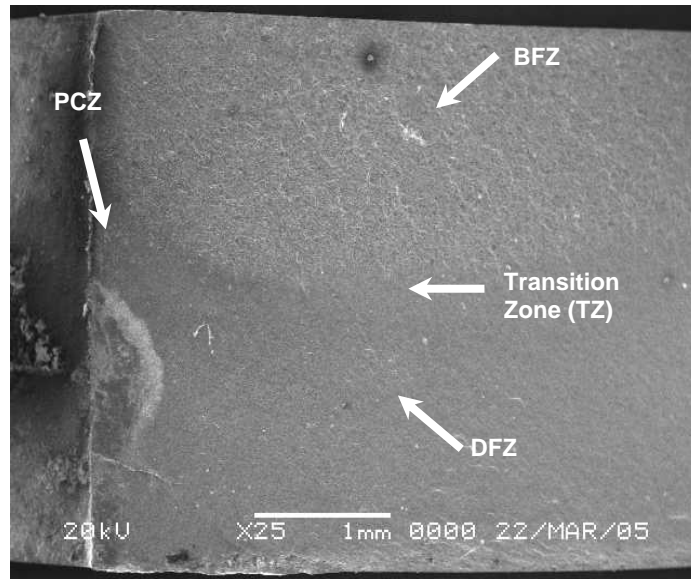


Figure 59: Scanning Electron Microscope (SEM) image of fracture surface, with prior cathodic hydrogen charge (AF1410 steel).

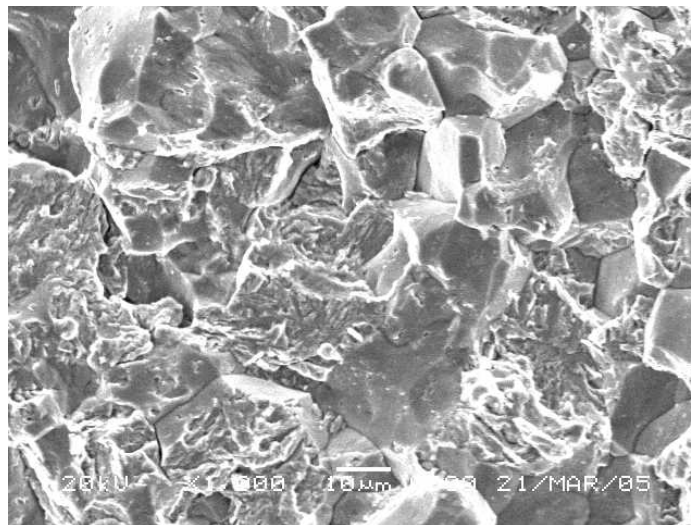


Figure 60: Brittle fracture zone with prior cathodic hydrogen charge (AF1410 steel).

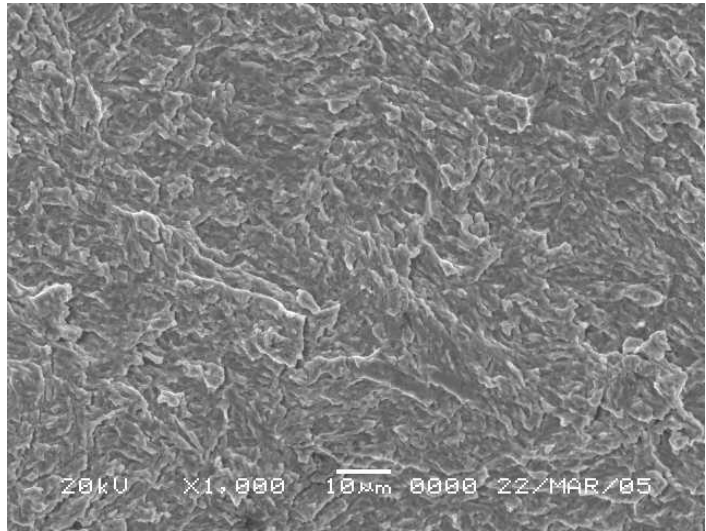


Figure 61: Ductile fracture zone (Without hydrogen), AF1410 steel.

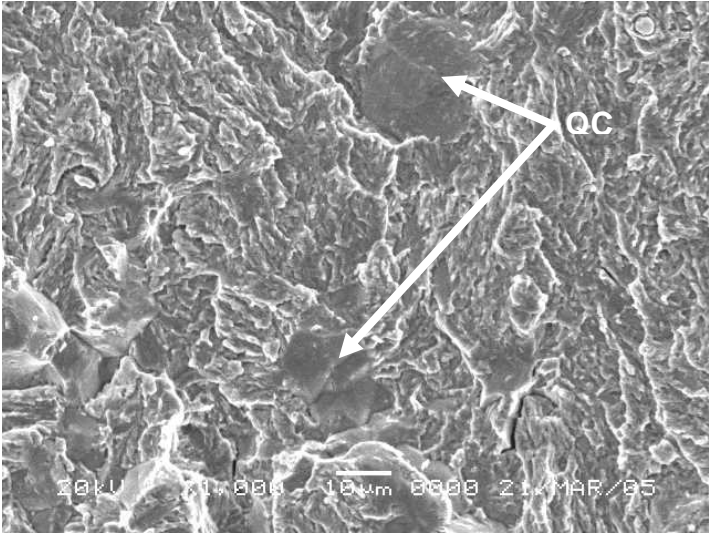


Figure 62: Ductile, brittle and quasi cleavage (QC) fracture (intermediate zone), AF1410 steel.

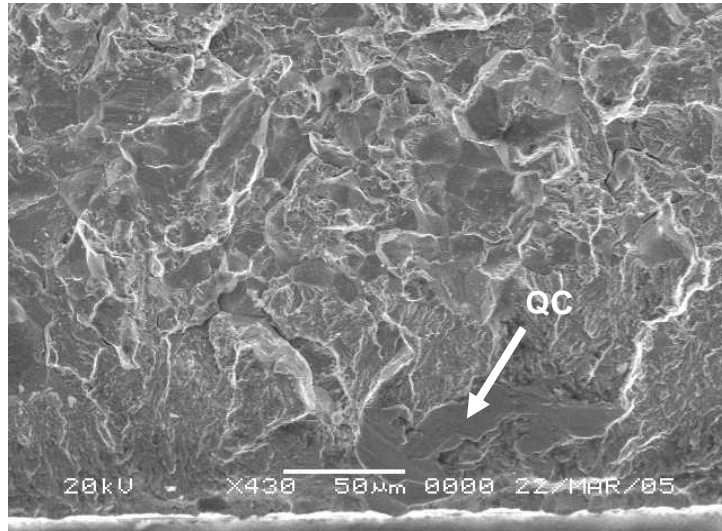


Figure 63: Ductile, brittle and quasi cleavage (QC) fracture zone (close to face to cathodic hydrogen charge), AF1410 steel.

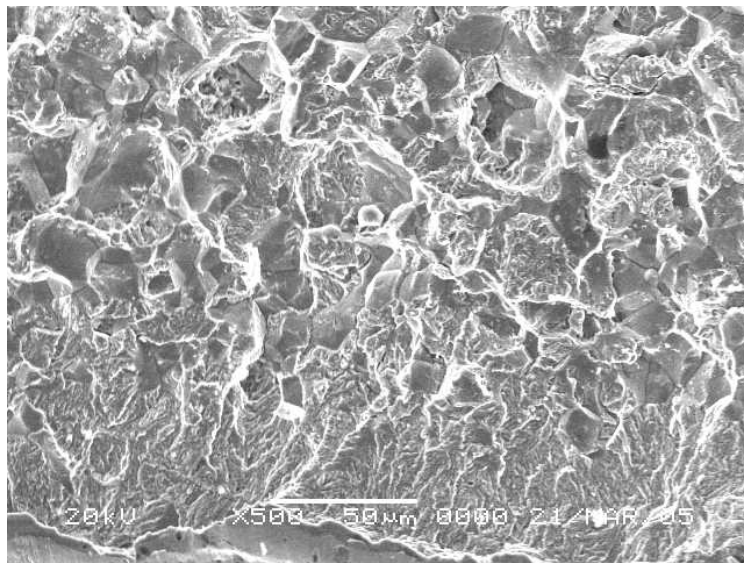


Figure 64: Ductile fracture zone combine with brittle, near to charging surface (AF1410 steel).

5. CONCLUSIONS AND RECOMMENDATIONS

5.1. Conclusions

- The optimal charging current density obtained for Armco-Fe is 1.00 mA/cm^2 in $0.1\text{MH}_2\text{SO}_4 + 1.00 \text{ g/l Na}_2\text{HAsO}_4 \cdot 7\text{H}_2\text{O}$, and for AF1410 steels 2.00 mA/cm^2 with same solution. This is based on the analyses of the permeation experiments.
- The promoter that is most effective for permeation in an acid solution (pH=1.2), is sodium arsenate.
- The acid solution ($0.1\text{MH}_2\text{SO}_4$) gave the best experimental result of permeation and consequently of diffusion parameters. For alkaline solution under same charging conditions as indicated in reference [17] gives a relatively low diffusivity value. Also the permeation profile is observed to fluctuated with time for both cases with a $1.00 \text{ g/l Na}_2\text{HAsO}_4 \cdot 7\text{H}_2\text{O}$ solution
- The promoter concentration in the solution is critical, as manifested by the effect in the fraction of hydrogen surface coverage. The optimum promoter concentrations are between 0.25 to 1.00 g/l approximately in acid solution.
- Hydrogen diffusivity decreases with increase in materials thickness, due to enhanced trapping binding energy. The maximum trap energy obtained is 9.72 KJ/mol , for a 0.80 mm thick ($d_g=16.0\mu\text{m}$) Armco-Fe, with prior heat treatment.
- In Armco-Fe, the effect of cold work leads to the reduction of diffusivity and permeability of hydrogen. This is due to the increase in the number of trapping sites and consequently the trap energy. The maximum value obtained corresponds for 0.20 mm ($d_g=0.58\mu\text{m}$) thickness to 20.81KJ/mol .
- The permeation profile decreases after attaining a maximum rate of permeation in the As-receive samples (cold work) of Armco-Fe, as consequence of dislocation acting as barriers or irreversible trapping sites.
- Grain boundaries act as irreversible trapping sites; as were clearly shown in the permeation profile for different grain sizes. In samples with small grain size the diffusivity coefficient is small in comparison to the large grain sized ones. Furthermore the trap binding energy is higher for small grain sized materials.

- The decrease of hydrogen permeation rate occurs in poor surface finished materials (roughness), due to the high retention time of H₂ at the surface being much higher than in better surface finished materials.
- Hydrogen Permeability in AF1410 steel is higher than in Armco-Fe, with the maximum value obtained for a 0.09 mm (thickness) equal to 3.47×10^4 A/cm²; this suggested that the solubility limit is higher, due to the multiphase nature of the material.
- The obtained value of diffusion coefficient that have a good fit in Armco-Fe is based on the breakthrough time, and for AF1410 steels the slope method.
- Hydrogen desorption in Armco-Fe in samples with grain size of 16μm is in the range of 2.27 to 1.38 % diffusible, while reversible trapping forms the rest. In samples with small grain size the percentage of diffusible hydrogen is in the range of 11.22 to 15.04 %. The increment is due to the increase of retained hydrogen in irreversible trapping sites (grain boundaries)
- The hydrogen escape in Armco-Fe with prior charge is three times less than approximately that in AF1410 steels. This is due to the high hydrogen solubility in AF1410 steels
- Hydrogen permeation rate decreases (in as-received cold worked samples) with simultaneous formation of blister at charging surface, and subsequently suffer hydrogen induce cracking.
- Blister formation seems to align preferentially to the direction of cold rolling, while formation depends only on hydrogen rate of entry in to the metal.
- If the concentration of hydrogen in AF1410 steel is high, fracture surface are present in transgranular and intergranular forms. In low concentration of hydrogen, material fracture is in the ductile and quasicleavage forms.
- The hydrogen that are between the surface and 55μm depth of the material tend to be evacuated in greater amount out of the material. In this part, fracture surface shows dominant ductile form and appreciable quasicleavage form. Similar fracture surface is observed in the transition part.

5.2. Future Work

5.2.1. Hydrogen Thermal Desorption

In order to determine the amount of hydrogen in the irreversible trapping sites as a function of grain boundaries, dislocations, austenitic phase, and interphase regions, etc., it is necessary to develop a hydrogen thermal desorption analysis as shown in figure 62 by Park et al. [29]

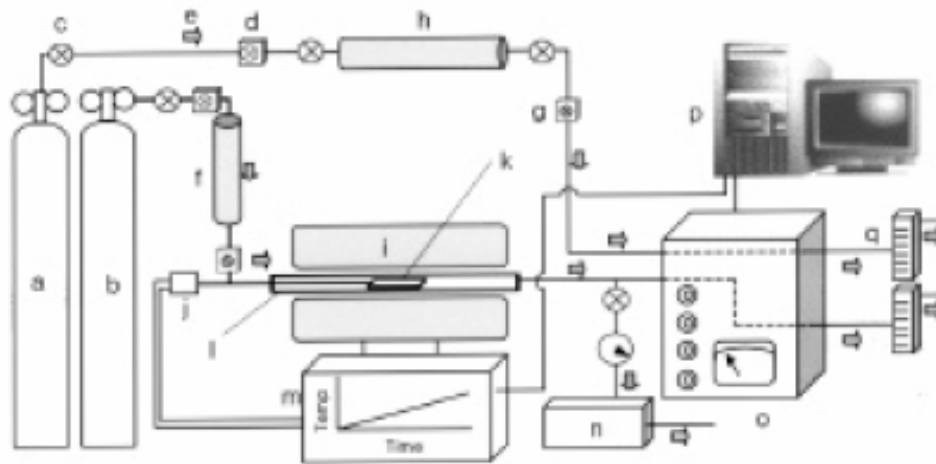


Figure 65: — Hydrogen thermal desorption analysis apparatus. a — reference gas cylinder (argon); b— carrier gas cylinder (argon); c — valve; d — pressure gauge; e — gas flow direction; f — oxygen trap; g — flow gauge; h — moisture trap; i — furnace; j — thermocouple; k — sample; l — fused silica tube; m — furnace controller; n — vacuum pump; o — gas chromatograph; p — computerized data acquisition system; q — flow meter [29]

The thermal desorption technique permits the measurement of hydrogen release in a material from various trap sites during a constant rate heating of the material under investigation. The system as shown in figure 62 utilizes a temperature controlled furnace and a fused silica tube wherein hydrogen charged sample is heated at a constant rate under a constant Argon carrier flow. For subsequent analysis, the release argon and hydrogen gas is fed into a gas chromatograph which permits quantitative analysis.

6. REFERENCES

- [1]: John P. Hirth: Effects of Hydrogen on the Properties of Iron and Steel. Metallurgical Transaction A; Vol. 11A 1980 pp 861-890
- [2]: V. S. Agarwala and J.J. De Luccia: Effect of Magnetic Field on Hydrogen Evolution Reaction and Diffusion in Iron and Steel
- [3] Daoming Li, Richard P. Gangloff, and J. R. Scully; Hydrogen Trap States in Ultrahigh-Strength Aermet 100 steel. Metallurgical and Materials Transformation A. Volume 35A, March 2004 pp 849-864.
- [4]: M Iino: More generalized analysis of hydrogen trapping: Acta Metallurgica Vol 30 pp 367; 1982
- [5]: George Chalaftris: Doctoral Thesis: Evaluation of Aluminum-Based Coating for Cadmium Replacement: Granfield University: December 2003
- [6]: C.J. Wen, C. Ho, B.A. Boukamp, I.D. Raistrick, W. Weppner, R.A. Huggins: Use of Electrochemical Method to Determinate Chemical – Diffusion Coefficient Alloy: and Application to LiAl: International Metals Reviews, 1981 Nro 5, pp 253-268
- [7]: T. Casanova and J. Crousier: Study of Passive Layer on Steel by Hydrogen Permeation: Universite de Provence, 13331 Marseille cedex 3, France. (<http://www.corrosionsource.com/events/intercorr/techsess/papers/session4/abstracts/casanova.html>)
- [8]: Anthony W. Thompson: Stress Corrosion Cracking and Hydrogen Embrittlement; Metallurgical Treatises; Metallurgical Society; pp 589-601; P. A. 1981
- [9]; G. P. Tiwari, A. Bose: A study of Internal Hydrogen Embrittlement of Steel: Material Science and Engineering: A 286 (2000), P269
- [10]: R. A. Oriani: The Diffusion and Trapping of hydrogen in Steel: Acta Metallurgica, Vol. 18; January 1970 pp 147-157
- [11]: H. K. Birnbaum: Hydrogen Related Failure Mechanisms in Metals: Department of Metallurgy and Mining Engineering, University of Illinois at Urbana-Champaign: Urbana, Illinois 61801 U.S.A.

- [12]: L. Fournier, D. Delafosse, T. Magnin: Cathodic Hydrogen Embrittlement in Alloy 718: *Material Science and Engineering A* 269 (1999); pp 111-119
- [13]: ASTM G 148-97 (Reapproved 2003): Standard Practice for Evaluation of Hydrogen Uptake, Permeation, and transport in metals by an Electrochemical Technique
- [14]: Jan Barcik, Karol Stepien: Role of Al₂O₃ Surface Layer in Saturating Intermetallic FeAl compound with Hydrogen.
- [15]: John K. Tien, Anthony W. Thompson I. M. Bernstein and Rebecca J. Richard: Hydrogen Transport by Dislocation: *Metallurgical Transaction A* Vol. 7A 1976. pp 821-829
- [16]: Rajan N. Iyer, and Howard W. Pickering. A Mechanical Analysis of hydrogen entry into metals during cathodic hydrogen charging; *Scripta Metallurgica*, Vol 22, pp. 911-916 1988
- [17]: Tadeusz Zakroczymski: Electrochemical Determination of Hydrogen in Metals; *Electrochemical chemistry* 475 (1999) pp. 82-88
- [18]: J. F. Newman and L. L. Shreir; Role of Hydrides in Hydrogen Entry into Steel from Solution Containing Promoters; *Corrosion Science*, vol. 9 pp 631 to 641; 1969
- [19]: S.Y. Qian, B. E. Conway and G. Jerkiewicz; Kinetic Rationalization of Catalyst Poison Effect on Cathodic H Sorption into Metals: Relation Of Enhanced and Inhibition to Coverage; *J Chem. Soc, faraday Trans.*, 1998; pp 2945-1954
- [20]: Saxena, A. and Hudak, S., *International Journal of Fracture*, Vol. 14, No. 5, 1978, 453-468
- [21]: S. D. Antolovich: Fatigue Crack Propagation and Corrosion Fatigue of AF1410 Steel: Department of Material Science and Metallurgical Engineering: University of Cincinnati, Technical Report Ohio January 1980
- [22]: P.A. Sundaram, D. K. Marble: Hydrogen Diffusivity in Armet 100 at Room Temperature under Galvanostatic Charging Condition; *Journal of Alloys and Compound* 326 (2003) pp 90-97
- [23]: H. J. Cialone and J. h. Holbrook; Effect of Hydrogen on Fatigue Crack Growth in Pipeline Steel: *Metallurgical and transaction A*; Vol. 16A January 1985 pp115-121

- [24]: V. S. Agarwala D. A. Berman, and G. Kohlhaas; Causes and Prevention of Structural Materials Failure in Naval Environments; Structural Failures; Corrosion 84, (New Orleans, April) paper #115June 1985
- [25]: H. S. Carslaw and J. C. Jaeger; Conduction of Heat in Solids; Oxford at the Clarendon Press second edition 1958
- [26]: J. Crank; The Mathematic of Diffusion; Oxford and the Clarendon Press 1967
- [27]: K. Kiuchi and R. B. McLellan; The Solubility and Diffusivity of Hydrogen in well-annealed Deformed Iron; Acta Metall; Vol. 31 pp 961-984, 1983
- [28]: S. L. Amey, G. M. Michal, and J. H. Payer; Modeling Hydrogen Entry and Exit in Metals Exposed to Multiple Charging Process; Metallurgical and Material Transaction A; Vol. 25A, April 1994-723
- [29]: Y. D. Park, I. S. Maroef, A. Landau, and D. L. Olson; Retain Austenite as a hydrogen Trap in Steel Welds; Welding Research February 2002, pp 27-35
- [30]: R. A. Oriani; The Physical and Metallurgical Aspects of Hydrogen in Metals; Four International Conference on Cold Fusion, 1993. Lahaina, Maui: Electric Power Research Institute.

APPENDIX A.

A.1. Mathematical Consideration of Diffusion Phenomenon

If we have an anisotropic system (material) the **first Fick's law** can be shown thus:

$$J_i = -D_{ij} \left(\frac{\partial C}{\partial x_j} \right) \quad i,j = 1,2,3. \quad (16)$$

$$\begin{aligned} J_1 &= -D_{11} \left(\frac{\partial C}{\partial x_1} \right) - D_{12} \left(\frac{\partial C}{\partial x_2} \right) - D_{13} \left(\frac{\partial C}{\partial x_3} \right) \\ J_2 &= -D_{21} \left(\frac{\partial C}{\partial x_1} \right) - D_{22} \left(\frac{\partial C}{\partial x_2} \right) - D_{23} \left(\frac{\partial C}{\partial x_3} \right) \\ J_3 &= -D_{31} \left(\frac{\partial C}{\partial x_1} \right) - D_{32} \left(\frac{\partial C}{\partial x_2} \right) - D_{33} \left(\frac{\partial C}{\partial x_3} \right) \end{aligned} \quad (17)$$

From equation (17) we can obtain a diffusion tensor that is:

$$D_{ij} = \begin{bmatrix} D_{11} & D_{12} & D_{13} \\ D_{21} & D_{22} & D_{23} \\ D_{31} & D_{32} & D_{33} \end{bmatrix} \quad (18)$$

For isotropic case, the tensor reduces thus:

$$D_{ij} = \begin{bmatrix} D_{11} & 0 & 0 \\ 0 & D_{22} & 0 \\ 0 & 0 & D_{33} \end{bmatrix} \quad (19)$$

With $D_{11} = D_{22} = D_{33} = D$

Equation (18) reduces to:

$$J_i = -D \left(\frac{\partial C}{\partial x_1} \right) - D \left(\frac{\partial C}{\partial x_2} \right) - D \left(\frac{\partial C}{\partial x_3} \right) \quad (20)$$

which is same to equation (2)

If we consider the diffusion as unidirectional, it can be analyzed for each component. The second Fick's law can be shown in the following manner, for isotropic system (material):

$$-\nabla \bullet J_i = \frac{\partial C}{\partial t} \quad (21)$$

With $\nabla = \frac{\partial}{\partial x_1} + \frac{\partial}{\partial x_2} + \frac{\partial}{\partial x_3}$

$$D \left(\frac{\partial^2 C}{\partial x_1^2} + \frac{\partial^2 C}{\partial x_2^2} + \frac{\partial^2 C}{\partial x_3^2} \right) = \frac{\partial C}{\partial t} \quad (22)$$

A.1.1. Deduction of Mathematical Approximation to Determine the Diffusion Coefficient Parameter

If we want to know total amount of hydrogen passing through (permeated) the sample or membrane it, is necessary to integrate with respect to time equation (5) obtain the following relation [26]:

$$Q_t = \frac{DC_i t}{l} - \frac{C_i l}{6} - \frac{2C_i l}{\pi^2} \sum_{n=1}^{\infty} \frac{(-1)^n}{n^2} \exp\left(-D \left(\frac{n\pi}{l}\right)^2 t\right) \quad (23)$$

at infinity time, $t \rightarrow \infty$, then equation (23) simplifies to:

$$Q_t = \frac{DC_i}{l} \left(t - \frac{l^2}{6D} \right) \quad (24)$$

At a simple observation this equation is linear and with an intersect of $l^2/(6D)$ called the time lag. This expression offers a good approximation for calculating the coefficient of diffusion, D. Thus we express the intersect as

$$t_{lag} = \frac{l^2}{6D} \quad (25)$$

If we put equation 24 as a function of Dt/l^2 in Figure 66, observe that the steady state is reached when $Dt/l^2 = 0.45$, and furthermore, the first hydrogen permeates the

sample when $Dt/l^2 = 0.0654$ which is called the breakthrough time. It is another way

$$\text{for calculating the diffusion coefficient i.e. } t_b = \frac{l^2}{15.3D} \quad (26)$$

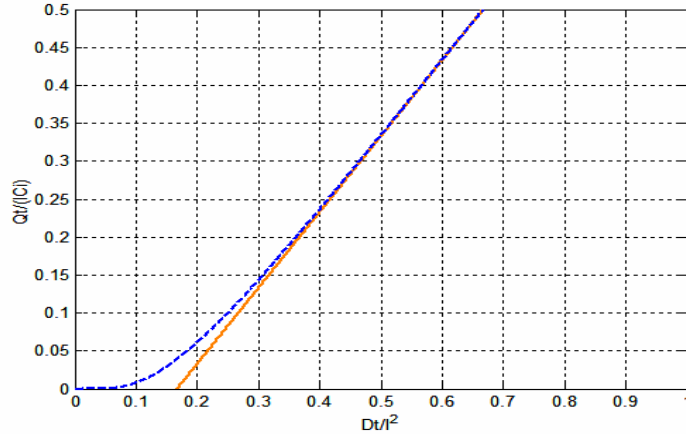


Figure 66: Approach to steady-state flow through a plane sheet.

APPENDIX B.

B.1. Slope Method to Determine the Diffusion Coefficient

Figure 63 and 64 show the slopes obtained, by taking the linear part of the transient of hydrogen permeation process in Armco-Fe (As-received cold rolled condition), and for the AF1410 steel. In both cases the $0.1\text{M}\text{H}_2\text{SO}_4 + 1.00\text{ g/l}$ sodium arsenate ($\text{Na}_2\text{HAsO}_4 \cdot 7\text{H}_2\text{O}$) was used to charge hydrogen. The following equation was used to determine the diffusion coefficient:

$$K = \frac{L^2 \log(e)}{4D}$$

where:

K: is the slope obtained

D: is the diffusion coefficient (cm^2/s)

L: is the thickness of sample (cm)

$$e = 2.71828182846$$

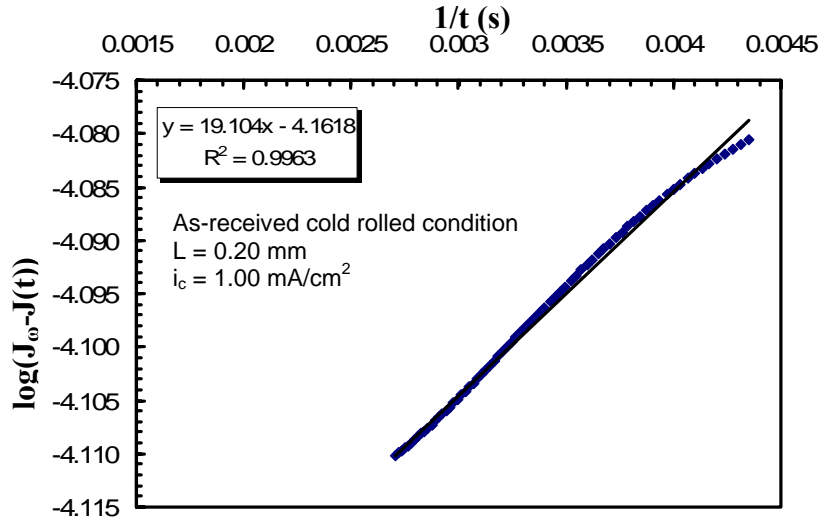


Figure 67: Slope determined from the data of hydrogen permeation transient for Armco-Fe.

Armco-Fe

$$D = \frac{L^2 \log(e)}{4K}$$

$$D = 2.27 \times 10^{-6} \text{ cm}^2 / \text{s}$$

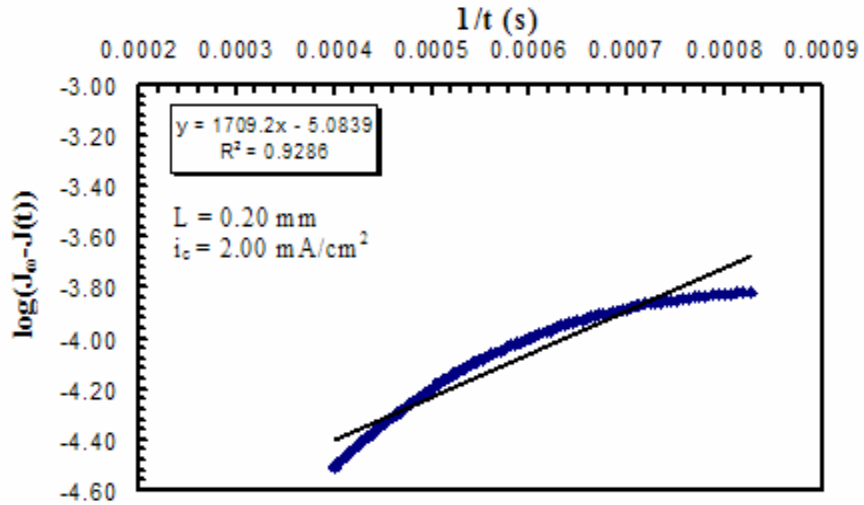


Figure 68: Slope determined from the data of hydrogen permeation transient for AF1410 steel.

AF1410 steel

$$D = 2.54 \times 10^{-8} \text{ cm}^2 / \text{s}$$